ALMA MATER STUDIORUM
UNIVERSITÀ DI BOLOGNA

DOTTORATO DI RICERCA IN

AUTOMOTIVE ENGINEERING FOR INTELLIGENT MOBILITY

Ciclo 37

Settore Concorsuale: 09/E2 - INGEGNERIA DELL'ENERGIA ELETTRICA

Settore Scientifico Disciplinare: ING-IND/32 - CONVERTITORI, MACCHINE E AZIONAMENTI ELETTRICI

ADVANCED DIAGNOSTIC AND CONTROL STRATEGIES FOR THREE-PHASE AND MULTHIPHASE ELECTRIC DRIVES

Presentata da: Antonio Femia

Coordinatore Dottorato

Davide Moro

Supervisore

Luca Zarri

Co-supervisore

Mattia Ricco

Esame finale anno 2025

"*What we know is a drop, what we don't know is an ocean.*"

Isaac Newton

Contents

List of Figures

List of Tables

List of Abbreviations

AI	**A**rtificial **I**ntelligence
MD	**M**anufacturing **D**efect
HRC	**H**igh-**R**esistance **C**onnection
SC	**S**hort **C**ircuit
PMSM	**P**ermanent **M**agnte **S**ynchronous **M**otors
VSI	**V**oltage **S**ource **I**nverter
RMS	**R**oot **M**ean **S**quare
ML	**M**achine **L**earning
PM	**P**ermanent **M**agnet
EV	**E**lectric **V**ehicle
BEV	**B**attery **E**lectric **V**ehicle
PHEV	**P**lug-in **H**ybrid **E**lectric **V**ehicle
CAGR	**C**ompound **A**nnual **G**rowth **R**ate
REE	**R**are **E**arth **E**lements
AC	**A**lternating **C**urrent
DC	**D**irect **C**urrent
RPM	**R**evolutions **P**er **M**inute
VSD	**V**ector **S**pace **D**ecomposition
ET	**E**xtra **T**urn
MMF	**M**agnetomotive **F**orce
VSI	**V**oltage **S**ource **I**nverter
SVM	**S**pace-**V**ector **M**odulation
PWM	**P**ulse-**W**idth **M**odulation

BEMF	**B**ack-**E**lectromotive **F**orce
FEM	**F**inite-**E**lement **M**odel
ITSC	**I**ntern-**T**urn **S**hort **C**ircuit
FOC	**F**ield **O**riented **C**ontrol

Physical Constants

Vacuum permeability	$\mu_0 = 4\pi \times 10^{-7}$ Hm^{-1}
Vacuum permittivity	$\varepsilon_0 = 8.8541878128(13) \times 10^{-12}$ Fm^{-1}

List of Symbols and Math Operators

μ	magnetic permeability	Hm^{-1}
μ_r	magnetic relative permeability	dimensionless
μ_0	magnetic vacuum permeability	Hm^{-1}
ε_p	electric permittivity	Fm^{-1}
$\bar{E}$	electric field vector	Vm^{-1}
$\bar{D}$	dielectric displacement vector	Cm^{-2}
$\bar{H}$	magnetic field vector	Cm^{-1}
$\bar{B}$	magnetic flux density vector	T
φ	magnetic flux	Wb
$\mathscr{F}$	magnetomotive force	Aturns
N_t	number of turns	dimensionless
$\bar{J}$	current density vector	Am^{-2}
i	current	A
ρ_c	charge density	Cm^{-3}
L	magnetic self-inductance	H
M	magnetic mutual-inductance	H
R	electric resistance	Ω
v	electric voltage	V
S	surface	m^2
l	length	m
$\hat{n}$	versor orthogonal to surface	dimensionless
$\bar{\kappa}$	magnetic dipole	Cm^2
$\bar{M}$	magnetic polarization vector	Am^{-1}

χ_m	material magnetic susceptibility	dimensionless
$\Re$	magnetic reluctance	H^{-1}
$\cdot$	scalar product operator	dimensionless
$\times$	cross product operator	dimensionless
$\Re_e$	real part operator	dimensionless
$\Im_m$	imaginary part operator	dimensionless
∇	divergence operator	dimensionless
$*$	conjugate operator	dimensionless
$'$	transposed operator	dimensionless

Dedico questo mio lavoro di tesi a te,

che non ci sei stata quando dovevi non esserci,

e che, quando dovevi esserci, non sei mai mancata.

A te che mi hai insegnato la forza della parola e la leggerezza del silenzio.

A te che mi hai educato alla felicità e ad affrontare la tristezza.

Dedico questo mio lavoro di tesi a tutti voi,

che adesso non ci siete ma continuerete ad esserci.

Al vuoto a cui avete dato forma e alla forma

a cui avete dato un senso di vuoto per la vostra scomparsa.

Alle braccia tese e alle mani intrecciate.

Alle poesie scritte al buio e ai versi pieni di luce.

Dedico questo mio lavoro di tesi

ai balli proibiti e alle sinfonie sussurrate.

Al tepore con cui mi avete cullato

e alla gioia con cui mi avete lasciato spiccare il volo.

Alle buche che avete tappato

e ai fiori che avete lasciato crescere nel mio animo.

Dedico questo mio lavoro di tesi

alle tante vite che mi avete donato senza mai chiedere nulla in cambio.
Grazie.

Mamma, Papà, Simona, Zia, Nonna, Elisa, Franco.

Introduction

The main objective of this thesis is to investigate the characteristics and performance of electrical machines that are specifically designed for industrial applications that need high power density and reliability, such as in the automotive sector.

The PhD thesis covers three independent topics.

A substantial part concentrates on developing methodologies for modeling malfunctioning electrical machines and employing Artificial Intelligence (AI) techniques to accurately identify and distinguish between different types of failures.

The studied failures comprised Manufacturing Defects (MDs), High-Resistance Connections (HRCs), and inter-turn Short Circuits (SCs). The methods presented in this research possess extensive applicability for surface-mounted Permanent Magnet Synchronous Motors (PMSM) but can be extended to a variety of motor typologies.

A further part of the doctoral program focuses on the control of two-level multiphase Voltage Source Inverters (VSIs).

Establishing appropriate and adaptable control strategies for VSIs is crucial for successfully exploiting the strengths of N-phase electric drives. In the context of this activity, a control technique was developed with the objective of minimizing the Root Mean Square (RMS) value of the output current ripple produced from multiphase inverters with odd number of phases.

Furthermore, the proposed approach optimizes the number of commutations of the power electronic switches. As a consequence, the current provided to the motor exhibits enhanced quality, leading to reduced deterioration of power electronic switching components and a reduction in motor overheating.

A significant contribution to the outcomes in condition monitoring resulted from the collaboration with the Polytechnic University of Valencia, where the research took place for six months. During this period, the research focused on the distinguishing properties of eccentric PMSM machines, which have a rotor axis of symmetry that differs from that of the stator. The study resulted in the development of a diagnostic strategy based on radial stray flux measurement. The method enables the differentiation of various kinds of eccentricity affecting the machine, including static, dynamic, and mixed eccentricity.

All the investigations have been assessed through simulations and experimental tests employing prototypes of three-phase and multiphase motors and converters.

The content of each chapter is detailed below.

Chapter 1 presents an in-depth review of current advances in the field of electrical drives suitable for automotive applications.

Chapter 2 provides a comprehensive introduction to multiphase electric drives with a particular focus on the Dual-Three-Phase (DTP) architecture.

Chapter 3 discusses in detail the principal failures that can impact the stator windings of a DTP drive. An analytical model is created for each of the faults mentioned, underscoring the potential of integrating the models into the control system and using fault-tolerant and fault-identification strategies.

Chapter 4 covers the application of Machine Learning (ML) for fault diagnostics. Two fault diagnosis methodologies that effectively diagnose the failures analytically outlined in Chapter 2 are presented.

Chapter 5 provides an in-depth description of a control technique for odd-phase inverters that aims to minimize the RMS of the ripple of the phase current as well as to reduce the number of commutations of the power electronics switches.

Chapter 6 provides a diagnostic method for identifying eccentricity in PMSM by measuring the magnetic flux surrounding the stator yoke, which is referred to as stray flux.

In conclusion, the achievements of the three-year doctoral research have been summarized, highlighting prospective future developments for the undertaken activities..

Chapter 1

The Automotive Sector and the Importance of Permanent Magnets

This chapter offers a comprehensive analysis of the electrification process within the automobile sector, focusing on its worldwide proliferation and its impact on Europe and Italy. The magnetic characteristics of Permanent Magnets (PMs) are delineated, emphasizing their significance in vehicle electrification.

1.1 Clean Energy and Electrification

1.1.1 World Trend

Despite facing challenges, there are strong indicators of a significant increase in the move towards renewable energy. Figs. 1.1 and 1.2 demonstrate the positive trends in the adoption of renewable energy sources, which contribute to reducing emissions and improving energy efficiency. The rise in investment is mostly focused on industrialized countries. In order to achieve the sustainable development goals, it is crucial to promote the widespread adoption of renewable energy projects. This should be done through strong domestic policies and international financial support. These goals include ensuring access to energy, addressing global climate issues, and enhancing energy security.

In this scenario, there has been a gradual transition within the automotive industry towards the manufacturing of Electric Vehicles (EVs). Despite they comprise a mere 2.1% of the

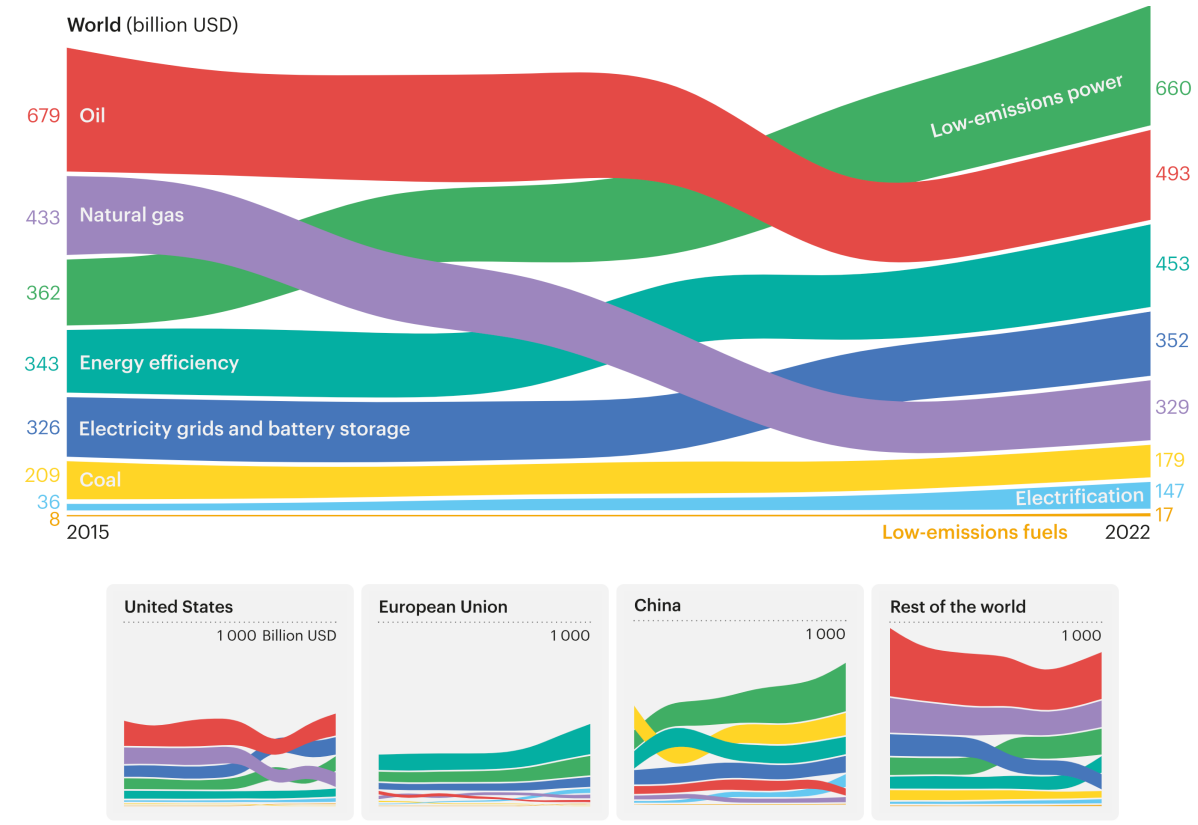

FIGURE 1.1: Investment flows [1].

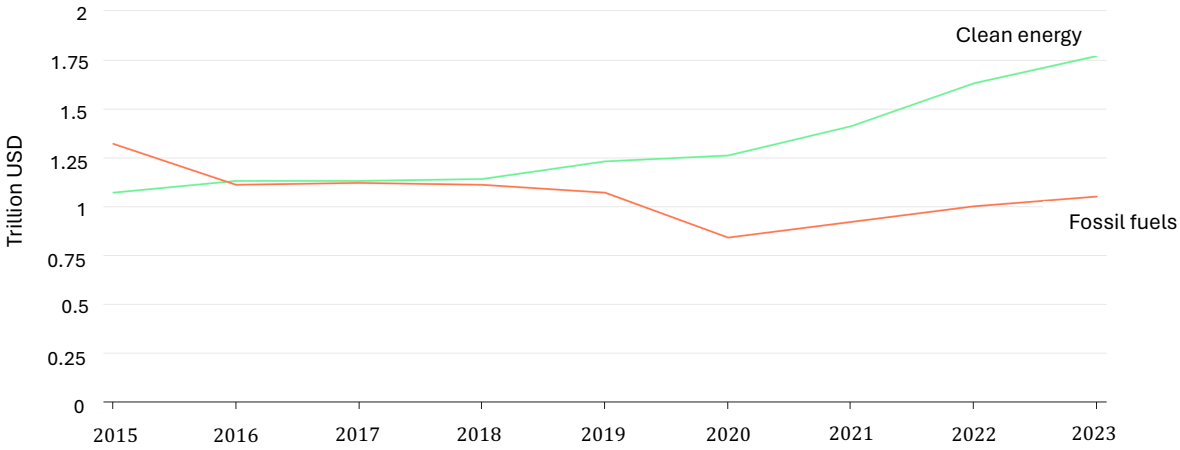

FIGURE 1.2: Investment in clean energy and fossil fuels [1].

worldwide vehicle inventory, available data indicates a substantial acceleration in the electrification process [2]. Different studies forecast that in ten years, 20% of all newly sold cars will be electric cars and in twenty years, around 25% [3]. This transition process exerts significant control over contemporary supply chains pertaining to automobile parts, as well as their design and manufacture procedures. Automobile manufacturers are allocating substantial financial resources towards research and development ($R\&D$) endeavors, along with the establishment of new manufacturing facilities, in order to effectively anticipate and adapt to future trends.

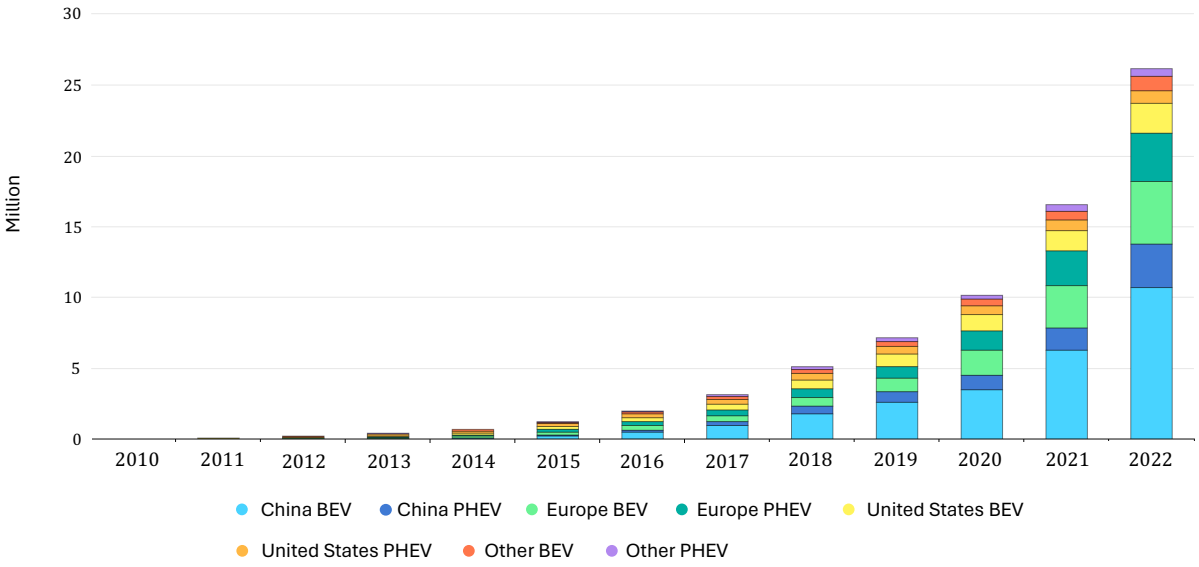

FIGURE 1.3: Global electric car stock [1].

Recent investment trends have begun to transition the global energy system toward one that is more electrified and renewables-rich [1]. Increasing sales pushed the total number of electric cars on the world's roads to 26 million in 2022, up 60% relative to 2021 with Battery Electric Vehicles (BEV) accounting for over 70% of total annual growth as depicted in Fig 1.3. The annual growth rate for electric car sales in 2022 was similar to the average rate over 2015-2018, and the annual growth rate for the global stock of electric cars in 2022 was similar to that of 2021 and over the 2015-2018 period, showing a robust recovery of EV market expansion to pre-pandemic pace.

As illustrated in Fig. 1.4, China has generated the highest revenue from EVs, followed by the United States with a four-fold lower profit. The revenues of the United Kingdom and France were approximately 50% of those of Germany.

1.1.2 European Trend

The European Union market is experiencing a gradual integration of EVs, encompassing both BEVs and Plug-in Hybrid Electric Vehicles (PHEVs). The number of new electric car registrations has consistently risen from 600 in 2010 to approximately 1.74 million in 2021, representing 18% of all new registrations . In 2022, the percentage of newly registered passenger automobiles that were electric increased to over 22%. In 2022, BEVs constituted 12.2% of all new automobile registrations, and PHEVs accounted for 9.4% (see Fig. 1.5)[5].

Compared to 2021, the proportion of newly registered EVs increased in nearly all nations (EU-27, Iceland, Norway) in 2022 (see Fig. 1.6). Norway accounted for the largest proportions (89%), followed by Sweden (58%), and Iceland (56%). Germany, France, and Norway constituted

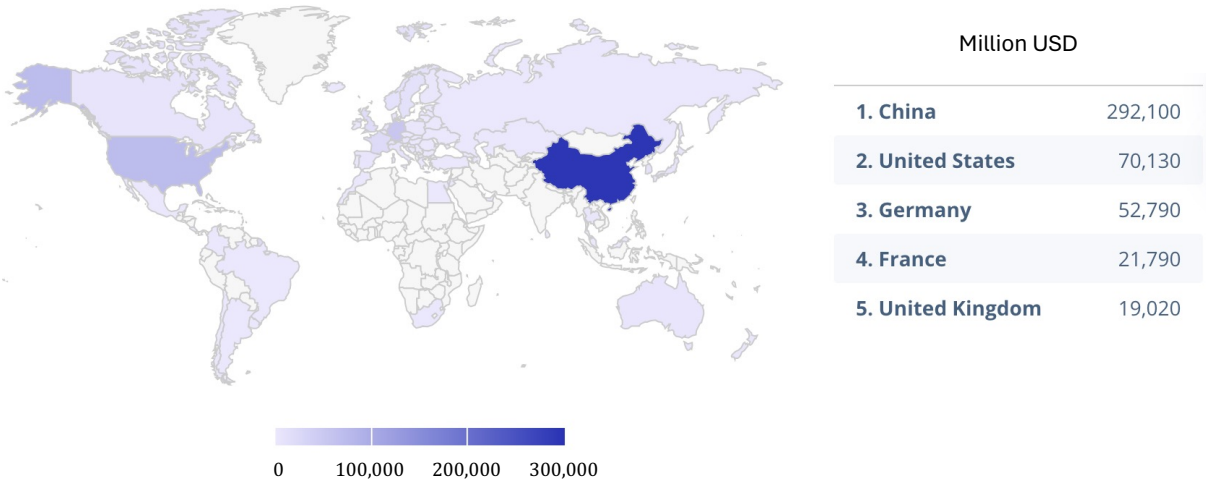

FIGURE 1.4: Ranking of the top five countries in terms of revenue generated from electric vehicles in 2023 [4].

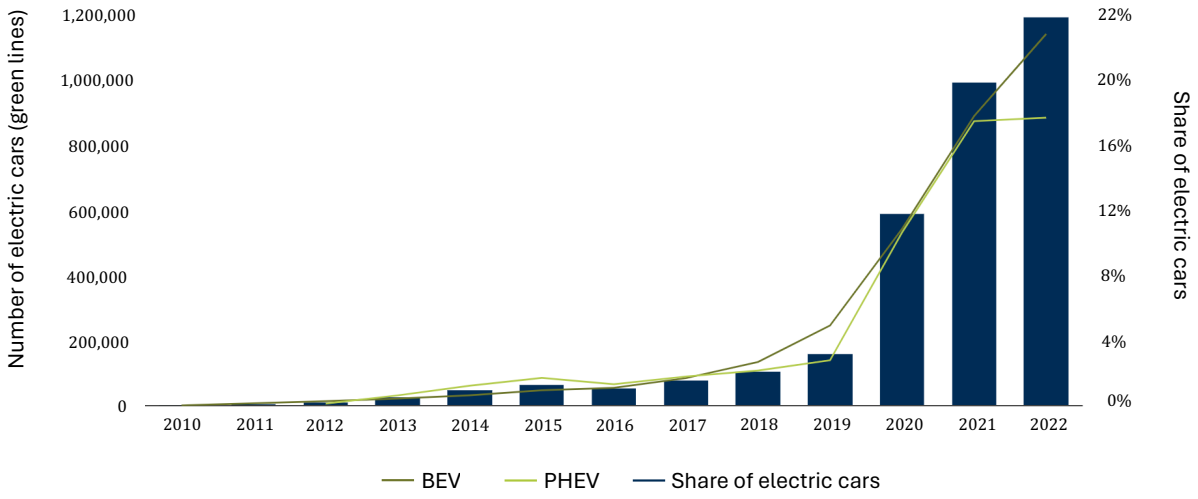

FIGURE 1.5: Volume and share of electric cars sales in Europe [4].

approximately 64% of the total number of newly registered BEVs among the EU-27 and non-EU EEA nations. The greatest percentages of PHEV sales were recorded in Finland (20%), Iceland (23%), and Sweden (23%). The proportion of EVs registered in the total fleet of four European countries (Cyprus, Poland, Czechia, and Slovakia) remained below 5%.

1.1.3 Italian Trend

Italian consumers are becoming increasingly attracted to EVs because of their environmental benefits. Due to the rising awareness of climate change and air pollution, more and more people are looking for eco-friendly alternatives to traditional gasoline-powered automobiles. The data depicted in Fig. 1.7 suggests that the mean quantity of EVs in circulation remained reasonably stable at 125 million from 2021 to 2023. This statistic is over eight times greater than the value

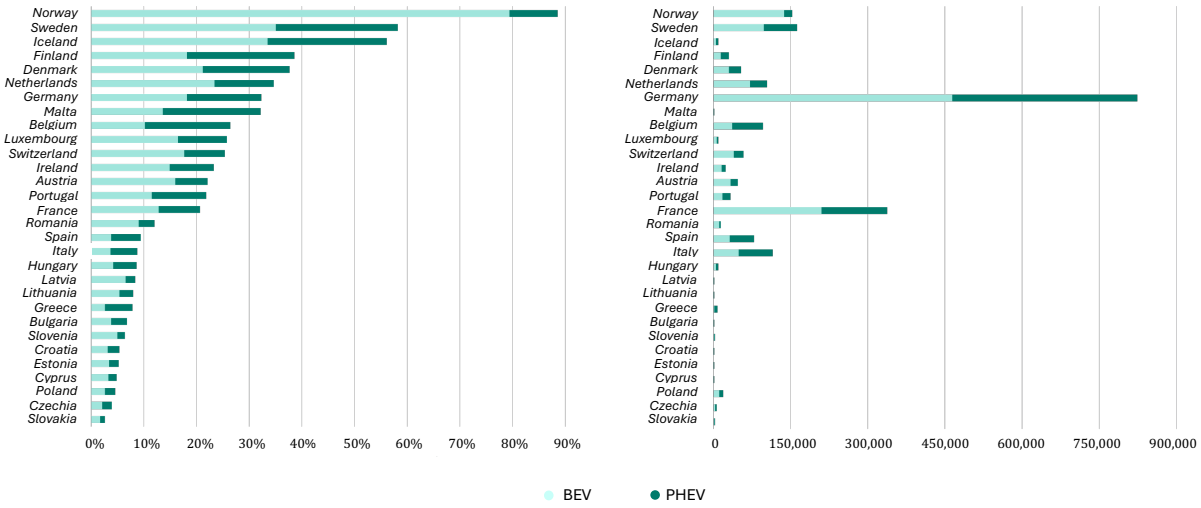

FIGURE 1.6: Percentage (left figure) and number (right figure) of registered electric cars (BEV and PHEV) in the EU-27 and non-EU EEA countries (i.e. Iceland, Norway and Switzerland) in 2022 [4].

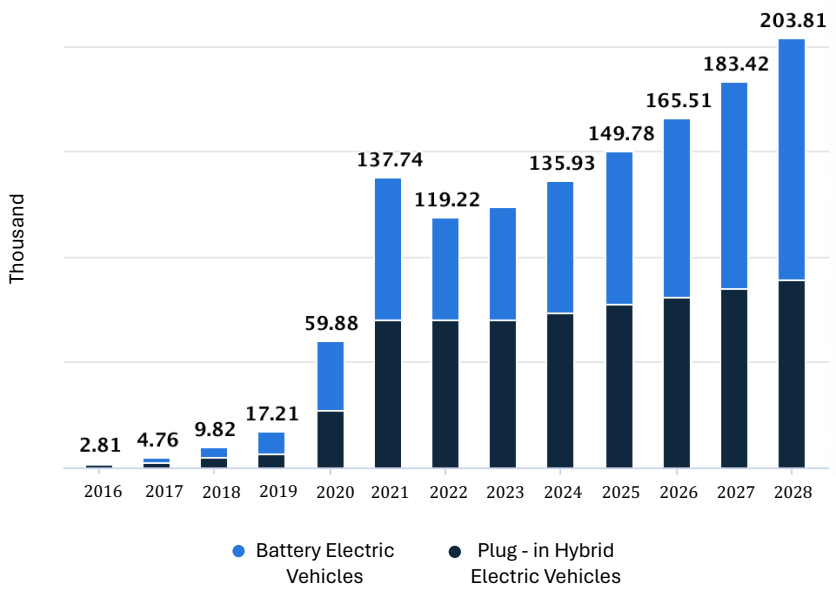

FIGURE 1.7: Vehicles sales in Italy [4].

recorded in 2019 and three times higher than the value recorded in 2020. Further projections indicate that the upward trajectory continues, with the number of vehicles on the highways expected to reach a maximum of 203,800 by 2028.

By 2024, it is anticipated that the EVs market in Italy will generate revenue of 7.5 billion euros. With a Compound Annual Growth Rate (CAGR) of 10.13% from 2024 to 2028, the market is expected to reach 11.0 billion euros in volume by that year. Following this trend, the sales of EVs are projected to hit 203,800 units by the year 2028. Additionally, the volume-weighted average price of a BEVs in the Italian market is expected to reach 54.1k euros by 2024 [4].

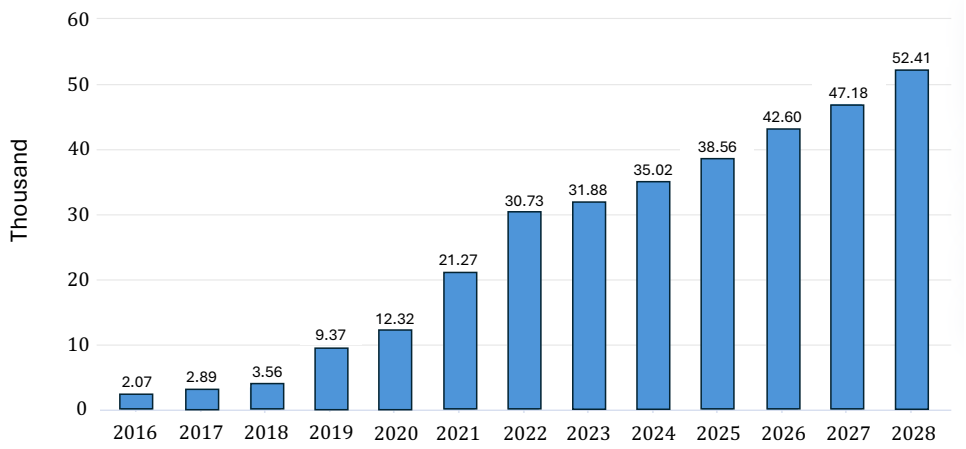

FIGURE 1.8: Number of charging stations in Italy [4].

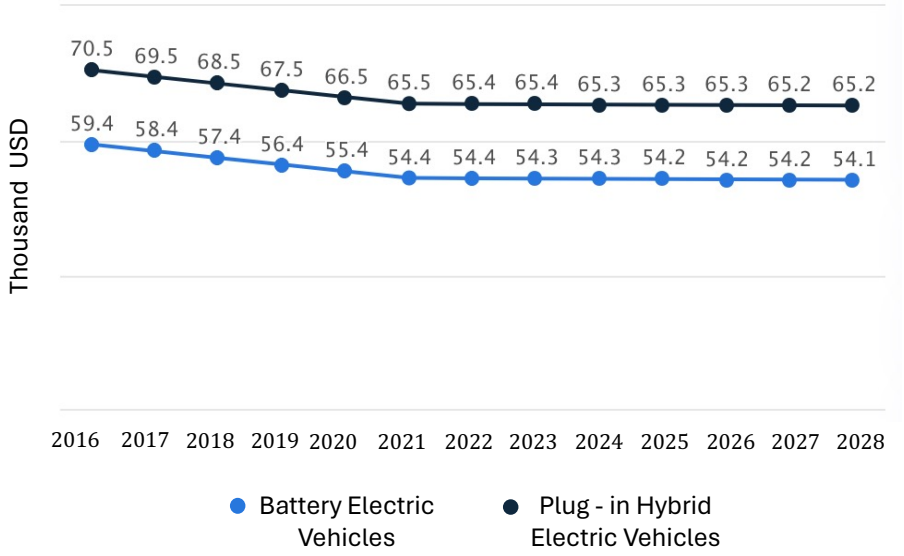

FIGURE 1.9: Average price of BEVs and PHEVs in Italy [4].

One factor contributing to the expansion of the electric vehicle market in Italy is the government's initiative to strategically increase the number of charging stations (see Fig. 1.8). This development has enabled the alleviation of concerns related to range anxiety and has motivated a wider range of individuals to consider purchasing EVs. According to projections, the number of charging stations in Italy will reach 52.41 million by 2028, which is approximately 60% more than the current count and four times greater than what was recorded in 2020.

1.2 Permanent Magnet Motors Market Share

The International Renewable Energy Agency (IRENA) has documented a consistent increase in the utilization of PM[1] motors in recent years. Fig. 1.10 depicts a twofold increase in the quantity of EVs incorporating PM motors from 2020 to 2023. By 2030, the projected number of

[1] A thorough description of magnetic circuits is provided in Appendix A.

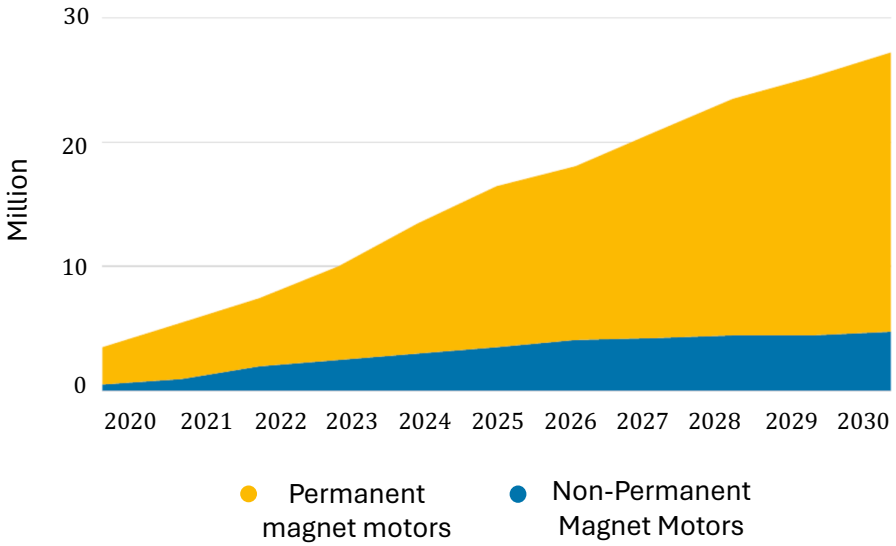

FIGURE 1.10: Projection for rare-earth permanent magnet motors use in electric vehicles.

units is expected to reach 28 million. Forecasts indicate that by 2030, the quantity of vehicles equipped with PM motors will be approximately four times greater than the quantity of vehicles equipped with motors that do not utilize magnets.

The primary factors that contribute to the diffusion of PMSMs are mostly due to their high power density and reliability [6]. Moreover, the need for PM motors is propelled by benefits, such as the ability to operate at elevated temperatures with low losses. In addition, PMSMs exhibit a substantial improvement in torque generation, when compared to induction motors, along with a faster rate of acceleration and deceleration.

Due to their outstanding efficiency, PMSMs find wide use in power steering, regenerative braking generators, drive motors, and stop-start motors. Furthermore, they are frequently employed to enhance the performance of electric drives across a range of industrial contexts such as forklifts, robots, blower motors, switchers installed on railroads, tracks, crossing gates, marine pumps, and amusement systems.

1.2.1 Current and Prospective Trend

The primary driver of the global PM motor market is industrial demand. The market has observed an increase in the need for energy-efficient motors and an expanding mandate for the application of PM motors across various sectors, including the automotive industry.

The global PM market is expected to grow at a CAGR of 9.5% from 2021 to 2026, resulting in an increase from 34.5 billion USD to 54.1 billion USD [7]. The factors fueling this expansion encompass a surge in demand from various industrial applications and the automotive industry, with the Asia Pacific area being one of the most significant contributors [8]. The U.S. Department

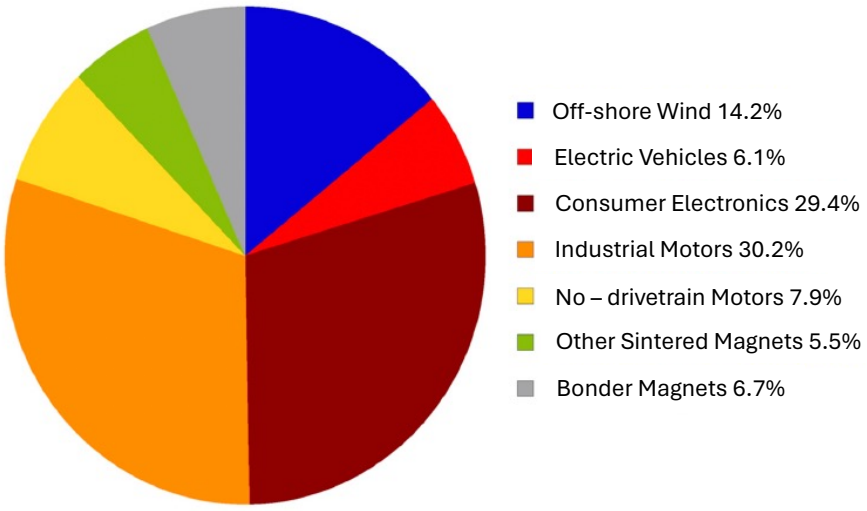

FIGURE 1.11: NeFeB demand by sector, 2020.

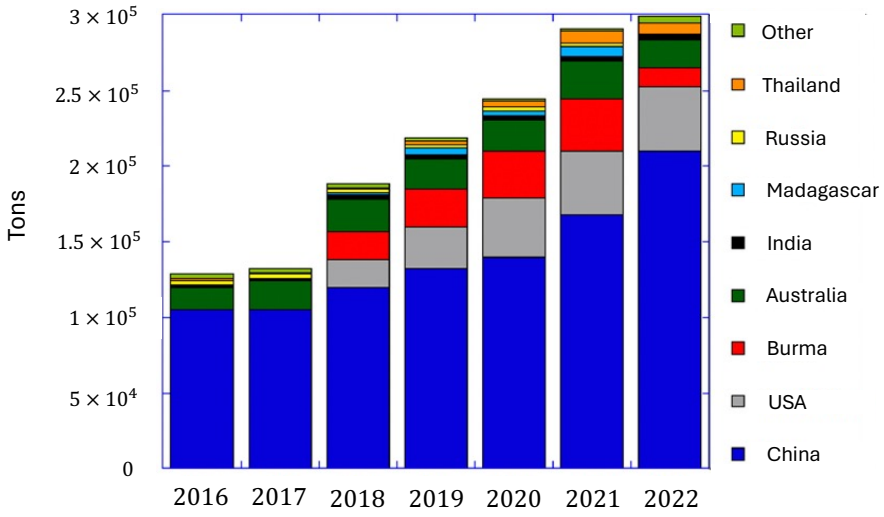

FIGURE 1.12: Annual REE production by country.

of Energy (DOE) provides data on the end-use sectors that shown the highest demand for PMs in the year 2020, as depicted in Fig. 1.11.

PMSMs employ PMs to generate the rotating magnetic field required for the generation of torque. The composition of PMs consists of alloys with Rare-Earth Elements (REEs), which have unique optical and magnetic properties. Magnets accounted for 34% of the demand for REEs in 2019, according to IHS Markit. By 2030, magnets are predicted to constitute approximately 40% of total demand [9]. If that forecast proves accurate, demand for key magnetic REEs may far exceed supply by the end of this decade. Batteries and catalysts accounted for 8% and 20%, respectively, of REE demand in 2020 (see Fig. 1.11).

Fig. 1.12 presents a summary of REE production data covering from 2016 to 2022, as published by the U.S. Geological Survey. China is becoming an increasingly dominant force in the annual production of REEs.

The North American region represents the second-largest market share globally due to the influence of countries such as the United States, Canada, and Mexico, which stimulate market interest in this area.

1.2.2 Neodymium-iron-boron

As previously anticipated, PMs are composed by REEs, with neodymium-iron-boron (NdFeB) and samarium cobalt (SmCo) playing a significant role. The decision to select these types of materials is driven by their significant maximum energy product, which serves as a reliable measure of their efficiency and ability to resist demagnetization [10].

Among PMSMs, those including NdFeB magnets (also known as NIB or Neo magnet) have emerged as the favored option, since their introduction on the market in 1984, for numerous applications, such as the automotive one, due to their ability to produce an high magnetic field [11]. Moreover, NdFeB PMs are widely regarded as the most optimal magnets now accessible, owing to their exceptional energy product. This characteristic makes them highly effective and well-suited for lightweight mobile applications. As a result, they find extensive application in wind turbines, BEVs and PHEVs, household electrical appliances, computer hard disk drives, and various small consumer electronic gadgets [12].

In 2019, the global production of NdFeB magnets amounted to around 130,000 metric tons, which corresponds to a market volume of 6.5 billion USD. Notably, China accounted for nearly 93% of the total sourcing and production of these magnets [13].

1.3 Conclusions

This chapter provided a comprehensive analysis of the global, European, and Italian markets for electric cars and electric motors. Moreover, it has been emphasized how permanent magnet motors are the preferred choice due to their superior performance and reliability in comparison to induction motors.

Bibliography

[1] [Online]. Available: https://www.iea.org/reports/world-energy-outlook-2023/context-and-scenario-design

[2] M. Rísquez Ramos and M. E. Ruiz-Gálvez, "The transformation of the automotive industry toward electrification and its impact on global value chains: Inter-plant competition, employment, and supply chains," *European Research on Management and Business Economics*, vol. 30, no. 1, p. 100242, 2024.

[3] R. Casper and E. Sundin, "Electrification in the automotive industry: effects in remanufacturing," *Journal of Remanufacturing*, vol. 11, no. 2, pp. 121–136, 2021.

[4] [Online]. Available: https://www.statista.com/outlook/mmo/electric-vehicles/italy?currency=EUR

[5] "European environmental agency." [Online]. Available: https://www.eea.europa.eu/en/analysis

[6] M. S. Rafaq, H. Lee, Y. Park, S. B. Lee, D. Fernandez, D. Diaz-Reigosa, and F. Briz, "A simple method for identifying mass unbalance using vibration measurement in permanent magnet synchronous motors," *IEEE Transactions on Industrial Electronics*, vol. 69, no. 6, pp. 6441–6444, 2022.

[7] "Permanent magnet market size share analysis - growth trends forecasts (2024 - 2029)," *Mordor Intelligence Research Advisory*, 2023.

[8] J. W. Heim and R. L. Vander Wal, "Ndfeb permanent magnet uses, projected growth rates and nd plus dy demands across end-use sectors through 2050: A review," *Minerals*, vol. 13, no. 10, 2023. [Online]. Available: https://www.mdpi.com/2075-163X/13/10/1274

[9] D. Gielen and M. Lyons, "Critical materials for the energy transition: Rare earth elements," 05 2022.

[10] B. Podmiljšak, B. Saje, P. Jenuš, T. Tomše, S. Kobe, K. Žužek, and S. Šturm, "The future of permanent-magnet-based electric motors: How will rare earths affect electrification?" *Materials*, vol. 17, no. 4, 2024. [Online]. Available: https://www.mdpi.com/1996-1944/17/4/848

[11] H.-J. Lee, J. Jeong, M. O. Zapico, S. B. Lee, D. D. Reigosa, and F. B. del Blanco, "Airgap flux search coil-based estimation of permanent magnet temperature for thermal protection of pmsms," *IEEE Transactions on Industry Applications*, vol. 60, no. 1, pp. 367–376, 2024.

[12] Y. Yang, A. Walton, R. Sheridan, K. Güth, R. Gauß, O. Gutfleisch, M. Buchert, B.-M. Steenari, T. Van Gerven, P. T. Jones, and K. Binnemans, "Ree recovery from end-of-life ndfeb permanent magnet scrap: A critical review," *Journal of Sustainable Metallurgy*, vol. 3, no. 1, pp. 122–149, 2017.

[13] "United states geological survey. rare earths statistics and information. 2023." [Online]. Available: https://www.usgs.gov/centers/national-minerals-information-center/rare-earths-statistics-and-information

Chapter 2

Multiphase Electric Drives

This chapter delineates the main advantages of multiphase machines compared to their three-phase equivalents. The benefits of an increased number of phases in an electric drive system are emphasized, especially regarding performance and reliability. In addition, the Vector Space Decomposition (VSD) is illustrated since it facilitates the control of multiphase drives.

2.1 Introduction to Multiphase Electric Drives

Multiphase drives are an intriguing technology that distributes power throughout more than three phases (see Fig. 2.1), making them well-suited for high-power applications. Multiphase motor drives offer various advantages over typical three-phase drives with same power, including improved torque quality and reduced stator current per phase [1; 2]. An increased number of phases correlates to a greater number of degrees of freedom [3], which can be efficiently employed to enhance the drive's tolerance to electrical faults or to increase the torque density [4; 5].

2.1.1 State of The Art

Three-phase motors are very suitable for use as traction motors in electric vehicles. In conventional applications, their maximum output power can reach 400 kW, while their rotational motor speed can reach up to $25,000$ Revolutions Per Minute (RPM).

Despite their outstanding performance, three-phase motor drives are subject to certain limitations. For example, they are weak in terms of torque and power production for some electric propulsion applications, such as aircraft and heavy machinery. In fact, as the torque requirement

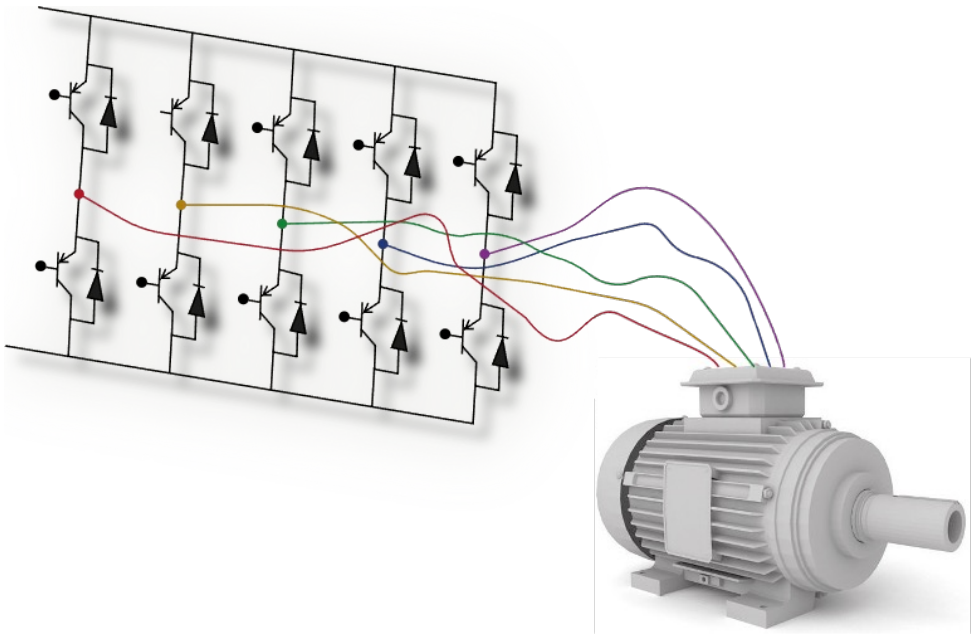

FIGURE 2.1: Multiphase drive.

increases, the magnitude of the currents flowing into the power converter increases, resulting in a significant stress for the power electronic components. In a multiphase converter, the power is divided among multiple phases, thereby reducing the risk of overheating and extending the lifespan of the components.

Finally, three-phase electrical drives possess a restricted capacity for handling faults; in the event that any of the three phases fails, the motor experiences a loss of torque and ceases operation. On the other hand, a multiphase drive may continue to operate even if one of the phases fails, albeit with reduced performance [6–9]. Therefore, in applications requiring a high degree of reliability, multiphase Alternating Current (AC) electrical machines may progressively supplant three-phase machines as a result of developments in power electronics [10–13] and data processing.

Based on their characteristics, the main current and future uses of multiphase drives are in aerospace applications, hybrid an battery electric vehicles, ship propulsion, locomotive traction, wind turbine generation (primarily for remote offshore applications with high-voltage direct current connection to the shore), and high-power industrial applications in general [14].

A five-phase motor has been developed (see Fig. 2.2) by Daniel Vicario and Siavash Sadeghi, who founded Optiphase Drive Systems (ODS), with the aim to overcome the constraints of three-phase motors and broaden the application of electric vehicles beyond just small and light vehicles [15].

According to the researchers of the Power Electronics Innovation Center (PEIC),Polytechnic University of Turin, multi three-phase drives are increasingly being used in practical applications due to their ability to be fed by standard three-phase inverters in a modular manner [16].

FIGURE 2.2: A sneak peek at the integrated system in development at ODS that combines the company's five-phase motor and controller in one compact design.

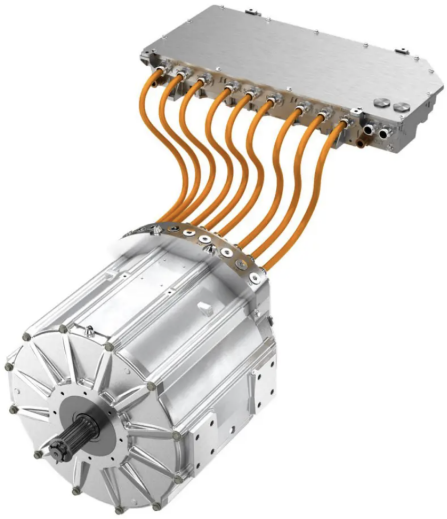

FIGURE 2.3: TM4 SUMO MD nine-phase motor proposed by Dana TM4.

Dana TM4, a collaboration between Dana Incorporated and Hydro-Québec, states that "multi-phase topology systems offers multiple benefits both technically and economically with the added bonus of facilitating vehicle integration due to the reduction in component size and bulk" [17]. The company offers a variety of multiphase motor options, including the one shown in Fig. 2.3.

As anticipated, multiphase drives are suitable for applications that necessitate high torque densities and high reliability. In this context, the Hyundai's nine-phase ultrahigh-speed elevator (see Fig. 2.4)[18] can be mentioned as an outstanding application of a multiphase drive.

The EVs market is progressing toward the adoption of multiphase design. Here are some examples:

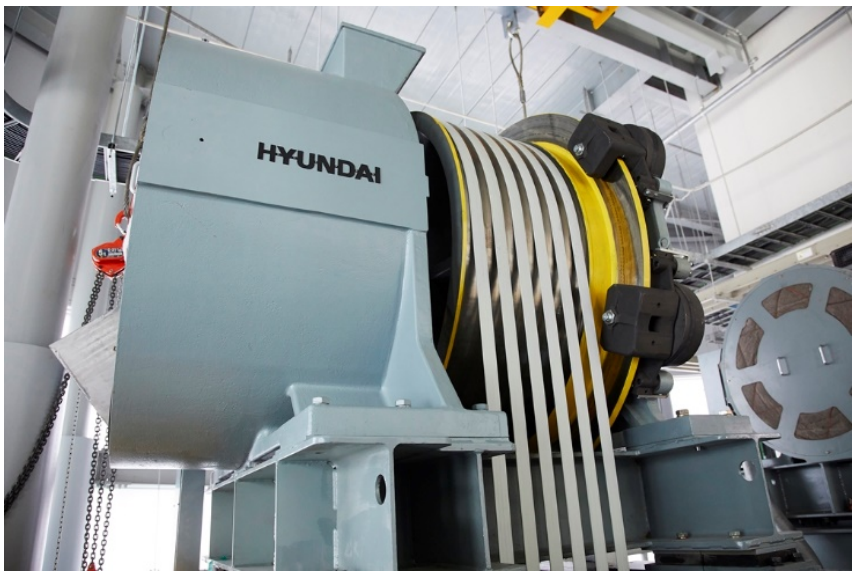

FIGURE 2.4: Nine-phase permanent magnet synchronous machine with three isolated neutral points.

- **BMW iX M60**: "...the iX M60's rear motor can now take 1,200 amps. It does this by adding a second full set of three-phase windings around an extended stator in the rear motor..." [19].
- **Mercedes-Benz EQS**:"...the motor on the rear axle is particularly powerful due to six-phase operation: two windings with three phases each..." [20].
- **Mercedes-Benz EQE**: "... the six-phase electric motor has an output of 215 kW, and Mercedes gives the maximum torque as 565 Nm..." [21].
- **KIA Motors EV6 GT**: "...the rear-mounted electric motor uses two inverters. Each (...) delivers its three-phase current to only half of the hairpin windings..." [22].
- **NASCAR**: "...three six-phase electric motors, with one mounted up front and the other two in the rear..." [23].
- **AUDI AG e-tron FE07**: "...a six-phase, motor-based, single-speed drivetrain..."[24].
- **Ford & STARD SuperVan 4.2**: "...three high-power, six-phase electric motors..." [25].
- **Škoda Auto**: "...the design of the five-phase IPMSM (...) to achieve maximum performance, reduce weight, and increase efficiency, all within the limited space in the vehicle chassis..." [26].
- **Motiv Electric Trucks & Nidec Motor Corporation**: "...a six-phase motor and motor controller featuring torque that surpasses counterparts" [27].

2.1.2 Multiphase Drives Classification

The classification of multiphase drives is based on two key characteristics: the number of phases N and how the phases are are connected (single neutral point or multiple neutral points).

A first type, also known as multi three-phase, is characterized by a number of phases multiple of three. The multiphase drives belonging to this group can be configured in either a symmetrical multi-three-phase arrangement, where a single neutral point is used, or in an asymmetrical configuration, where each three-phase subset of windings is connected to its own neutral point. The term "asymmetrical" derives from the fact that each subset of windings is shifted by a specific angle from the preceding one. Conversely, for drives with an odd number of phases, the sole feasible phase connection is a single neutral point, as there are no subsets of windings that form an independent three-phase layout.

Regardless of the drive's architecture, the complexity of the system grows as the number of phases increases. As a result, the most commonly used multiphase drives, with the exception of particular applications, typically do not have more than nine phases. Fig. 2.5 illustrates the potential configurations of a multiphase electric drive.

Induction motor and PM solutions have been the focus of most research on multiphase drives. Motors using PMs are commonly used in the automotive sector because of their higher torque density compared to induction motors. Moreover, the weight and size of an induction motor is significantly larger than those of a PM synchronous motor with the same power. Lastly, in comparison to synchronous machines, induction motors often have increased rotor joule losses, leading to reduced efficiency [28].

Conversely, the ability to directly link the motor to the grid makes multiphase induction motor drives ideal for applications such wind turbines. In this context, it is worth to mention the use of the open-end winding layout [29].

PM multi-three-phase drives are a compelling solution for industry because they may be viewed as a set of three-phase units working in parallel and feeding the same machine. As a result, the power converter may be designed as a set of multiple three-phase power modules, leading to considerable savings in size, cost, and design time [30–32].

Multi-three-phase drives can be categorized in asymmetrical [33] and symmetrical [34]. Several studies have been conducted to determine which architecture provides the most benefits. Research on asymmetrical topology indicates that this drive configuration results in reduced torque oscillations. On the other hand, the symmetrical form seems to exhibit a reduction in the total current harmonic distortion [35].

Undoubtedly, the study of multi three-phase drives is currently exerting a significant influence in both academic research and industrial applications, emerging as one of the most promising

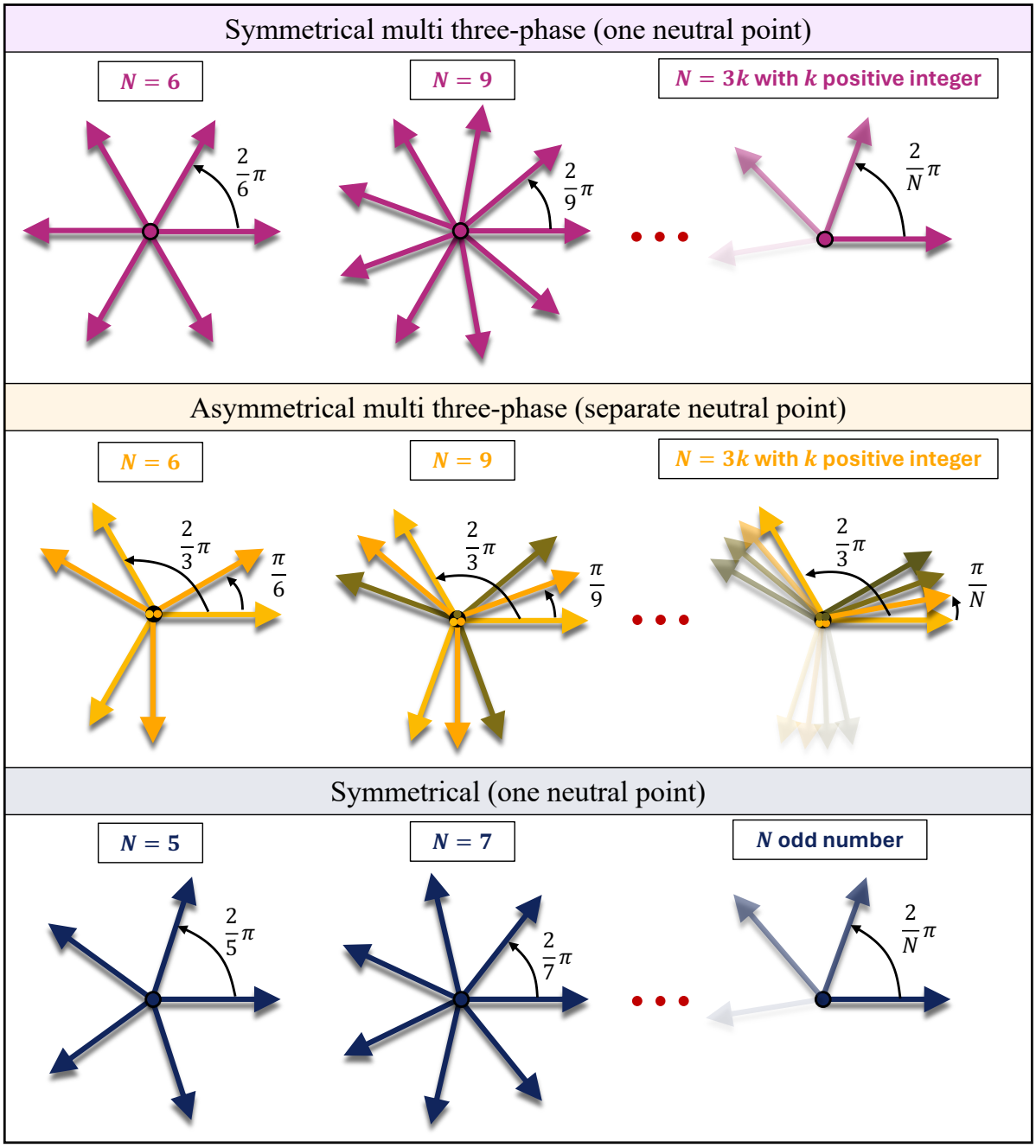

FIGURE 2.5: Typologies of multiphase drives.

choices for the future.

2.2 Vector Space Decomposition Approach

As previously stated, the complexity of a multiphase drive rises as the number of phases increases. This issue has prompted the research community to consider an alternative methodology for handling them.

The VSD approach is a general-purpose solution, which can be applied to multiphase electric drives, that becomes increasingly valuable as the number of variables describing the system

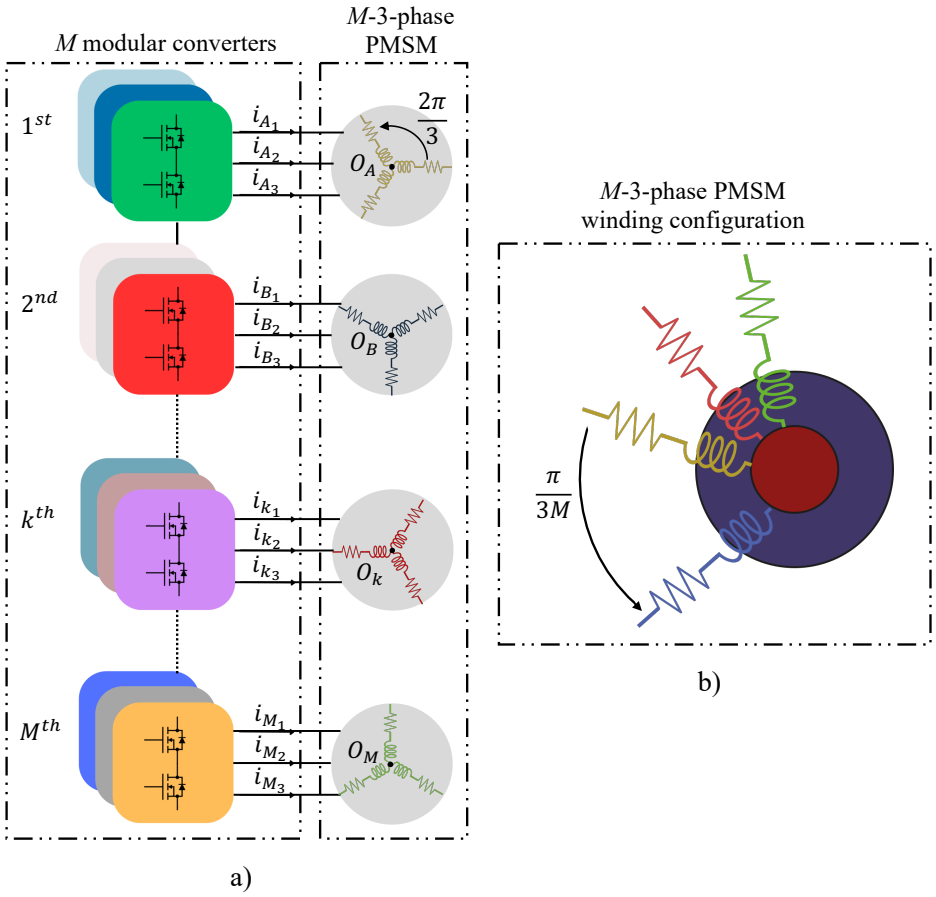

FIGURE 2.6: Asymmetrical multi three-phase drive scheme with distinct neutral points. a) Multi three-phase converter. b) Multi three-phase motor.

increases [36].

Fortescue in 1918 was the first to establish the basis for VSD in his key publication [37]. In this work, he demonstrated that it was feasible to transform a single system with a generic number of variables into multiple symmetrical sub-systems without losing the information content.

The VSD relies on the concept of "space vectors". They can be visualized as vectors lyingon distinct planes.

2.2.1 Odd Number of Real Variables

Assuming N is an odd number, by using the VSD, for a given set of N-odd real variables $(x_1, ..., x_k, ..., x_N)$, a new set of complex variables $\bar{y}_0, ..., \bar{y}_\rho, ..., \bar{y}_{N-1}$ can be obtained by means of the following symmetrical linear transformations known as extended Clarke's transformation:

$$\bar{y}_\rho = \frac{2}{N} \sum_{k=1}^{N} x_k \bar{\alpha}^{\rho(k-1)} \quad \rho = 0, 1, 2, ..., N-1 \tag{2.1}$$

where $\bar{\alpha}$ is a complex number with unit magnitude and phase that is contingent upon the number N of real variables considered, $\bar{\alpha} = e^{j\frac{2\pi}{N}}$.

It is often advantageous to rotate the variables described in equation (2.1) by a specific angle θ. The transition from the $\alpha_\rho - \beta_\rho$ plane of y_ρ to the new plane, commonly known as the $d_\rho - q_\rho$ plane, is called the Park transformation and is defined as follows:

$$\bar{y}'_\rho = \bar{y}_\rho e^{-j\theta} \quad \rho = 0, 1, 2, ..., N-1. \tag{2.2}$$

Thus, by performing the Park transformation, the two components of $\bar{y}_\rho$, namely y_{ρ_α} and y_{ρ_β}, can be transformed into y_{ρ_d} and y_{ρ_q}.

The relationship (2.1) results in a real variable $\bar{y}_0 = y_0$, known as zero-sequence component (or homopolar component), and $N-1$ complex variables $\bar{y}_1, ..., \bar{y}_\rho, ..., \bar{y}_{N-1}$ (multiple space vectors). The VSD is a bidirectional transformation process. Specifically, given the multiple space vectors and the zero-sequence component, it is always feasible to obtain the values of x_k by using the following inverse-transformation:

$$x_k = \sum_{\rho=0}^{N-1} \bar{y}_\rho \bar{\alpha}^{\rho(k-1)} \quad k = 1, 2, ..., N. \tag{2.3}$$

According to (2.3), the transition from the set of real variables x_k to the set of complex variables $\bar{y}_\rho$ introduces redundancy because multiple space vectors have both real and imaginary components. As a result, it has significance to determine the minimum number of multiple space vectors required to eliminate the aforementioned redundancy. This task can be accomplished by exploiting the Hermetian function property of the space vector that allows to assert the following:

$$y_{N-\rho} = y^*_\rho. \tag{2.4}$$

As a consequence of (2.4), (2.1) can be rewritten as:

$$\bar{y}_\rho = \frac{2}{N} \sum_{k=1}^{N} x_k \bar{\alpha}^{\rho(k-1)} \quad \rho = 0, 1, 3, 5, ..., N-2. \tag{2.5}$$

The anti-transformation becomes:

$$x_k = \frac{1}{2} y_0 + \sum_{\rho_{odd}}^{N-2} \bar{y}_\rho \cdot \bar{\alpha}^{\rho(k-1)} \quad k = 1, 2, ..., N. \tag{2.6}$$

Expression (2.6) shows the interpretation of the variables x_k as a result of two contributions: the first originating from the zero-sequence component and the second from the multiple space vectors. The latter are referred to as null-sum components and represent the projection of the space vector onto N straight lines passing through the origin, rotated by $\frac{2\pi}{N}$ with respect to the real axis. Based on that, (2.6) is often rewritten as follows:

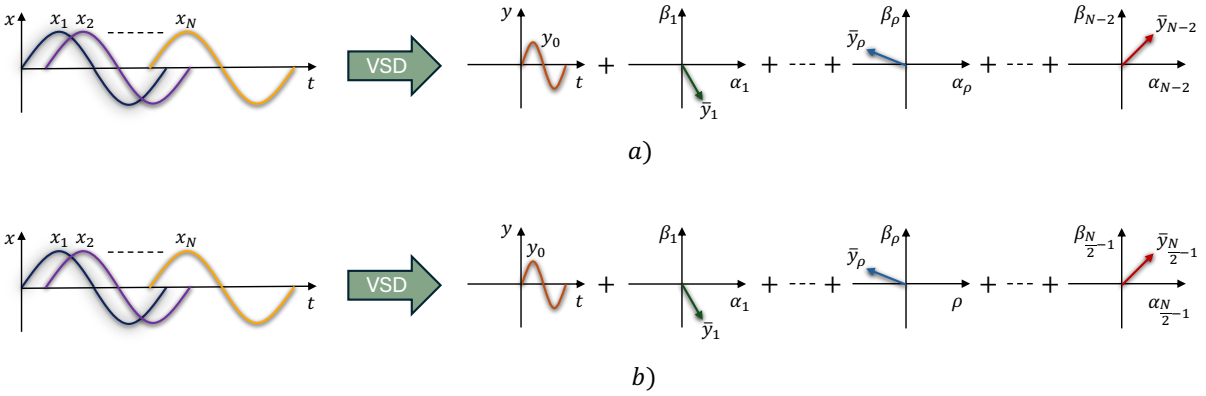

FIGURE 2.7: Vector space decomposition. a) Odd number of real variables. b) Even number of real variables

$$x_k = \frac{1}{2} y_0 + \sum_{\rho_{odd}}^{N-2} \Re_e\{\bar{y}_\rho \bar{\alpha}^{\rho(k-1)}\} \quad k = 1, 2, ..., N. \tag{2.7}$$

Resuming, through the VSD a system consisting of N-odd real variables $(x_1, ...x_k, ...x_N)$ can be fully described by $N-2$ space vectors, whose trajectory lies on the corresponding ρ-th plane (or ρ-th space), and a zero-sequence component (see Fig. 2.7a).

2.2.2 Even Number of Real Variables

The most widespread machines characterized by an even number of phases are multi-three-phase machines such as six-phase and twelve-phase machines. As depicted in Fig. 2.5, the multi-three-phase design may be symmetrical or asymmetrical; hence, a single equation analogous to (2.1) for the VSD transformation is missing. Consequently, each machine type must be treated individually according to the stator winding arrangement.

2.2.3 Vector Space Decomposition for Dual-Three-Phase Electrical Machines

The majority of electric vehicles (EVs) that employ a multiphase drive prefer PM dual-three-phase architectures, according to Sec. 2.1.1. These multiphase machines typologies are highly attractive solutions for industry due to the following main reasons:

- They incorporate the advantages of PM motors with those of multiphase motors.
- They can be considered as two three-phase units connected in parallel; consequently, the knowledge learned regarding conventional three-phase machines can be used for their design.
- If one of the three-phase units malfunctions, it is feasible to sustain motor operation by disconnecting the faulty unit if each unit is connected to a separate neutral point.

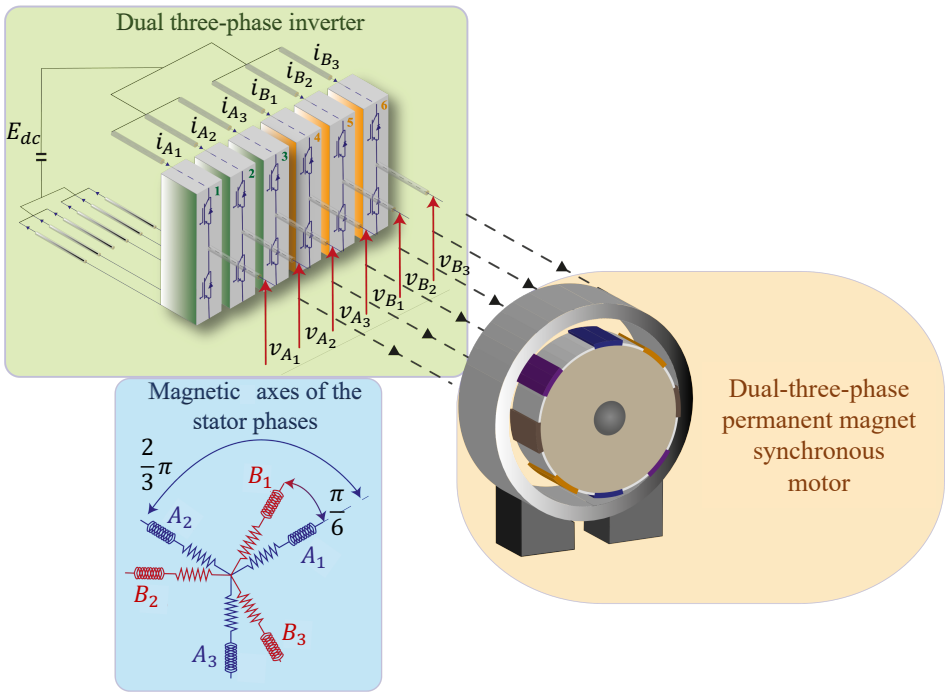

FIGURE 2.8: Asymmetrical dual three-phase permanent magnet electrical drive.

- The control of the motor can be regarded as an extension of the three-phase case.

In an asymmetrical dual-three-phase Permanent Magnet Synchronous Motors (PMSMs), such as the one shown in Fig. 2.8, there are two sets of three-phase windings (A and B) that are positioned with a spatial displacement of 30 electrical degrees. Furthermore, the phases belonging to the same three-phase set of windings are displaced by 120 electrical degrees.

The study of dual-three-phase PMSMs can be approached in two distinctive manners. The first method, known as the vector approach, involves evaluating the whole system, which comprises six distinct phases. The second way entails considering the drive as two sets of three-phase windings, known as a modular approach because the drive is divided into three-phase "modules".

For a dual-three-phase electric drive, equation (2.1) is frequently written in terms of the angle $\bar{\beta} = e^{j\frac{\pi}{6}}$, rather than $\bar{\alpha}$, which corresponds to the spatial displacement between the two sets of three-phase windings. Using β leads to:

$$\bar{y}_\rho = \frac{1}{3}(x_{A_1} + x_{B_1}\bar{\beta}^\rho + x_{A_2}\bar{\beta}^{4\rho} + x_{B_2}\bar{\beta}^{5\rho} + x_{A_3}\bar{\beta}^{8\rho} + x_{B_3}\bar{\beta}^{9\rho}) \quad \rho = 0, 1, 2, ..., N-1. \tag{2.8}$$

In addition, the following symmetry properties are valid for any integer k:

$$\begin{aligned} \bar{y}_{12k+\rho} &= \bar{y}_\rho \\ \bar{y}_{12k-\rho} &= \bar{y}_\rho^* \end{aligned} \tag{2.9}$$

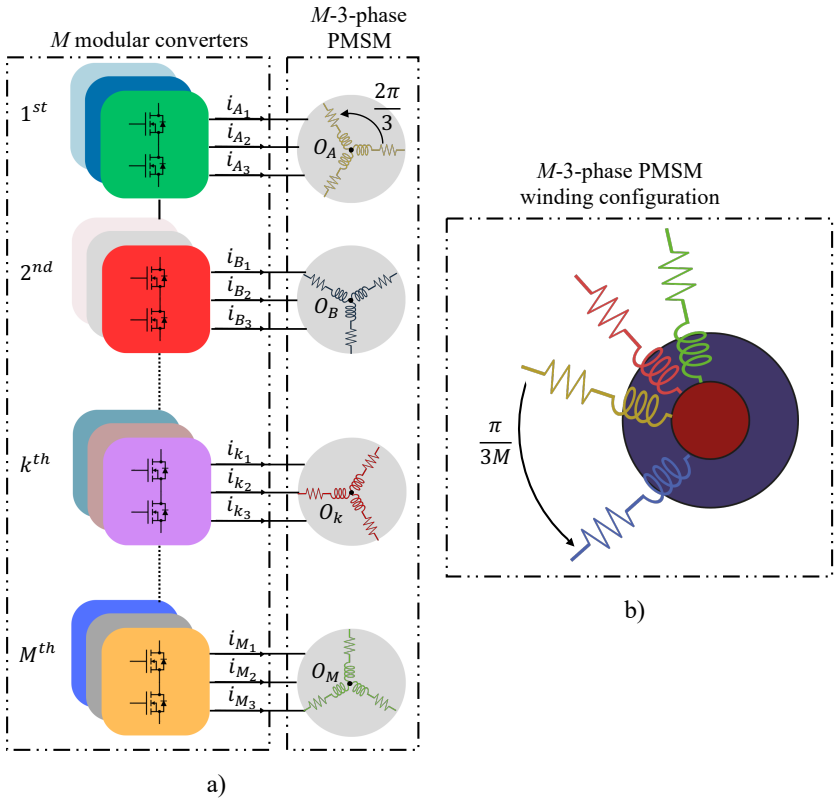

FIGURE 2.9: Asymmetrical multi-three-phase drive scheme with distinct neutral points. a) Multi-three-phase converter. b) Multi-three-phase motor.

where "$*$" is the complex conjugate operator. Equations (2.9) show that the space vectors with $\rho = 1, 3, 5$ are independent and sufficient to unequivocally represent the six quantities $x_{A_1}, x_{A_2}, x_{A_3}, x_{B_1}, x_{B_2}$, and x_{B_3}. As a result, the following transformations con be used:

$$\begin{aligned}
y_0 &= \frac{1}{3}(x_{A_1} + x_{B_1} + x_{A_2} + x_{B_2} + x_{A_3} + x_{B_3}) \\
\bar{y}_1 &= \frac{1}{3}(x_{A_1} + x_{B_1}\bar{\beta} + x_{A_2}\bar{\beta}^4 + x_{B_2}\bar{\beta}^5 + x_{A_3}\bar{\beta}^8 + x_{B_3}\bar{\beta}^9) \\
\bar{y}_3 &= \frac{1}{3}(x_{A_1} + jx_{B_1} + x_{A_2} + jx_{B_2} + x_{A_3} + jx_{B_3}) \\
\bar{y}_5 &= \frac{1}{3}(x_{A_1} + x_{B_1}\bar{\beta}^5 + x_{A_2}\bar{\beta}^8 + x_{B_2}\bar{\beta} + x_{A_3}\bar{\beta}^4 + x_{B_3}\bar{\beta}^9).
\end{aligned} \tag{2.10}$$

The physical interpretation of the real variable $\bar{y}_3$, derived for $\rho = \frac{N}{2}$, can be deduced from equation (2.10). It represents the sum of quantities associated with the first set of three-phase windings and the second rotated by 90 degrees.

Using the modular approach, according to (2.1), the generic quantities x_{A_k} and x_{B_k} $(k = 1, 2, 3)$ of the dual-three-phase drive can be represented as space vectors in two-dimensional spaces $\alpha_\rho - \beta_\rho$, as follows:

$$\bar{y}_\rho = \frac{1}{2}\bar{y}_{A_\rho} + \frac{1}{2}\bar{y}_{B_\rho}\bar{\beta}^\rho \quad \rho = 0, 1, 2, ..., N-1. \tag{2.11}$$

where

$$\begin{aligned}\bar{y}_{A_\rho} &= \frac{2}{3}(x_{A_1} + x_{A_2}\bar{\beta}^{4\rho} + x_{A_3}\bar{\beta}^{8\rho}) \\ \bar{y}_{B_\rho} &= \frac{2}{3}(x_{B_1} + x_{B_2}\bar{\beta}^{4\rho} + x_{B_3}\bar{\beta}^{8\rho}).\end{aligned} \tag{2.12}$$

When ρ is 0, (2.12) provides the zero-sequence components:

$$\begin{aligned}y_{A_0} &= \frac{2}{3}(x_{A_1} + x_{A_2} + x_{A_3}) \\ y_{B_0} &= \frac{2}{3}(x_{B_1} + x_{B_2} + x_{B_3}).\end{aligned} \tag{2.13}$$

Given (2.12) and (2.13), considering (2.9), the following transformations con be used:

$$\begin{aligned}y_0 &= \frac{1}{2}y_{A_0} + \frac{1}{2}y_{B_0} \\ \bar{y}_1 &= \frac{1}{2}\bar{y}_{A_1} + \frac{1}{2}\bar{y}_{B_1}\bar{\beta} \\ \bar{y}_3 &= \frac{1}{2}y_{A_0} + j\frac{1}{2}y_{B_0} \\ \bar{y}_5 &= \frac{1}{2}\bar{y}^*_{A_1} + \frac{1}{2}\bar{y}^*_{B_1}\bar{\beta}^5.\end{aligned} \tag{2.14}$$

It should be noted that the findings in (2.14) are the same as in (2.10), which emphasizes that a dual-three-phase drive may be regarded as a combination of two three-phase units.

The real quantities associated with each set of three-phase windings are obtained from (2.14) by considering (2.12) and (2.13) as follows:

$$\begin{aligned}x_{A_1} &= \Re_e(\bar{y}_3) + \bar{y}_1 \cdot 1 + \bar{y}^*_5 \cdot 1 \\ x_{B_1} &= \Im_m(\bar{y}_3) + \bar{y}_1 \cdot \bar{\alpha} + \bar{y}^*_5 \cdot \bar{\alpha}^7 \\ x_{A_2} &= \Re_e(\bar{y}_3) + \bar{y}_1 \cdot \bar{\alpha}^4 + \bar{y}^*_5 \cdot \bar{\alpha}^4 \\ x_{B_2} &= \Im_m(\bar{y}_3) + \bar{y}_1 \cdot \bar{\alpha}^5 + \bar{y}^*_5 \cdot \bar{\alpha}^{11} \\ x_{A_3} &= \Re_e(\bar{y}_3) + \bar{y}_1 \cdot \bar{\alpha}^8 + \bar{y}^*_5 \cdot \bar{\alpha}^8 \\ x_{B_3} &= \Im_m(\bar{y}_3) + \bar{y}_1 \cdot \bar{\alpha}^9 + \bar{y}^*_5 \cdot \bar{\alpha}^3\end{aligned} \tag{2.15}$$

Equation (2.15) is applicable to both vector and modular approaches. Consequently, throughout the rest of the investigation, both methodologies are used interchangeably to represent the dual-three-phase drive, with the aim of making the notation and algebraic operations as straightforward as possible.

2.3 Conclusions

This chapter covered multiphase electrical drives, emphasizing their advantages compared to common three-phase configuration.

The main architectures of multi-phase electric drive systems have been outlined, emphasizing the multi-tree-phase design as the most attractive option.

The VSD approach has been introduced, which becomes important when the number of phases increases. This approach enables the use of a reduced amount of variables to describe the system, while maintaining the degree of freedom and information content unchanged.

Bibliography

[1] F. Barrero and M. J. Duran, "Recent advances in the design, modeling, and control of multiphase machines—part i," *IEEE Trans. on Ind. Elect.*, vol. 63, no. 1, pp. 449–458, 2016.

[2] M. J. Duran and F. Barrero, "Recent advances in the design, modeling, and control of multiphase machines—part ii," *IEEE Trans. on Ind. Elect.*, vol. 63, no. 1, pp. 459–468, 2016.

[3] E. Levi, "Advances in converter control and innovative exploitation of additional degrees of freedom for multiphase machines," *IEEE Trans. on Ind. Elect.*, vol. 63, no. 1, pp. 433–448, 2016.

[4] M. Mengoni, L. Zarri, A. Tani, L. Parsa, G. Serra, and D. Casadei, "High-torque-density control of multiphase induction motor drives operating over a wide speed range," *IEEE Transactions on Industrial Electronics*, vol. 62, no. 2, pp. 814–825, 2015.

[5] A. G. Yepes, A. Shawier, W. E. Abdel-Azim, A. S. Abdel-Khalik, S. Ahmed, and J. Doval-Gandoy, "General online current-harmonic generation for increased torque capability with minimum stator copper loss in fault-tolerant multiphase induction motor drives," *IEEE Transactions on Transportation Electrification*, vol. 9, no. 3, pp. 4650–4667, 2023.

[6] J. Sun, Z. Zheng, C. Li, K. Wang, and Y. Li, "Optimal fault-tolerant control of multiphase drives under open-phasex002f;open-switch faults based on dc current injection," *IEEE Transactions on Power Electronics*, vol. 37, no. 5, pp. 5928–5936, 2022.

[7] G. Yang, S. Li, H. Hussain, J. Zhang, and J. Yang, "A novel svpwm fault-tolerant strategy for torque ripple reduction of seven-phase induction machines under single-phase open-circuit fault," *IEEE Transactions on Power Electronics*, vol. 38, no. 4, pp. 5217–5229, 2023.

[8] G. Sala, M. Mengoni, G. Rizzoli, M. Degano, L. Zarri, and A. Tani, "Impact of star connection layouts on the control of multiphase induction motor drives under open-phase fault," *IEEE Transactions on Power Electronics*, vol. 36, no. 4, pp. 3717–3726, 2021.

[9] N. K. Nguyen, F. Meinguet, E. Semail, and X. Kestelyn, "Fault-tolerant operation of an open-end winding five-phase pmsm drive with short-circuit inverter fault," *IEEE Transactions on Industrial Electronics*, vol. 63, no. 1, pp. 595–605, 2016.

[10] M. J. Duran, I. Gonzalez Prieto, M. Bermudez, F. Barrero, H. Guzman, and M. R. Arahal, "Optimal fault-tolerant control of six-phase induction motor drives with parallel converters," *IEEE Transactions on Industrial Electronics*, vol. 63, no. 1, pp. 629–640, 2016.

[11] C. Tan, D. Xiao, J. E. Fletcher, and M. F. Rahman, "Carrier-based pwm methods with common-mode voltage reduction for five-phase coupled inductor inverter," *IEEE Transactions on Industrial Electronics*, vol. 63, no. 1, pp. 526–537, 2016.

[12] W. Taha, P. Azer, A. D. Callegaro, and A. Emadi, "Multiphase traction inverters: State-of-the-art review and future trends," *IEEE Access*, vol. 10, pp. 4580–4599, 2022.

[13] L. Vancini, M. Mengoni, G. Rizzoli, L. Zarri, and A. Tani, "Voltage balancing of the dc-link capacitors in three-level t-type multiphase inverters," *IEEE Transactions on Power Electronics*, vol. 37, no. 6, pp. 6450–6461, 2022.

[14] F. Betin, G.-A. Capolino, D. Casadei, B. Kawkabani, R. I. Bojoi, L. Harnefors, E. Levi, L. Parsa, and B. Fahimi, "Trends in electrical machines control: Samples for classical, sensorless, and fault-tolerant techniques," *IEEE Industrial Electronics Magazine*, vol. 8, no. 2, pp. 43–55, 2014.

[15] [Online]. Available: https://optiphasedrive.com/

[16] [Online]. Available: https://www.electricmotorengineering.com/multi-three-phase-drives-are-becoming-more-and-more-widespread/

[17] [Online]. Available: https://www.danatm4.com/5-benefits-of-multi-phase-motors-and-inverters/

[18] [Online]. Available: https://www.hyundaielevator.co.kr/en/technology/tech/speed

[19] [Online]. Available: https://www.motortrend.com/news/2023-bmw-ix-m60-xdrive50-edrive-electric-motors-explained/

[20] [Online]. Available: https://www.electrive.com/2022/08/25/mercedes-launches-sales-of-the-eqe-in-china/

[21] [Online]. Available: https://www.greencarcongress.com/2021/04/20210404-eqs.html

[22] [Online]. Available: https://www.renewableinverter.com/blogev-gt-on-the-road-inside-korea-s/

[23] [Online]. Available: https://www.caranddriver.com/news/a61547194/nascar-electric-prototype-details/

[24] [Online]. Available: https://www.automotivepowpowertrain-technologies/audi-shows-off-lightweight-formula-e-motor-inverter.htm

[25] [Online]. Available: https://www.driving.co.uk/nsport/wild-electric-ford-supervan-4-2-is-ready-to-tackle-pikes-peak-with-1400bhp/

[26] [Online]. Available: https://www.motorindiaonline.in/skoda-group-debuts-at-busworld-2023-with-cutting-edge-urban-mobility-solutions/

[27] [Online]. Available: https://www.thedrive.com/news/heres-how-koenigseggs-dark-matter-electric-motor-makes-800-hp

[28] V. Dmitrievskii, V. Prakht, E. Valeev, A. Paramonov, V. Kazakbaev, and A. Anuchin, "Comparative study of induction and wound rotor synchronous motors for the traction drive of a mining dump truck operating in wide constant power speed range," *IEEE Access*, vol. 11, pp. 68 395–68 409, 2023.

[29] X. Sun, Z. Liu, D. Jiang, and W. Kong, "Multiphase open-end winding induction machine drive with the floating capacitor," *IEEE Transactions on Industry Applications*, vol. 56, no. 5, pp. 5013–5022, 2020.

[30] I. Zoric, M. Jones, and E. Levi, "Arbitrary power sharing among three-phase winding sets of multiphase machines," *IEEE Transactions on Industrial Electronics*, vol. 65, no. 2, pp. 1128–1139, 2018.

[31] A. Femia, G. Sala, M. Mengoni, L. Vancini, G. Rizzoli, L. Zarri, and A. Tani, "Stator imbalance in asymmetrical six-phase synchronous motor drives: High-resistance connections and mismanufactured winding," in *2023 IEEE 14th International Symposium on Diagnostics for Electrical Machines, Power Electronics and Drives (SDEMPED)*, 2023, pp. 172–178.

[32] J. K. Pandit, M. V. Aware, R. Nemade, and Y. Tatte, "Simplified implementation of synthetic vectors for dtc of asymmetric six-phase induction motor drives," *IEEE Transactions on Industry Applications*, vol. 54, no. 3, pp. 2306–2318, 2018.

[33] A. G. Yepes, J. Doval-Gandoy, F. Baneira, and H. A. Toliyat, "Control strategy for dual three-phase machines with two open phases providing minimum loss in the full torque operation range," *IEEE Transactions on Power Electronics*, vol. 33, no. 12, pp. 10 044–10 050, 2018.

[34] D. Glose and R. Kennel, "Continuous space vector modulation for symmetrical six-phase drives," *IEEE Transactions on Power Electronics*, vol. 31, no. 5, pp. 3837–3848, 2016.

[35] A. González-Prieto, I. González-Prieto, A. G. Yepes, M. J. Duran, and J. Doval-Gandoy, "On the advantages of symmetrical over asymmetrical multiphase ac drives with even phase number using direct controllers," *IEEE Transactions on Industrial Electronics*, vol. 69, no. 8, pp. 7639–7650, 2022.

[36] G. Sala, M. Mengoni, G. Rizzoli, L. Zarri, and A. Tani, "Decoupled d–q axes current-sharing control of multi-three-phase induction machines," *IEEE Transactions on Industrial Electronics*, vol. 67, no. 9, pp. 7124–7134, 2020.

[37] C. L. Fortescue, "Method of symmetrical co-ordinates applied to the solution of polyphase networks," *Transactions of the American Institute of Electrical Engineers*, vol. XXXVII, no. 2, pp. 1027–1140, 1918.

Chapter 3

Stator Faults in Asymmetrical Dual-Three-Phase Electrical Machines

This chapter provides a comprehensive analysis of some electrical faults that can occur in a dual-three-phase electric motor. The proposed methodologies can be seamlessly integrated into the control system and have the capability to identify the presence of an electrical failure without the need for any measuring equipment. Thus, the methodologies given provide a solid basis for the online implementation of fault-tolerance control strategies.

3.1 Faults in Electric Motors

An electric drive can experience different forms of failures, including Short Circuits (SCs) [1–5], High-Resistance Connections (HRCs) [6], Manufacturing Defects (MDs), magnet demagnetization [7; 8], eccentricity [9–11], gearbox damages [12], broken bars in squirrel cage induction machines [13]. Among failures, electrical faults play a significant role in the field of fault diagnosis since they are more difficult to identify than mechanical faults. Indeed, mechanical failures produce vibrations and noises that might serve as an early warning sign of the machine's poor health. In contrast, electrical failures frequently produce relatively little noise and often are not visible from the outside of the machine, under a certain level of severity, since they have an effect just on the drive's electrical control variables.

HRCs, MDs, and SCs exhibit comparable behavior by causing distortions in voltages and currents. Furthermore, measuring instruments that have a full scale that is at least equivalent to the rated current or voltage of the machine are not precise enough to measure quantities with small amplitudes. In fact, according to the CEI standards, measuring equipments are categorized into various accuracy classes. The classifications extend from C005 (maximum accuracy) to C5 (minimum accuracy). The classes denote the percentage error value shown by the measuring instrument in relation to the full-scale measurement. Equipment for electrical measurements typically ranges from class C02 to C1. For instance, a current probe with a maximum range of 200 A, denoted by a C02, indicates that while measuring a current of 200 A, it may incur a maximum percentage error of 0.2%. Conversely, if the same probe monitors a current of 50 A, the accuracy decreases. In addition, sensors not only increase the complexity, cost, and size of the whole system, but they can also be obtrusive and their incorrect placement could compromise the results. Some of the failures that the stator winding of a dual-three-phase PMSM may experience are illustrated in 3.1.

It is worth noticing that the models used in Sections 3.1.1, 3.1.2 and 3.1.3 assume that the magnetic saturation of the iron core is negligible, and the linearity principle is satisfied. This assumption is necessary because the iron saturation interferes with the independents of the vector spaces in multiphase machines.

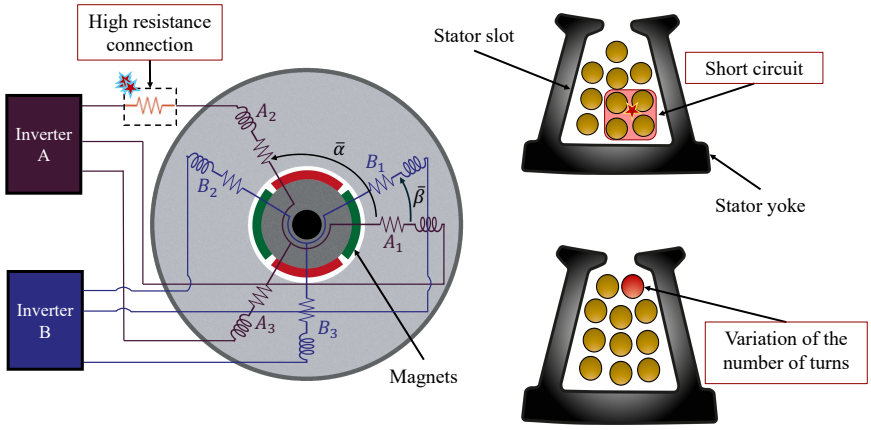

FIGURE 3.1: Stator imbalances in asymmetrical dual-three-phase PMSM.

3.1.1 Equations for High-resistance Connections

The phase equations for a dual-three-phase PMSM are as follows:

$$v_k = R_k i_k + \frac{d\varphi_k}{dt} \quad k = A_1, B_1, A_2, B_2, A_3, B_3 \tag{3.1}$$

where R_k indicate the phase resistances of the k-th phase, whereas i_k and φ_k define the stator current and the flux linkage, respectively.

According to (2.14), the phase voltages are fully described by the following space vectors:

$$\begin{aligned}
\bar{v}_1 &= \frac{1}{2}\bar{v}_{A_1} + \frac{1}{2}\bar{v}_{B_1}\bar{\beta} \\
\bar{v}_5 &= \frac{1}{2}\bar{v}^*_{A_1} + \frac{1}{2}\bar{v}^*_{B_1}\bar{\beta}^5 \\
v_3 &= \frac{1}{2}v_{A_0} - \frac{1}{2}v_{B_0} \\
v_0 &= \frac{1}{2}v_{A_0} + \frac{1}{2}v_{B_0}.
\end{aligned} \tag{3.2}$$

In the same manner the stator phase currents are as follows:

$$\begin{aligned}
\bar{i}_1 &= \frac{1}{2}\bar{i}_{A_1} + \frac{1}{2}\bar{i}_{B_1}\bar{\beta} \\
\bar{i}_5 &= \frac{1}{2}\bar{i}^*_{A_1} + \frac{1}{2}\bar{i}^*_{B_1}\bar{\beta}^5 \\
i_3 &= \frac{1}{2}i_{A_0} - \frac{1}{2}i_{B_0} \\
i_0 &= \frac{1}{2}i_{A_0} + \frac{1}{2}i_{B_0}.
\end{aligned} \tag{3.3}$$

In (3.3), the currents i_{A_0} and i_{B_0} are both zero because of the star-connection arrangement of the three-phase windings constituting the dual-three-phase motor. Therefore, based on (2.15), the inverse transformation of (3.3) is given:

$$\begin{aligned}
i_{A_1} &= \bar{i}_1 \cdot 1 + \bar{i}^*_5 \cdot 1 \\
i_{B_1} &= \bar{i}_1 \cdot \bar{\beta} + \bar{i}^*_5 \cdot \bar{\beta}^7 \\
i_{A_2} &= \bar{i}_1 \cdot \bar{\beta}^4 + \bar{i}^*_5 \cdot \bar{\beta}^4 \\
i_{B_2} &= \bar{i}_1 \cdot \bar{\beta}^5 + \bar{i}^*_5 \cdot \bar{\beta}^{11} \\
i_{A_3} &= \bar{i}_1 \cdot \bar{\beta}^8 + \bar{i}^*_5 \cdot \bar{\beta}^8 \\
i_{B_3} &= \bar{i}_1 \cdot \bar{\beta}^9 + \bar{i}^*_5 \cdot \bar{\beta}^3.
\end{aligned} \tag{3.4}$$

The stator flux vectors $\bar{\varphi}_1$ and $\bar{\varphi}_5$ can be used to express the stator fluxes φ_{A_k} and φ_{B_k}, as follows:

$$\begin{aligned}
\bar{\varphi}_1 &= L_1\bar{i}_1 + \bar{\varphi}_{e_1} \\
\bar{\varphi}_5 &= L_5\bar{i}_5
\end{aligned} \tag{3.5}$$

where $\bar{\varphi}_{e_1}$ is the fundamental excitation flux vector, which is considered sinusoidal, and L_1 and L_5 are the equivalent inductances in subspaces $\alpha_1 - \beta_1$ and $\alpha_5 - \beta_5$, respectively.

The VSD applied to the phase resistances gives:

$$\begin{aligned}
R_{A_1} &= \frac{R_{A_0}}{2} + \bar{R}_1 \cdot 1 + \bar{R}_5^* \cdot 1 \\
R_{B_1} &= \frac{R_{B_0}}{2} + \bar{R}_1 \cdot \bar{\beta} + \bar{R}_5^* \cdot \bar{\beta}^7 \\
R_{A_2} &= \frac{R_{A_0}}{2} + \bar{R}_1 \cdot \bar{\beta}^4 + \bar{R}_5^* \cdot \bar{\beta}^4 \\
R_{B_2} &= \frac{R_{B_0}}{2} + \bar{R}_1 \cdot \bar{\beta}^5 + \bar{R}_5^* \cdot \bar{\beta}^{11} \\
R_{A_3} &= \frac{R_{A_0}}{2} + \bar{R}_1 \cdot \bar{\beta}^8 + \bar{R}_5^* \cdot \bar{\beta}^8 \\
R_{B_3} &= \frac{R_{B_0}}{2} + \bar{R}_1 \cdot \bar{\beta}^9 + \bar{R}_5^* \cdot \bar{\beta}^3.
\end{aligned} \tag{3.6}$$

where $\bar{R}_1$ and $\bar{R}_5$ are complex numbers defined according to (2.12) and (2.14), while R_{A_0} and R_{B_0} are the zero-sequence components resulting from (2.13).

Considering the voltage equations (3.1), multiplying (3.6) with (3.4) and considering the fluxes (3.5), gives:

$$\begin{aligned}
\bar{v}_1 &= \frac{1}{4}[(R_{A_0} + R_{B_0})\bar{i}_1 + \sqrt{2}(\bar{\psi}\bar{R}_1^* + \bar{\psi}^*\bar{R}_5)\bar{i}_1^*] + \frac{d\bar{\varphi}_1}{dt} \\
\bar{v}_5 &= \frac{1}{4}[(R_{A_0} - R_{B_0})\bar{i}_1^* + \sqrt{2}(\bar{\psi}\bar{R}_1 + \bar{\psi}^*\bar{R}_5^*)\bar{i}_1].
\end{aligned} \tag{3.7}$$

where $\bar{\psi}$ is equal to $e^{j\frac{\pi}{4}}$ and $\bar{v}_3 = 0$ since $\bar{i}_3 = 0$. In addition, the control system is expected to keep the current vector $\bar{i}_5$ at zero under all operating conditions, including in the case of a fault.

By applying the Park transformation, as defined in (2.2), and assuming that the motor operates in the maximum torque-per-ampere condition ($i_{d_1} = 0$) [14; 15], the steady state voltage harmonic components are expressed as follows:

$$\begin{aligned}
\bar{v}_{1_R}^{1+} &= \frac{1}{4}j(R_{A_0} + R_{B_0})i_{q_1} - \omega L_1 i_{q_1} + j\omega\bar{\varphi}_{e1} \\
\bar{v}_{1_R}^{1-} &= -\frac{\sqrt{2}}{4}j(\bar{\psi}\bar{R}_1^* + \bar{\psi}^*\bar{R}_5)i_{q_1} \\
\bar{v}_{5_R}^{1+} &= \frac{\sqrt{2}}{4}j(\bar{\psi}\bar{R}_1 + \bar{\psi}^*\bar{R}_5^*)i_{q_1} \\
\bar{v}_{5_R}^{1-} &= -\frac{1}{4}j(R_{A_0} - R_{B_0})i_{q_1}
\end{aligned} \tag{3.8}$$

where the positive-sequence harmonics are indicated by the superscript $+$ and the negative-sequence harmonics are denoted by the superscript $-$, both preceded by the harmonic order. Simultaneously, the subscripted number specifies the specific subspace to which the space vector belongs, while the letter "R" identifies the fault type, specifically a high-resistance connection. For instance, $\bar{v}_{5_R}^{1-}$ represents the first negative-sequence harmonic (superscript $1-$) in the fifth subspace (subscript 5) caused by a resistance imbalance (subscript R).

When no HRC occurs, $\bar{R}_1 = \bar{R}_5 = 0$ and $R_{A_0} = R_{B_0}$ in (3.8). Thus, only the fundamental harmonic component $\bar{v}_{1_R}^{1+}$ exists.

The set of equations in (3.8) can be solved as a function of $\bar{R}_1$ and $\bar{R}_5$, resulting in the following:

$$\begin{aligned}
\bar{R}_1 &= \frac{\sqrt{2}(\bar{\psi}^* \bar{v}_{1_R}^{*1-} - \bar{\psi}\bar{v}_{5_R}^{1+})}{i_{q_1}} \\
\bar{R}_5 &= \frac{\sqrt{2}(\bar{\psi}\bar{v}_{5_R}^{*1+} - \bar{\psi}^* \bar{v}_{1_R}^{1-})}{i_{q_1}} \\
R_{A_0} &= 2j\frac{\bar{v}_{5_R}^{1-}}{i_{q_1}} + 2R_{avg} \\
R_{B_0} &= -2j\frac{\bar{v}_{5_R}^{1-}}{i_{q_1}} + 2R_{avg}
\end{aligned} \tag{3.9}$$

where R_{avg} is the average value of the six resistances R_{A_k} and $R_{B_k} (k = 1, 2, 3)$.

It is worth noting that, according to (3.8), $\bar{v}_{5_R}^{1-}$ is an imaginary number, so the values of R_{A_0} and R_{B_0} are real numbers. Quantities R_{A_0} and R_{B_0} have different amplitudes due to the variation caused by the HRC in one of the two three-phase windings, while $\bar{R}_1$ and $\bar{R}_5$ are complex conjugate when the imbalance affects only one phase.

The phase resistances can be obtained by applying the inverse transformation (3.6) to $\bar{R}_1$ and $\bar{R}_5$ given in (3.9):

$$\begin{aligned}
R_{A_1} &= j\frac{2\sqrt{2}}{i_{q_1}}\Re_e\left[\bar{\psi}^* \Im_m(\bar{v}_{1_R}^{*1-}) + \bar{\psi}\Im_m(\bar{v}_{5_R}^{*1+})\right] + j\frac{\bar{v}_{5_R}^{1-}}{i_{q_1}} + R_{avg} \\
R_{B_1} &= \frac{2\sqrt{2}}{i_{q_1}}\Re_e\left[\bar{\psi}^* \Re_e(\bar{v}_{1_R}^{1-}\bar{\beta}) + \bar{\psi}\Re_e(\bar{v}_{5_R}^{1+}\bar{\beta}^5)\right] - j\frac{\bar{v}_{5_R}^{1-}}{i_{q_1}} + R_{avg} \\
R_{A_2} &= j\frac{2\sqrt{2}}{i_{q_1}}\Re_e\left[\bar{\psi}^* \Im_m(\bar{v}_{1_R}^{*1-}\bar{\beta}^8) + \bar{\psi}\Im_m(\bar{v}_{5_R}^{*1+}\bar{\beta}^4)\right] + j\frac{\bar{v}_{5_R}^{1-}}{i_{q_1}} + R_{avg} \\
R_{B_2} &= \frac{2\sqrt{2}}{i_{q_1}}\Re_e\left[\bar{\psi}^* \Re_e(\bar{v}_{1_R}^{1-}\bar{\beta}^5) + \bar{\psi}\Re_e(\bar{v}_{5_R}^{1+}\bar{\beta})\right] - j\frac{\bar{v}_{5_R}^{1-}}{i_{q_1}} + R_{avg} \\
R_{A_3} &= j\frac{2\sqrt{2}}{i_{q_1}}\Re_e\left[\bar{\psi}^* \Im_m(\bar{v}_{1_R}^{*1-}\bar{\beta}^4) + \bar{\psi}\Im_m(\bar{v}_{5_R}^{*1+}\bar{\beta}^8)\right] + j\frac{\bar{v}_{5_R}^{1-}}{i_{q_1}} + R_{avg} \\
R_{B_3} &= \frac{2\sqrt{2}}{i_{q_1}}\Re_e\left[\bar{\psi}^* \Re_e(\bar{v}_{1_R}^{1-}\bar{\beta}^9) + \bar{\psi}\Re_e(\bar{v}_{5_R}^{1+}\bar{\beta}^9)\right] - j\frac{\bar{v}_{5_R}^{1-}}{i_{q_1}} + R_{avg}.
\end{aligned} \tag{3.10}$$

The control system is capable of determining the voltage harmonic components in (3.10) utilizing resonant PI regulators. However, the equations for the phase resistances still rely on the unknown quantity R_{avg}. Hence, (3.10) can be utilized to calculate the deviation of each resistance from the mean value. If a variation δ_R occurs in phase f of winding A, the expected

resistance deviations from R_{avg} are as follows:

$$\begin{aligned}\Delta R_{A_k} = R_{A_k} - R_{avg} &= \begin{cases} \frac{5}{6}\delta_R, & \text{if } k = f \\ -\frac{1}{6}\delta_R & \text{otherwise} \end{cases} \\ \Delta R_{B_k} = R_{B_k} - R_{avg} &= -\frac{1}{6}\delta_R. \end{aligned} \tag{3.11}$$

Therefore, (3.10) and (3.11) can be used to identify a resistance imbalance due to high-resistance connections.

3.1.2 Variation in the Number of Turns Equations

Incorrect manufacture can result in variations in the number of turns, leading to imbalances in the stator phases, changes in resistance, self- and mutual inductances, and fluctuations in flux linkage. Therefore, it is essential to comprehend the difference in machine parameters between an unbalanced machine and a healthy machine.
In this chapter, in order to simplify the notation and eliminate superfluous subscripts or superscripts, the variables representing the quantities of the healthy machine are indicated in bold.

Defining ε as the ratio of the variation ΔN_t in the number of turns to the total number of turns N_t in a healthy phase, the inductance L_{kh} between the k-th and h-th phases of the faulty machine is given by the following values:

$$L_{kh} = \begin{cases} \boldsymbol{L_{kh}}, & \text{if } k \neq f \vee h \neq f \\ (1+\varepsilon)\boldsymbol{L_{kf}}, & \text{if } k \neq f \vee h = f \\ (1+\varepsilon)^2\boldsymbol{L_{ff}}, & \text{if } k = f \vee h = f. \end{cases} \tag{3.12}$$

The subscripts h and k assume the values A_1, A_2, A_3, B_1, B_2, B_3 and indicate a general stator phase. On the other hand, the subscript f denotes the specific phase in which the MD occurs. Furthermore, the variables associated to the healthy machine are in bold. For instance, $\boldsymbol{L_{A_1B_1}}$ represents the mutual- inductance between the phases A_1 and B_1 under healthy operating conditions (bold letter).

The stator air-gap fluxes for the k-th healthy phase and faulty f phase can be written as follows:

$$\begin{aligned}\varphi_k &= \sum_{\substack{h=1 \\ h\neq f}}^{N} \boldsymbol{L_{kh}} i_h + (1+\varepsilon)\boldsymbol{L_{kf}} i_f \qquad (k \neq f) \\ \varphi_f &= \sum_{\substack{h=1 \\ h\neq f}}^{N} (1+\varepsilon)\boldsymbol{L_{fh}} i_h + (1+\varepsilon)^2\boldsymbol{L_{ff}} i_f. \end{aligned} \tag{3.13}$$

Substituting the definitions (3.12) in (3.13), yields:

$$\begin{aligned} \varphi_k &= \boldsymbol{\varphi_k} + \varepsilon \boldsymbol{L_{kf}} i_f \qquad (k \neq f) \\ \varphi_f &= (1+\varepsilon)(\boldsymbol{\varphi_f} + \varepsilon \boldsymbol{L_{ff}} i_f). \end{aligned} \tag{3.14}$$

It's worth noting that if $i_f = 0$, the only term in (3.34) is $\varphi_k = \boldsymbol{\varphi_k}$, which is the stator flux in healthy operating conditions.

Magnet flux contributions are:

$$\begin{aligned} \varphi_{e,k} &= \boldsymbol{\varphi_{e,k}} \qquad (k \neq f) \\ \varphi_{e,f} &= (1+\varepsilon)\boldsymbol{\varphi_{e,f}}. \end{aligned} \tag{3.15}$$

The stator voltage equations can be written as follows:

$$\begin{aligned} v_k &= R_s i_k + \frac{d}{dt}\varphi_k + \frac{d}{dt}\varphi_{e,k} \qquad (k \neq f) \\ v_f &= (1+\varepsilon) R_s i_f + \frac{d}{dt}\varphi_f + \frac{d}{dt}\varphi_{e,f}. \end{aligned} \tag{3.16}$$

where R_s is the resistance of the stator winding in healthy conditions. Substituting (3.14) and (3.15) in (3.16), gives:

- if $k \neq f$ (healthy phase):

$$\begin{aligned} v_k &= \boldsymbol{v_k} + \Delta v_k \\ \Delta v_k &= \varepsilon \boldsymbol{L_{kf}} \frac{d}{dt} i_f \end{aligned} \tag{3.17}$$

- if $k = f$ (faulty phase):

$$\begin{aligned} v_f &= \boldsymbol{v_f} + \Delta v_f \\ \Delta v_f &= \varepsilon\big[(1+\varepsilon)\boldsymbol{L_{ff}} \frac{d}{dt} i_f + \boldsymbol{v_f}\big] \end{aligned} \tag{3.18}$$

where the equation of the generic k-th healthy phase is give by:

$$\boldsymbol{v_k} = R_s i_k + \sum_{h=1}^{N} \boldsymbol{L_{kh}} \frac{di_h}{dt} + \frac{d}{dt}\boldsymbol{\varphi_{e_k}}. \tag{3.19}$$

According to (2.10), considering a star connection layout of the stator phases, the phase voltages can be fully represented by two space vectors:

$$\begin{aligned} \bar{v}_1 &= \bar{\boldsymbol{v}}_{\mathbf{1}} + \Delta \bar{v}_1 \\ \bar{v}_5 &= \bar{\boldsymbol{v}}_{\mathbf{5}} + \Delta \bar{v}_5 \end{aligned} \tag{3.20}$$

where $\bar{\boldsymbol{v}}_{\mathbf{1}}$ and $\bar{\boldsymbol{v}}_{\mathbf{5}}$ are the voltage space vectors in healthy conditions, whereas $\Delta\bar{v}_1$ and $\Delta\bar{v}_5$ are the voltage variations resulting from the a variation in the number of turns. They assumes the following forms:

$$\begin{aligned}\Delta\bar{v}_1 &= \frac{1}{3}(\Delta v_{A_1} + \Delta v_{B_1}\bar{\beta} + \Delta v_{A_2}\bar{\beta}^4 + \Delta v_{B_2}\bar{\beta}^5 + \Delta v_{A_3}\bar{\beta}^8 + \Delta v_{B_3}\bar{\beta}^9)\\ \Delta\bar{v}_5 &= \frac{1}{3}(\Delta v_{A_1} + \Delta v_{B_1}\bar{\beta}^5 + \Delta v_{A_2}\bar{\beta}^8 + \Delta v_{B_2}\bar{\beta} + \Delta v_{A_3}\bar{\beta}^4 + \Delta v_{B_3}\bar{\beta}^9).\end{aligned} \tag{3.21}$$

Substituting the definition 3.17 and 3.18 in 3.21 leads to the following expressions:

$$\begin{aligned}\Delta\bar{v}_1 &= \frac{1}{3}\varepsilon e^{j\vartheta_f}\left[R_s i_f + (2L_1 + \varepsilon\boldsymbol{L_{ff}})\frac{d}{dt}i_f + \frac{d}{dt}\boldsymbol{\varphi_{e_f}}\right]\\ \Delta\bar{v}_5 &= \frac{1}{3}\varepsilon e^{-j\vartheta_f}\left[R_s i_f + (L_1 + L_5 + \varepsilon\boldsymbol{L_{ff}})\frac{d}{dt}i_f + \frac{d}{dt}\boldsymbol{\varphi_{e_f}}\right]\end{aligned} \tag{3.22}$$

Assuming that the machine rotates at a constant electrical speed ω and the MTPA control is implemented, if the control system keeps the current vector $\bar{i}_5$ at zero under all operating conditions, the stator currents exhibit sinusoidal behavior and are solely determined by the torque-producing component i_{q_1} of the current vector $\bar{i}_1$.

The quantities i_f and $\boldsymbol{\varphi_{e_f}}$ appearing in (3.22) can be written in the following manner:

$$\begin{aligned}i_f &= \Re_e\{j i_{q_1} e^{j(\omega t - \vartheta_f)}\}\\ \boldsymbol{\varphi_{e_f}} &= \Re_e\{\phi_e e^{j(\omega t - \vartheta_f)}\}\end{aligned} \tag{3.23}$$

where ϕ_e is the magnitude of the maximum excitation flux linkage with a generic healthy phase.

Substituting (3.23) in (3.22) and separating the positive and negative sequences of the voltage harmonics, one finds the following result:

$$\begin{aligned}\bar{v}_{1_N}^{1-} &= -\frac{1}{6}j\varepsilon e^{j2\vartheta_f}\{[R_s - j\omega(2L_1 + \varepsilon\boldsymbol{M_{ff}})]i_{q_1} + \omega\phi_e\}\\ \bar{v}_{5_N}^{1+} &= \frac{1}{6}j\varepsilon e^{-j2\vartheta_f}\{[R_s + j\omega(L_1 + L_5 + \varepsilon\boldsymbol{M_{ff}})]i_{q_1} + \omega\phi_e\}\\ \bar{v}_{5_N}^{1-} &= -\frac{1}{6}j\varepsilon\{[R_s - j\omega(L_1 + L_5 + \varepsilon\boldsymbol{M_F})]i_{q_1} + \omega\phi_e\}\end{aligned} \tag{3.24}$$

where subscript N means that the voltage harmonics are due to a variation in the number of turns. The back electromotive force dominates in (3.24) while operating at high speeds and low currents. Therefore, under these specific operating conditions, (3.24) can be simplified by considering solely the back electromotive force term.

Equations (3.24) can be inverted to determine in which phase the MD occurs and the corresponding variation in the number of turns:

$$\vartheta_f = -\frac{1}{2}Arg\left(\bar{v}_{5_N}^{1+}\bar{v}_{5_N}^{1-}\right) + k\pi \qquad (k \in \mathbb{R}) \tag{3.25}$$

$$\Delta N_t \simeq \Re_e \left[\frac{6j\bar{v}_{1_N}^{1-} e^{-2j\theta_f}}{R_s i_{q_1} - 2j\omega L_1 i_{q_1} + \omega\phi_{e_f}} N_t \right]. \tag{3.26}$$

Equations (3.25)-(3.26) can be used to identify a MD during the operation of the drive. This can be done by estimating the harmonic components $\bar{v}_{1_N}^{1-}$, $\bar{v}_{5_N}^{1-}$ and $\bar{v}_{5_N}^{1+}$ by means of a suitable control system similar to that shown in Sec. 3.1.3.

3.1.3 Short Circuit Equations

A SC is one of the most dangerous faults that may affect the windings of an electric motor, since it causes changes in resistance, an imbalance in inductance, and variations in flux linkage. Furthermore, unlike MDs or HRCs, a SC generates the flow of an uncontrolled current that may exceed the rated value by ten times or more [16], depending on variables such as the quantity of shorted turns, rotational velocity, and motor characteristics.

A common method for diagnosing SC is the measurement of phase impedance. However, due to the unpredictable resistance along the path of the SC current, performing an offline measurement of the phase impedance may result in misclassifying a SC as an HRC or a MD, hence neglecting the possible harm that the SC current could cause.

This section discusses the development of an analytical model that can be effortlessly included into the control system for identifying and evaluate the presence of a SC through the analysis of voltage harmonics components as done in Secs. 3.1.1 and 3.1.2.

In this Section, a simple model of an Intern-Turn Short Circuit (ITSC) fault is derived. When an inter-turn short circuit occurs in phase f, the short-circuit current flows through a low-impedance path, assumed to be purely resistive, as shown in Fig. 3.2. Without loss of generality, the turns affected by the fault are assumed to be concentrated at the terminal end of phase f. The following aspects can be noted:

- The healthy phase z is characterized by the resistance R_z, self- and mutual inductances L_{zh} $(z, h \neq f)$, and current i_z.
- The faulty portion of phase f, represented by the red section in Fig. 3.2, is characterized by the resistance $R_f^{''}$, self-inductance $L_{ff}^{''}$, and current $i_f^{''}$.
- The healthy portion of phase f, represented by the sky blue section in Fig. 3.2, is characterized by the resistance $R_f^{'}$, self-inductance $L_{ff}^{'}$, and current $i_f^{'}$.
- The short-circuited branch, indicated in orange in Fig. 3.2, has a resistance R_{sc} through which the current i_{sc} flows.

In addition, L''_{zf} indicates the mutual inductance between the healthy phase z and the faulty portion of the faulty phase f, whereas L'_{zf} denotes the mutual inductance between an healthy phase and the healthy portion of the faulty phase. Finally, M_{ff} defines the mutual inductance between the healthy and faulty portions of the faulty phase.

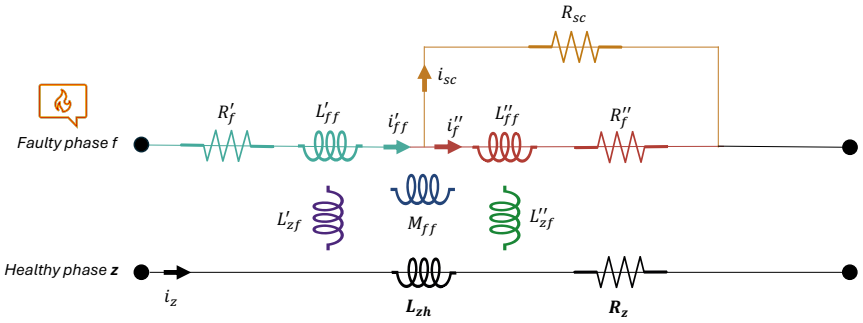

FIGURE 3.2: Equivalent circuit of the stator phase afflicted by a short circuited fault.

First, the inductances must be determined in both healthy and defective operating conditions in order to evaluate the impact of an ITSC fault on the DTP machine. The variables that belong to the healthy machine are highlighted in bold.

The inductance L'_{zf} can be estimated by using the superposition principle. Its deviation from $\boldsymbol{L_{zf}}$ is assumed to be caused by two contributions. The first one is the variation of the flux linkage due to a small reduction ΔN_f in the number of turns, the second one is due to a small displacement $\Delta\theta_f$ of the magnetic axis.

$$L'_{zf} = \boldsymbol{L_{zf}} + \frac{\partial \boldsymbol{L_{zf}}}{\partial N_f}\Delta N_f + \frac{\partial \boldsymbol{L_{zf}}}{\partial \theta_f}\Delta\theta_f \tag{3.27}$$

where N_f is the number of turns of the faulty phase. It can be demonstrated that $\boldsymbol{L_{zf}}$ can be approximated as follows:

$$\boldsymbol{L_{zf}} = \frac{1}{3}N_t N_f\left[L_{u1}\cos\left(\theta_z - \theta_f\right) + L_{u5}\cos\left(5\theta_z - 5\theta_f\right)\right] \tag{3.28}$$

where N_t indicates the number of turns of an healthy phase, θ_z is the electrical angle of the magnetic axis of the z-th healthy phase, L_{u1} and L_{u5} are the inductances in subspaces $\alpha_1 - \beta_1$ and $\alpha_5 - \beta_5$, respectively, when just one turn is considered.

If λ is the ratio of ΔN_f to the number of turns N_t of an healthy phase, considering (3.28), (3.27) becomes:

$$L'_{zf} = \boldsymbol{L_{zf}}\left[1 - \lambda + \boldsymbol{\Gamma_{zf}}\Delta\theta_f\right] \tag{3.29}$$

where:

$$\boldsymbol{\Gamma_{zf}} = \frac{L_{u1}\sin(\theta_z - \theta_f) + L_{u5}\sin(5\theta_z - 5\theta_f)}{L_{u1}\cos(\theta_z - \theta_f) + L_{u5}\cos(5\theta_z - 5\theta_f)}. \tag{3.30}$$

Since $\boldsymbol{L_{zf}} = L_{zf}^{'} + L_{zf}^{''}$, the following result can be obtained:

$$L_{zf}^{''} = \boldsymbol{L_{zf}}[\lambda - \boldsymbol{\Gamma_{zf}}\Delta\theta_f]. \tag{3.31}$$

After some tedious algebraic calculations, the self-inductances $L_{ff}^{'}$ and $L_{ff}^{''}$ of the faulty phase and the mutual-inductance M_{ff}, can be obtained. So, the machine inductances are summarized as follows:

$$\begin{aligned}
L_{zf}^{'} &= L_{fz}^{'} = \boldsymbol{L_{zf}}[1 - \lambda + \boldsymbol{\Gamma_{zf}}\Delta\theta_f] \\
L_{zf}^{''} &= L_{fz}^{''} = \boldsymbol{L_{zf}}[\lambda - \boldsymbol{\Gamma_{zf}}\Delta\theta_f] \\
L_{ff}^{'} &= \boldsymbol{L_{zf}}(1-\lambda)^2 \\
L_{ff}^{''} &= \boldsymbol{L_{zf}}\lambda^2 \\
M_{ff}^{''} &= \boldsymbol{L_{zf}}\lambda(1-\lambda).
\end{aligned} \tag{3.32}$$

It worthwhile to note that (3.32) applies for machines that have only one pole pairs. In fact, under SC circuit operating conditions, Babak V. et al [17] have shown that the inductances increase by a small percentage proportional to number of pole pairs. Therefore, as the machine considered in this study has only two pole pairs, the variation of the inductances compared to those estimated in (3.32) has been neglected.

Based on the equivalent circuit shown in Fig. 3.2, one can derive the expressions of the contributions to the stator fluxes due to the sole stator currents (the contribution of the excitation field is considered later):

$$\begin{aligned}
\varphi_z &= \sum_{\substack{h=1 \\ h\neq f}}^{N} \boldsymbol{L_{zh}} i_h + L_{zf}^{'} i_f^{'} + L_{zf}^{''} i_f^{''} \qquad (z \neq f) \\
\varphi_f^{'} &= \sum_{\substack{h=1 \\ h\neq f}}^{N} \boldsymbol{L_{hf}^{'}} i_h + L_{ff}^{'} i_f^{'} + M_{ff} i_f^{''} \\
\varphi_f^{''} &= \sum_{\substack{h=1 \\ h\neq f}}^{N} \boldsymbol{L_{hf}^{''}} i_h + M_{ff} i_f^{'} + L_{ff}^{''} i_f^{''}.
\end{aligned} \tag{3.33}$$

Substituting (3.32) in (3.33) yields:

$$\begin{aligned}
\varphi_z &= \boldsymbol{\varphi_z} + \boldsymbol{L_{zf}}[\lambda - \boldsymbol{\Gamma_{zf}}\Delta\theta_f] i_{sc} \qquad (z \neq f) \\
\varphi_f^{'} &= (1-\lambda)(\boldsymbol{\varphi_f} - \boldsymbol{L_{zf}}\lambda i_{sc}) \\
\varphi_f^{''} &= \lambda(\boldsymbol{\varphi_f} + \lambda \boldsymbol{L_{zf}}\lambda i_{sc}).
\end{aligned} \tag{3.34}$$

The excitation field generates a flux linkage $\varphi_{e,z}$ with the healthy phases, which remain unaffected. and the faulty and healthy portion of faulty phase. Conversely, the flux linkage with

the faulty phase due to the rotor magnets can be split into two terms, $\varphi_{e,f}^{'}$ and $\varphi_{e,f}^{''}$, respectively for the healthy and faulty portion.

$$\begin{aligned} \varphi_{e,z} &= \boldsymbol{\varphi_{e,z}} \qquad (z \neq f) \\ \varphi_{e,f}^{'} &= (1-\lambda)\boldsymbol{\varphi_{e,f}} \\ \varphi_{e,f}^{''} &= \lambda \boldsymbol{\varphi_{e,f}}. \end{aligned} \tag{3.35}$$

The stator voltage equations can be written as follows:

$$\begin{aligned} v_z &= R_s i_z + \frac{d}{dt}\varphi_z + \frac{d}{dt}\varphi_{e,z} \qquad (z \neq f) \\ v_f^{'} &= R_f^{'} i_f + \frac{d}{dt}\varphi_f^{'} + \frac{d}{dt}\varphi_{e,f}^{'} \\ v_f^{''} &= (1+\lambda) R_f^{''} i_f + \frac{d}{dt}\varphi_f^{''} + \frac{d}{dt}\varphi_{e,f}^{''}. \end{aligned} \tag{3.36}$$

It is worth noting that the voltage drop on R_{sc} is never considered in the previous equations, so the entire model does not rely on the knowledge of this unknown parameter.

Substituting (3.34) and (3.35) in (3.36), gives:

- if $z \neq f$ (healthy phase):

$$\begin{aligned} v_z &= \boldsymbol{v_z} + \Delta v_z \\ \Delta v_z &= \boldsymbol{L_{zf}}[\lambda - \boldsymbol{\Gamma_{zf}} \Delta\theta_f] \frac{di_{sc}}{dt} \end{aligned} \tag{3.37}$$

- if $z = f$ (faulty phase):

$$\begin{aligned} v_f &= \boldsymbol{v_f} + \Delta v_f \\ \Delta v_f &= \lambda\Big(\boldsymbol{L_{ff}} \frac{di_{sc}}{dt} + R_s i_{sc}\Big) \end{aligned} \tag{3.38}$$

If the stator phases are star connected, the phase voltages can be fully represented by two space vectors, $\bar{v}_1$ and $\bar{v}_5$:

$$\begin{aligned} \bar{v}_1 &= \bar{\boldsymbol{v}}_{\mathbf{1}} + \Delta\bar{v}_1 \\ \bar{v}_5 &= \bar{\boldsymbol{v}}_{\mathbf{5}} + \Delta\bar{v}_5 \end{aligned} \tag{3.39}$$

where $\bar{\boldsymbol{v}}_{\mathbf{1}}$ and $\bar{\boldsymbol{v}}_{\mathbf{5}}$ are the voltage space vectors in healthy conditions, whereas $\Delta\bar{v}_1$ and $\Delta\bar{v}_5$ are the voltage variations resulting from the ITSC.

The expression of $\Delta\bar{v}_1$ and $\Delta\bar{v}_1$ can be found by applying the space vector transformations (2.11) and (2.12) to Δv_z $(z \neq f)$ and Δv_f given by (3.37) and (3.38):

$$\begin{aligned} \Delta\bar{v}_1 &= \frac{1}{3}\lambda R_{sc} i_{sc} e^{j\theta_f} + (\lambda\bar{\Lambda}_1 - \Delta\theta_f \bar{\zeta_1}) \frac{d}{dt} i_{sc} \\ \Delta\bar{v}_5 &= \frac{1}{3}\lambda R_{sc} i_{sc} e^{j5\theta_f} + (\lambda\bar{\Lambda}_5 - \Delta\theta_f \bar{\zeta_5}) \frac{d}{dt} i_{sc} \end{aligned} \tag{3.40}$$

where $\bar{\Lambda}_1$ and $\bar{\Lambda}_5$ are two complex quantities defined as follows:

$$\begin{aligned}\bar{\Lambda}_1 =&\frac{1}{9}\sum_{k=1}^{3}\bar{\beta}^{4(k-1)}\Big\{L_1\Big[\cos(\theta_{A_k}-\theta_f)+\bar{\beta}\cos(\theta_{B_k}-\theta_f)\Big]+\\&+L_5\Big[\cos(5\theta_{A_k}-5\theta_f)+\bar{\beta}\cos(5\theta_{B_k}-5\theta_f)\Big]\Big\}\end{aligned} \tag{3.41}$$

$$\begin{aligned}\bar{\Lambda}_5 =&\frac{1}{9}\sum_{k=1}^{3}\bar{\beta}^{8(k-1)}\Big\{L_1\Big[\cos(\theta_{A_k}-\theta_f)+\bar{\beta}^5\cos(\theta_{B_k}-\theta_f)\Big]+\\&+L_5\Big[\cos(5\theta_{A_k}-5\theta_f)+\bar{\beta}^5\cos(5\theta_{B_k}-5\theta_f)\Big]\Big\}\end{aligned} \tag{3.42}$$

and the quantities $\bar{\zeta}_1$ and $\bar{\zeta}_5$ are equal to $\bar{\Lambda}_1$ and $\bar{\Lambda}_5$, respectively, but the cosine is replaced by the sine. The parameters L_1 and L_5 are the machine inductances in subspaces $\alpha_1-\beta_1$ and $\alpha_5-\beta_5$, respectively, and can be calculated by using a finite-element model of the machine [18].

After some calculations, it is possible to verify that (3.41) and (3.42) can be rewritten in a simpler form:

$$\begin{aligned}\bar{\Lambda}_1 &= \frac{1}{3}L_1e^{j\theta_f}\\ \bar{\Lambda}_5 &= \frac{1}{3}L_5e^{j5\theta_f}.\end{aligned} \tag{3.43}$$

Similarly, $\bar{\zeta}_1$ and $\bar{\zeta}_5$ become as follows:

$$\begin{aligned}\bar{\zeta}_1 &= \frac{1}{3}jL_1e^{j\theta_f}\\ \bar{\zeta}_5 &= \frac{1}{3}jL_5e^{j5\theta_f}.\end{aligned} \tag{3.44}$$

Substituting (3.43) and (3.44) in (3.40) gives:

$$\begin{aligned}\Delta\bar{v}_1 &= \frac{1}{3}e^{j\theta_f}\Big[\lambda R_s i_{sc}+L_1(\lambda-j\Delta\theta_f)\frac{d}{dt}i_{sc}\Big]\\ \Delta\bar{v}_5 &= \frac{1}{3}e^{j5\theta_f}\Big[\lambda R_s i_{sc}+L_5(\lambda-j\Delta\theta_f)\frac{d}{dt}i_{sc}\Big].\end{aligned} \tag{3.45}$$

For the sake of simplicity, the short circuit current is assumed sinusoidal with angular frequency ω_1:

$$i_{sc}=\Re_e\Big\{\bar{I}_{sc}e^{j\omega_1 t}\Big\}=\frac{\bar{I}_{sc}e^{j\omega_1 t}+\bar{I}^*_{sc}e^{-j\omega_1 t}}{2}. \tag{3.46}$$

Substituting (3.46) in (3.45), the harmonic balance allows one to calculate the positive and negative sequence harmonic components $\bar{v}_1^{1-}$, $\bar{v}_5^{1-}$ and $\bar{v}_5^{1+}$:

$$\begin{aligned}\bar{v}_1^{1-} &= -\frac{1}{6}\lambda\bar{I}^*_{sc}e^{j\vartheta_f}\{R_s-j\omega_eL_1(1-j\frac{\Delta\theta_f}{\lambda})\}\\ \bar{v}_5^{1-} &= -\frac{1}{6}\lambda\bar{I}^*_{sc}e^{j5\vartheta_f}\{R_s-j\omega_eL_5(1-j\frac{\Delta\theta_f}{\lambda})\}\\ \bar{v}_5^{1+} &= \frac{1}{6}\lambda\bar{I}_{sc}e^{j5\vartheta_f}\{R_s+j\omega_eL_5(1-j\frac{\Delta\theta_f}{\lambda})\}.\end{aligned} \tag{3.47}$$

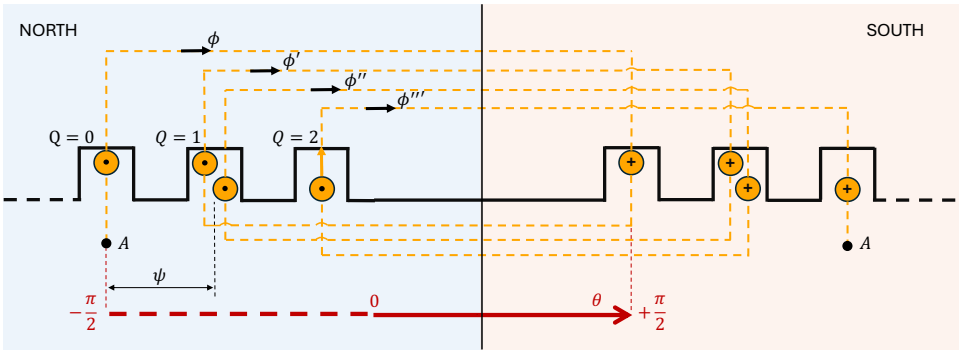

FIGURE 3.3: Arrangement of stator windings considering a pole pair.

The second and the third equations of (3.47) can be inverted to determine the angle θ_f of the magnetic axis of the faulty phase and the quantity λI_{sc}, which is related to the fault severity:

$$\vartheta_f = -\frac{1}{2}\left[Arg(\bar{v}_5^{1+}\bar{v}_5^{1-}) + \frac{\Delta\theta_f}{\lambda}\frac{(L_5\omega_e)^2}{R_s^2+(L_5\omega_e)^2}\right] + k\pi \quad (k \in \mathbb{R}) \tag{3.48}$$

$$\lambda I_{sc} = 6\sqrt{\left|\frac{\bar{v}_5^{1-}(\bar{v}_5^{1+})^*}{(R_s+j\omega_e L_5)^2}\right|}. \tag{3.49}$$

The value of $\Delta\theta_f$ in (3.47) and (3.48) corresponds to the rotation of the magnetic axis of the faulty phase and depends on the specific coil affected by the ITSC. Let us describe the steps for obtaining its value for the dual-three-phase motor used the experimental tests whose main parameters are listed in Tab. 4.4.

The magnetic flux density produced by the stator winding only under a pole pair, in a dual-three-phase machine, can be written as the sum of the fundamental spatial component and the fifth-order spatial harmonic component:

$$B(\theta) = \Re_e\left\{\bar{B}_1 e^{j\theta} + \bar{B}_5 e^{j5\theta}\right\} \tag{3.50}$$

where $\bar{B}_1$ and $\bar{B}_5$ are two phasors representing the air-gap magnitude and phase of the flux density in the subspaces α_1-β_1 and α_5-β_5, respectively.

Let us consider only a pole pair of a of a generic stator phase. With reference to the coordinate system shown in Fig 3.3, the flux linkage with the first coil is as follows:

$$\Phi = \frac{1}{\pi}NS\int_{-\frac{\pi}{2}}^{+\frac{\pi}{2}} B d\theta \tag{3.51}$$

where N is the number of coil turns and S is the section of a turn.

Substituting (3.50) in (3.51) leads to the following explicit expression for Φ:

$$\Phi = \frac{2}{\pi}NS\Re_e\left\{\bar{B}_1 + \frac{\bar{B}_5}{5}\right\}. \tag{3.52}$$

Using the same approach, considering the electrical slot pitch Ψ between two slots, the flux linked with the second coil is as follows:

$$\Phi^{'} = \frac{2}{\pi} NS\Re_e\Big\{\bar{B}_1 e^{j\Psi} + \frac{\bar{B}_5}{5} e^{j5\Psi}\Big\}. \tag{3.53}$$

As can be seen in Fig. 3.3, the flux linkage $\Phi^{''}$ of the third coil, placed in the lowest layer, is equal to $\Phi^{'}$. Finally, the flux linkage $\Phi^{'''}$ of the fourth coil is as follows:

$$\Phi^{'''} = \frac{2}{\pi} NS\Re_e\Big\{\bar{B}_1 e^{j2\Psi} + \frac{\bar{B}_5}{5} e^{j10\Psi}\Big\}. \tag{3.54}$$

The total flux linkage with a stator phase under a pole pairs is the sum of the four contributions:

$$\Phi_T = \frac{2}{\pi} NS\Re_e\Big\{\bar{B}_1(1 + 2e^{j\psi} + e^{j2\psi}) + \bar{B}_5(1 + 2e^{j5\psi} + e^{j\psi})\Big\}. \tag{3.55}$$

The following identity holds:

$$(1 + 2e^{j\psi} + e^{j2\psi}) = (1 + e^{j\psi})^2 = 4e^{j\psi} cos^2\Big(\frac{\psi}{2}\Big). \tag{3.56}$$

Substituting (3.56) in (3.55) yields:

$$\Phi_T = \frac{2}{\pi} 4NS\Re_e\Big\{\bar{B}_1 e^{j\psi} cos^2\Big(\frac{\psi}{2}\Big) + \bar{B}_5 e^{j5\psi} cos^2\Big(\frac{5}{2}\psi\Big)\Big\}. \tag{3.57}$$

Expression (3.57) defines the flux linked with a stator phase considering just one pole pair and healthy operating conditions. Given a machine with p pole pairs, and assuming an ITSC affecting a certain number of turns ΔN in a generic coil whose first active side in slot Q ($Q = 0, 1, 2$), the total flux linkage (3.57) becomes as follows:

$$\Phi_{T,sc} = p\Phi_T - \Delta\Phi = \frac{2}{\pi} N_t S\Re_e\Big\{\bar{B}_1\Big[cos^2\Big(\frac{\psi}{2}\Big)e^{j\psi} - \lambda e^{jQ\psi}\Big] + \frac{\bar{B}_5}{5}\Big[cos^2\Big(\frac{5\psi}{2}\Big)e^{j5\psi} - \lambda e^{j5Q\psi}\Big]\Big\} \tag{3.58}$$

where N_t, the total number of turns of a stator phase, is equal to $4pN$ in this specific case.

When the machine operates in sinusoidal conditions, the magnetic field B_5 is zero. In general, in a dual-three-phase machine, the amplitude of the spatial harmonics of he air-gap flux density is inversely proportional to harmonic order. This suggests that the contribution of B_5 can be neglected in comparison to that of B_1, and (3.58) can rewritten as follows:

$$\Phi_{T,sc} = \frac{2}{\pi} N_t S\Re_e\left\{\bar{B}_1 cos^2\Big(\frac{\psi}{2}\Big)e^{j\psi}\left[1 - \frac{\lambda e^{j(Q-1)\psi}}{cos^2(\frac{\psi}{2})}\right]\right\}. \tag{3.59}$$

The quantity $\left[1-\frac{\lambda e^{j(Q-1)\psi}}{cos^2(\frac{\psi}{2})}\right]$ in (3.59) is a complex number whose phase angle is the angular variation $\Delta\theta_f$ given in (3.60) for the magnetic axis of the faulty phase in case of an ITSC. It is as follows:

$$\Delta\theta_f \approx -\arctan\left(\frac{\lambda sin([Q-1]\Psi)}{cos^2(\frac{\psi}{2})-\lambda cos([Q-1]\Psi)}\right) \approx -\frac{\lambda sin([Q-1]\Psi)}{cos^2(\frac{\psi}{2})} \tag{3.60}$$

where Ψ is the electrical slot pitch, and Q is a parameter that identifies the slot of the faulty coil under a pole pair. For the DTP machine under consideration, Ψ is 15°, and Q can take the values 0, 1, and 2. Since each stator phase has two layers and is composed of four coils, which span over three slots per pole, if $Q = 0$, the fault affects a coil whose first active side is in the first slot; if $Q = 1$, the fault affects a coil whose first active side in the second slot; and if $Q = 2$, the fault affects a coil whose first active side is in the third slot. The approximated expression in (3.60) holds if both λ and ψ are small enough.

3.1.4 Finite Element Analysis

A numerical model of the dual-three-phase brushless motor (parameters in Tab. 4.4) based on finite element analysis has been developed to simulate the machine behavior and validate the results predicted by the analytical models presented in Secs. 3.1.1, 3.1.2 and 3.1.3.

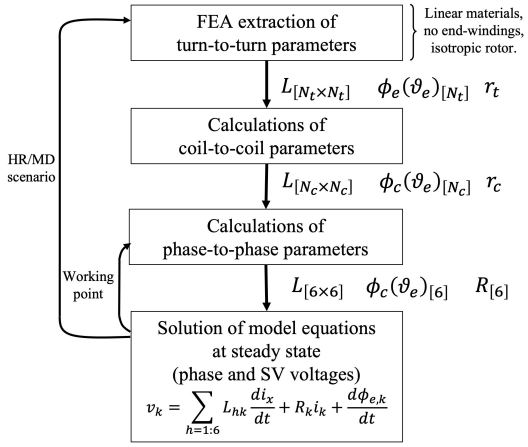

FIGURE 3.4: Block diagram of the workflow for the calculation of the parameters of a healthy and faulty machine.

The actions performed by the numerical model are illustrated in Fig. 3.4 and summarized in the following steps:

- Finite element analysis -based calculation of the $[N_t \times N_t]$ turn-to-turn inductance matrix, the N_t values of the flux linkage with each turn $\phi_e(\vartheta_{el})$ due to the rotor magnets for each electrical position θ_{el} of the rotor, and the turn resistance r_t (see Fig. 3.5).

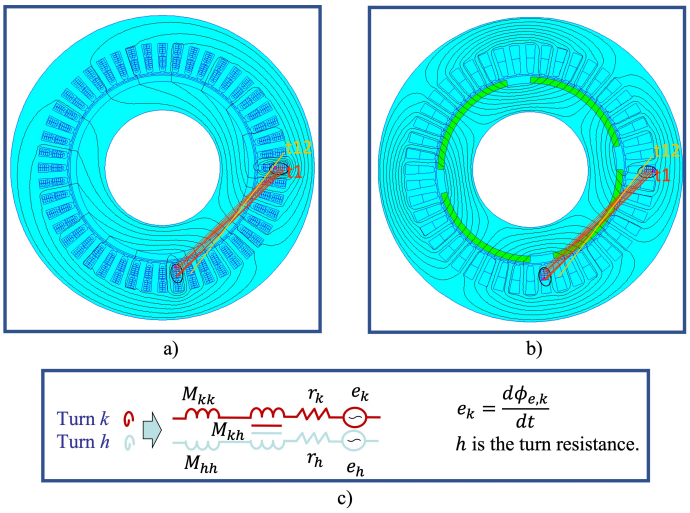

FIGURE 3.5: Flux density distribution by FEA used to extract the turn-to-turn motor parameters and equivalent electric circuit. a) A single turn is fed to calculate the turn-to-turn inductance matrix $M_{[N_t \times N_t]}$. b) Permanent magnet field is considered to calculate the flux linkage with the turns $\phi_{e[N_t]}$. c) Equivalent circuit for two generic turns k and h.

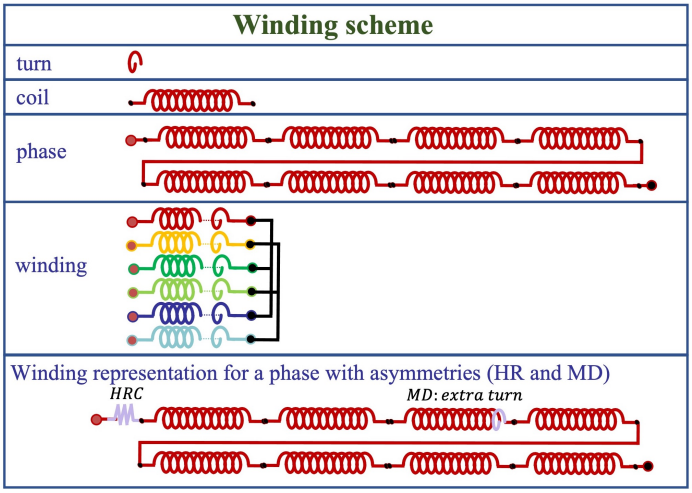

FIGURE 3.6: Connection scheme of a phase, including high-resistance connection and an extra turn in the 3rd coil.

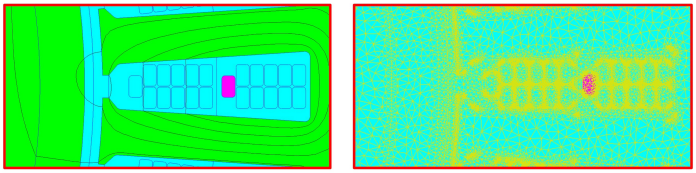

FIGURE 3.7: Zoomed view of a slot. The additional turn due to mismanufacturing is in red. a) Simulated geometry. b) Mesh grid during the calculation of the turn-to-turn inductance matrix.

- Evaluation of the coil parameters, such as the $[N_c \times N_c]$ coil-to-coil inductance matrix, the N_c values of the flux linkage with each coil, and the coil resistance r_c.
- Evaluation of the phase parameters, such as the $[6 \times 6]$ phase-to-phase inductance matrix, the flux linkage with each phase $\phi_{Z_k}(\vartheta_{el})$, and the phase resistances R_{Z_k} (with $Z = A, B$ and $k = 1, 2, 3$).

The flux linkage of a coil due to the rotor magnets and the coil resistance are obtained by summing the contributions of the single turns. Similarly, the coil-to-coil inductances are calculated by summing all the elements of the turn-to-turn inductance matrix corresponding to the considered pair of coils. The same approach is used to determine the phase-to-phase parameters of the model, starting from the coil-to-coil ones. In the case of a defective coil, the missing (extra) turns are not considered (included) in the sums.

The dual-three-phase motor used for the numerical simulations features 480 turns arranged in a double-layer layout. In normal conditions, each coil comprises ten turns located respectively in the top and bottom layers of two slots 165 electrical degrees apart. The windings are composed of 48 coils. Finally, the coils are series connected in 6 groups of 8 coils each to form the six phases of the machine.

Fig. 3.5 shows the position of the turns of the first coil (in red) and the first turn of the second coil (in orange).

Fig. 3.6 depicts the connection scheme of a generic phase. Also, it includes the equivalent schematic of an unbalanced phase, with an HRC at the input terminal and an ET due to a manufacturing defect at the end of the third coil.

In conclusion, 528 turns (480 + 48) are simulated in the Finite-Element Model (FEM) to consider the possibility of an extra turn in each coil. A detailed view of the geometry simulated to calculate the turn-to-turn inductance matrix and the mesh used during the same FEA simulation are shown in Fig. 3.7.

The turn-to-turn inductance matrix is obtained by supplying with 1 A the different turns of a single coil, one by one, and extracting the flux linkage with all the 528 turns. Due to the symmetry properties of the stator, these results are sufficient to calculate all elements of the

inductance matrix without further simulations. The flux linkages through the turns due to the permanent magnets are calculated for each rotor position. For symmetry reasons, it is sufficient to evaluate the flux linkage as a function of the rotor position only for the turns of a single coil (as in Fig. 3.5). The values for the remaining coils are obtained by shifting the resulting function by the angle $\theta_{slot,el}$ between neighboring slots.

The proposed approach can generate a dataset with the outputs of about one million asymmetries, faults, and operating scenarios in about 1.5 hours of numerical simulation in Matlab software with an AMD Ryzen 9 5900X Desktop Processor (12 CPU Cores, 3.7 GHz base clock frequency, 64 Gb RAM, NVIDIA QUADRO PNY P2000 Graphic Card). The methods can be easily adapted to motors with a different number of phases and other winding layouts.

3.2 Simulation and Experimental Results

Fig. 3.8 compares the magnitude of the harmonic component $\bar{v}_{1_R}^{1-}$ predicted by (3.8) with that estimated by the FEM as a function of the motor current i_{q_1} when the resistance of phase A_3 is 30% higher than the rated value. As can be seen, the matching between the expected and estimated values is excellent.

Fig. 3.9 shows the magnitude and phase of the complex vectors $\bar{R}_1$ and $\bar{R}_5$ when R_{A3} is 1.3 times the rated resistance and confirms that R_{A0} and R_{B0} are real numbers, as predicted by (3.9).

Fig. 3.10 compares the magnitude of the voltage harmonic $\bar{v}_{1_N}^{1-}$ resulting from (3.24) with that obtained with the FEM model as a function of the rotor speed for different values of i_{q_1} when an extra turn is added to phase A_3. In this case too, the numerical simulations perfectly match the results of the theoretical analysis.

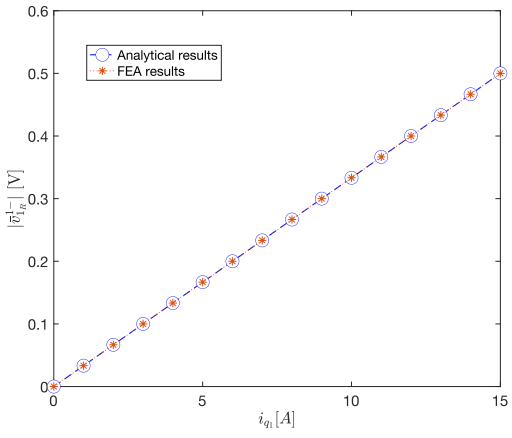

FIGURE 3.8: Magnitude of $\bar{v}_{1_R}^{1-}$ estimated by FEA-based simulations and analytical calculations as a function of i_{q_1} when the resistance R_{A_3} is 1.3 times the rated stator resistance.

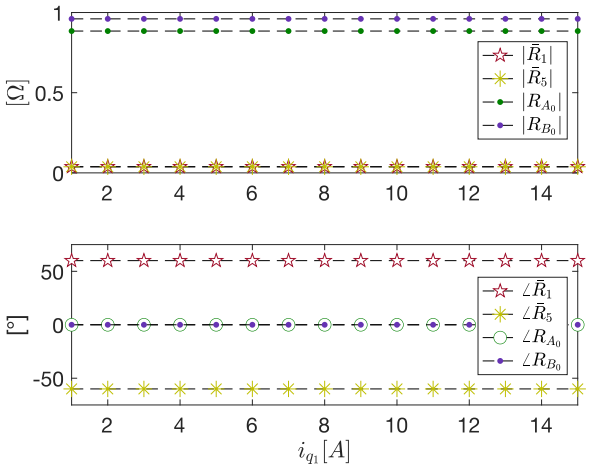

FIGURE 3.9: Magnitude and phase of the space vectors representing the HRC as a function of i_{q_1} when the resistance R_{A_3} is 1.3 times the rated stator resistance.

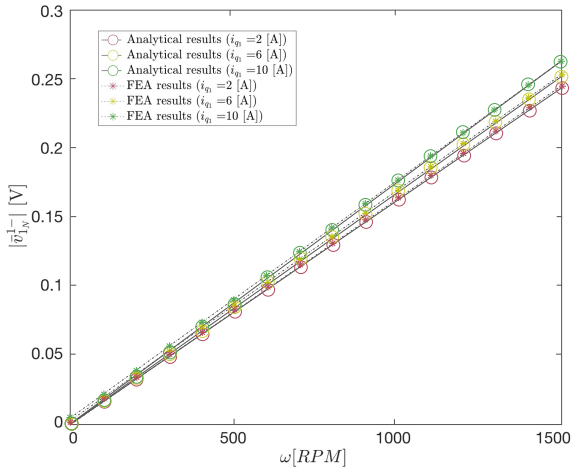

FIGURE 3.10: Magnitude of $\bar{v}^{1-}_{1_N}$ estimated by FEA-based simulations and through analytical calculations for different speeds and current values when an extra turn is added to phase A_3.

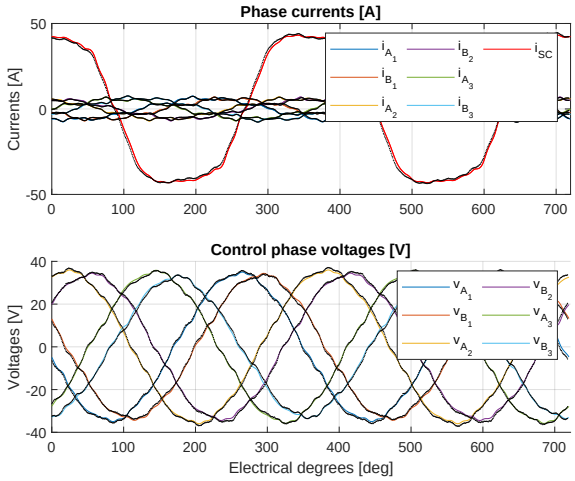

FIGURE 3.11: Comparison of analytical and experimental results. The red current is the short circuit one. The test is with a short circuit of 10 turns and 400 $m\Omega$ phase resistance unbalance, while the phase current reference is set at 5 A and the motor is rotating at 500 rpm. The experimental waveform are in black.

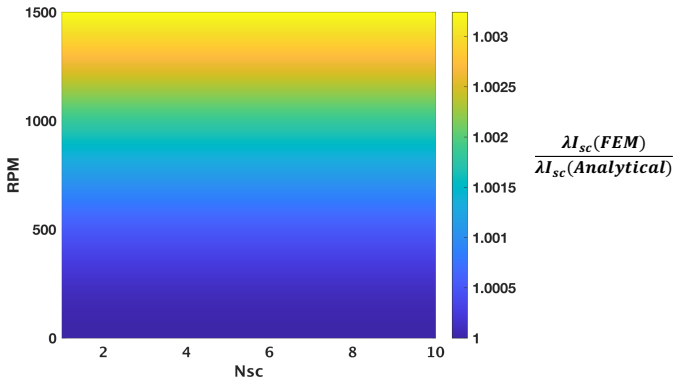

FIGURE 3.12: Ratio between λI_{sc} obtained from the FEM and that one predicted analytically.

Fig. 3.11 compares the analytical and experimental waveforms of the phase currents and voltages acquired experimentally with those predicted by the FEM under SC operating conditions. The waveforms are almost identical, demonstrating the effectiveness of the FEM to replicate the machine behavior, even under faulty operating conditions.

Once the validity of the FEM has been verified experimentally in case of a SC, it was employed to evaluate the results provided by the analytical model in Sec. 3.1.3 . Fig. 3.12 depicts the ratio of λI_{sc} derived from the FEM to that calculated from (3.49). The ratio consistently approximates one, irrespective of speed and the number of shorted turns considered, hence validating the analytical model.

Experiments were performed to evaluate the analytical model described in Sec. 3.1.3. All experiments incorporate (3.48) and (3.49) into the control system depicted in Fig. 3.13 for ITSC fault diagnosis. The control system runs on a dSPACE platform (MicroLabBox, DS1104), which controls the operation of the six-phase power converter via fiber-optic cables. A power supply unit from Elektro-Automatik (EA-PS 9500 - 20) is used to provide the DC link voltage for the

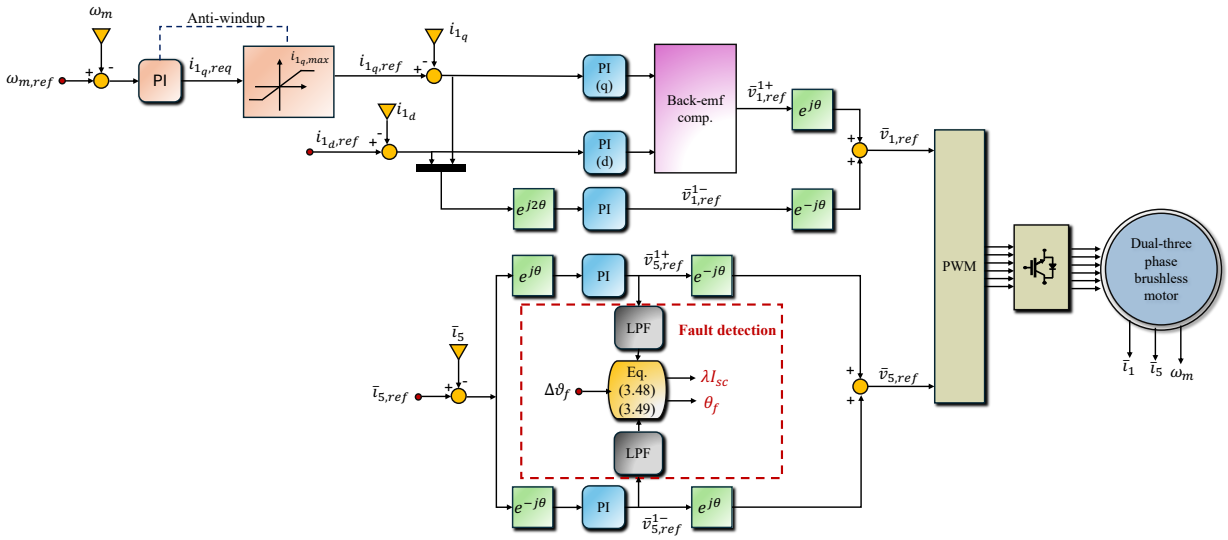

FIGURE 3.13: Block diagram of the control system used for the ITSC fault detection.

drive system. Additionally, a DC generator is used as a mechanical load. Fig. 3.14 shows the overall setup.

The dual-three-phase machine prototype allows one to shorten 5 or 10 turns in phases A_3 or B_3. The rotating speed cannot be higher than 500 RPM during the experimental tests. This speed value prevents the short circuit current from reaching levels that might demagnetize the motor or permanently harm the drive. However, if the speed were higher, fault detection is expected to be easier.

Fig. 3.15 illustrates the scenario in which a 10-turn ITSC occurs in phase B_3. The fault indicator λI_{sc} resulting from (3.49) experiences an abrupt increase from zero to 6 A after the introduction of the ITSC. Moreover, the angle θ_f, as predicted by (3.48), reaches 90°, coinciding with the magnetic axis of phase B_3. To further validate the effectiveness of the analytical model, an ITSC has been placed in A_3, and the results are depicted in Fig. 3.16. The fault indicator λI_{sc} remains equal to 6 A, indicating that the fault's intensity does not change compared to that for the ITSC in B_3, while the angle θ_f is 60°, corresponding to the magnetic axis of phase A_3. During these tests, the parameter λ is 10/80, and the measured short circuit current is about 37 A, which leads to a theoretical value of λI_{sc} of 4.625 A, slightly lower than the actual value. The discrepancy is likely attributable to the ambiguity regarding the machine parameters, particularly the inductance L_5.

Afterwards, five shorted turns have been introduced in A_3. The findings depicted in Fig. 3.17 support the reliability of the analytical model in identifying the fault, even at reduced numbers of shorted turns.

Finally, the proposed approach has been evaluated under transient conditions when the speed raises from 200 to 500 RPM. Below 500 RPM, the measurement of the short circuit current is

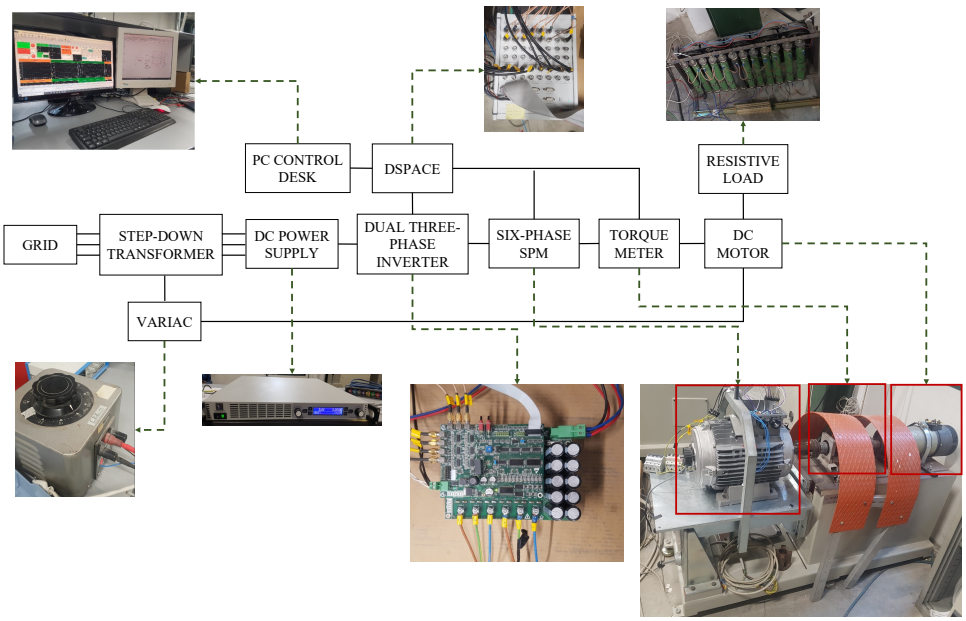

FIGURE 3.14: Test bench.

comparable to the rated current of the machine and does not lead to perceivable effects. Figure 3.18 illustrates that raising the speed results in an increase of λI_{sc}, while the angle θ_f remains constant at 60° proving that the analytical model is reliable in transient conditions when the effects of the ITSC are not negligible.

To enhance the reliability of the fault detection technique, an additional resistance R_{sc} has been included in the short circuit branch. In practical applications, this resistance cannot be easily estimated and its value is unknown; therefore, a robust fault diagnosis strategy should be valid regardless its value. In the proposed case of study, a resistance value of about 15% of the stator resistance is considered to achieve a speed of 700 RPM while maintaining the short circuit current at 37 A, which is the level attained at 500 RPM without any additional resistance. Fig. 3.19 presents the measurements obtained with the motor rotating at 700 RPM, whereas Fig. 3.20 depicts the transient scenario. As can be seen, the proposed strategy remains valid even in the presence of an additional resistance within the short circuit branch. Further, comparing Fig. 3.15 and Fig. 3.16 with Fig. 3.19, it is worth noting that the parameter λI_{sc}, estimated by means of (3.49), remains constant to 6 A regardless the short circuit resistance. This result demonstrates that the proposed technique is independent of the short circuit resistance.

3.3 Conclusions

This chapter introduced three analytical models that can be used to calculate the voltage harmonic contributions resulting from three specific faults (HRCs, MDs, SCs) that may occur in the stator windings of a brushless dual-three-phase motor.

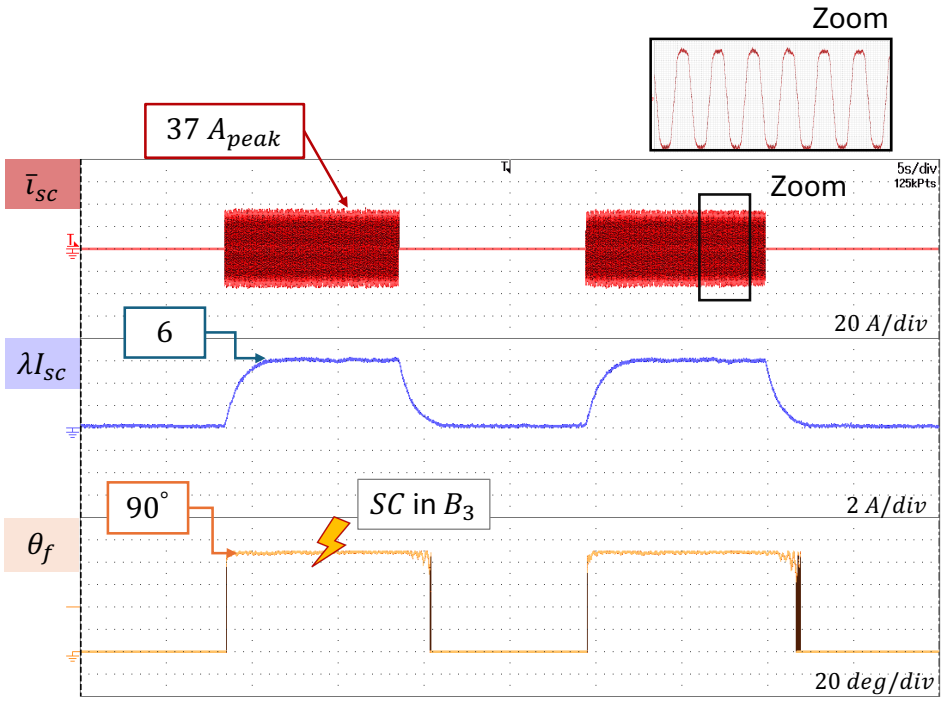

FIGURE 3.15: Fault estimation and identification in case of 10 shorted turns in the phase B_3 with the motor rotating ad 500 RPM and 5 A current reference.

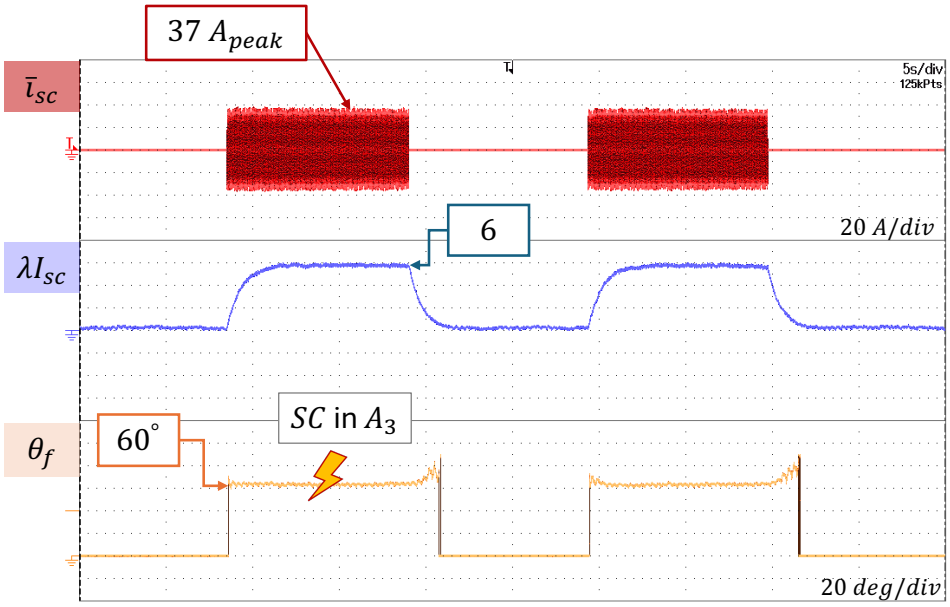

FIGURE 3.16: Fault estimation and identification in case of 10 shorted turns in the phase A_3 with the motor rotating ad 500 RPM and 5 A current reference.

The case study of HRC demonstrated how the voltage harmonic contributions can be used to determine the deviation of each phase resistance from the average value of the phase resistances and identify the phase in which the resistance imbalance occurs.

Regarding the presence of a variation in the number of turns in a stator phase, it was shown how it is possible to identify both the magnetic axis of the phase in which said variation takes place and to quantify the variations.

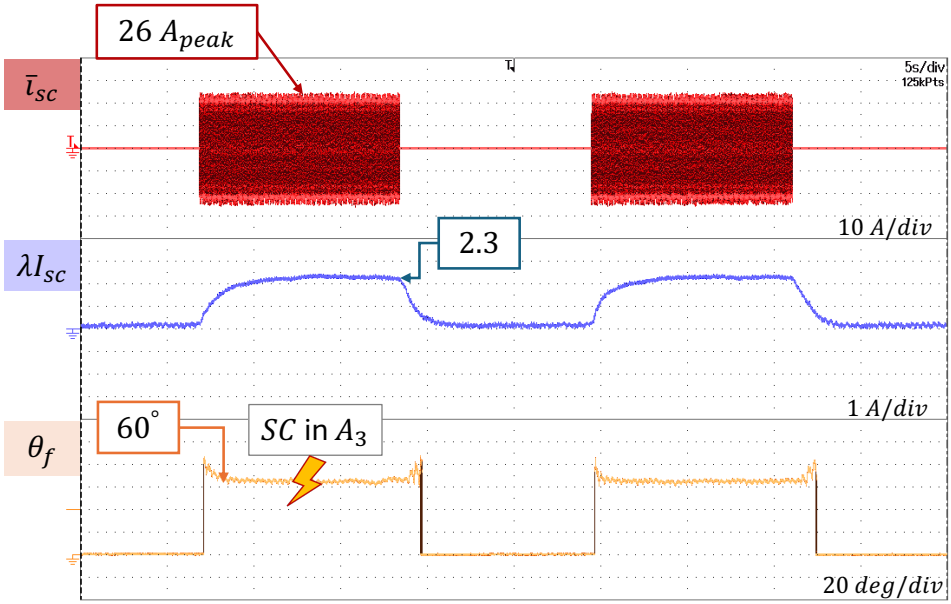

FIGURE 3.17: Fault estimation and identification in case of 5 shorted turns in the phase A_3 with the motor rotating ad 500 RPM and 5 A current reference.

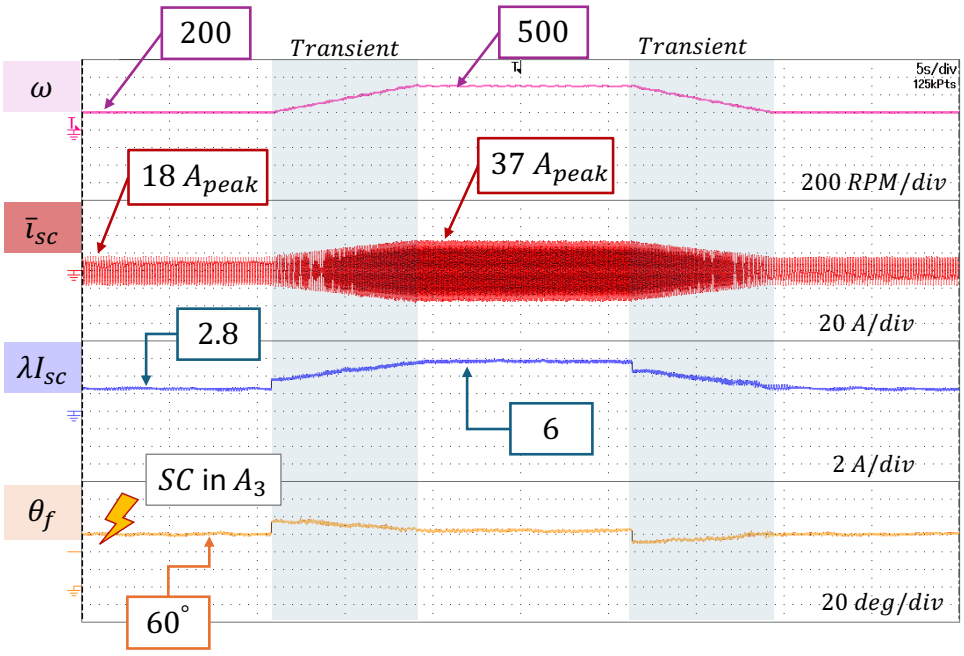

FIGURE 3.18: Fault estimation and identification in case of 10 shorted turns in the phase A_3 with the motor speed varying from 200 to 500 RPM and 5 A current reference.

Finally, the SC analytical model provides the estimation of fault severity and the identification of magnetic axis of the phase in which the SC occurs.

The presented analytical models can be included in the control system and, with the use of opportunely tuned PI current controllers, enable the estimation and identification of faults without the need to power-off the motor and utilize costly measuring devices.

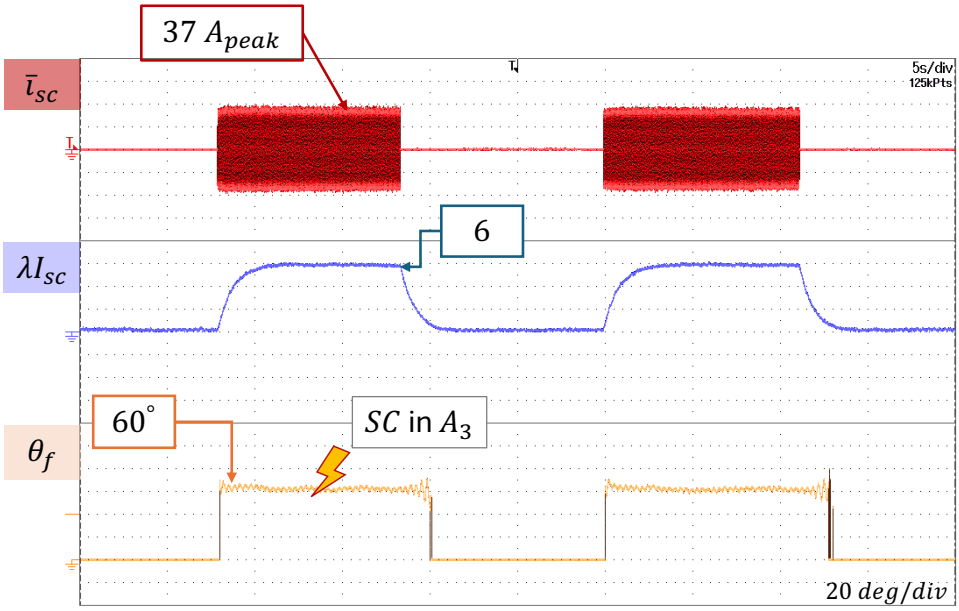

FIGURE 3.19: Fault estimation and identification in case of 5 shorted turns in the phase A_3 with the motor rotating ad 700 RPM and 5 A current reference.

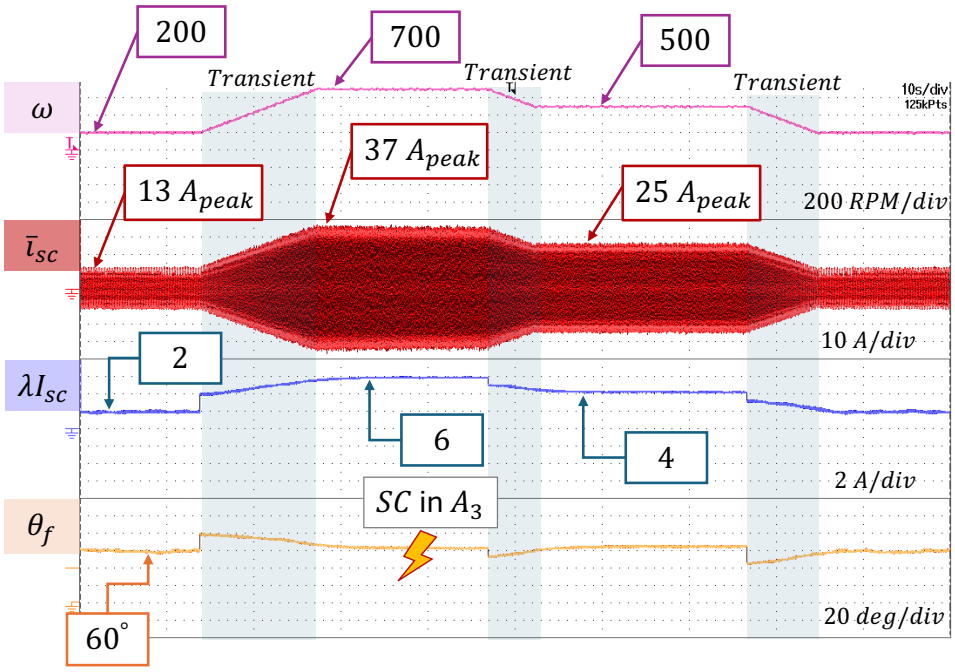

FIGURE 3.20: Fault estimation and identification in case of 10 shorted turns in the phase A_3 with the motor speed varying from 200 to 700 RPM and 5 A current reference.

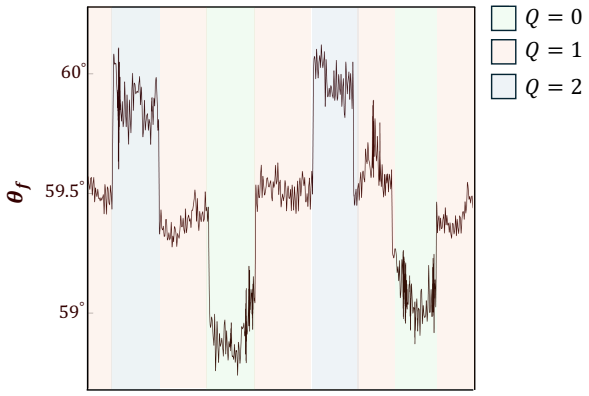

FIGURE 3.21: Effect of $\Delta\theta_f$ of the estimation of the magnetic axis of the phase affected the short circuit. The short circuit is inserted in the phase A_3.

Bibliography

[1] A. G. Yepes, D. S. B. Fonseca, H. R. P. Antunes, O. López, A. J. Marques Cardoso, and J. Doval-Gandoy, "Discrimination between eccentricity and interturn faults using current or voltage-reference signature analysis in symmetrical six-phase induction machines," *IEEE Transactions on Power Electronics*, vol. 38, no. 2, pp. 2421–2434, 2023.

[2] A. A. Rahman, A. Galassini, M. Degano, G. Buticchi, G. Cristián Pesce, C. Gerada, S. Bozhko, and H. A. Almurib, "Open and short circuit post-fault control strategies for multi-three-phase interior permanent magnet machines," *IEEE Transactions on Energy Conversion*, vol. 37, no. 1, pp. 163–174, 2022.

[3] A. Femia, G. Sala, L. Vancini, G. Rizzoli, M. Mengoni, L. Zarri, and A. Tani, "A machine learning-based inter-turn short-circuit diagnosis for multi-three-phase brushless motors," *IEEE Journal of Emerging and Selected Topics in Industrial Electronics*, pp. 1–11, 2023.

[4] X. Liu, W. Miao, Q. Xu, L. Cao, C. Liu, and P. W. T. Pong, "Inter-turn short-circuit fault detection approach for permanent magnet synchronous machines through stray magnetic field sensing," *IEEE Sensors Journal*, vol. 19, no. 18, pp. 7884–7895, 2019.

[5] V. Gurusamy, E. Bostanci, C. Li, Y. Qi, and B. Akin, "A stray magnetic flux-based robust diagnosis method for detection and location of interturn short circuit fault in pmsm," *IEEE Transactions on Instrumentation and Measurement*, vol. 70, pp. 1–11, 2021.

[6] M. Mengoni, L. Zarri, A. Tani, Y. Gritli, G. Serra, F. Filippetti, and D. Casadei, "Online detection of high-resistance connections in multiphase induction machines," *IEEE Transactions on Power Electronics*, vol. 30, no. 8, pp. 4505–4513, 2015.

[7] M. Mengoni, L. Vancini, A. Tani, Y. Gritli, L. Zarri, and C. Rossi, "On-line detection of magnet demagnetization in asymmetrical six-phase surface-mounted permanent magnet synchronous motor drives," in *2019 IEEE 12th International Symposium on Diagnostics for Electrical Machines, Power Electronics and Drives (SDEMPED)*, 2019, pp. 188–194.

[8] S. G. Lee, K.-S. Kim, J. Lee, and W. H. Kim, "A novel methodology for the demagnetization analysis of surface permanent magnet synchronous motors," *IEEE Transactions on Magnetics*, vol. 52, no. 3, pp. 1–4, 2016.

[9] H.-K. Lee, K.-H. Shin, T.-K. Bang, J.-H. Nah, and J.-Y. Choi, "Experimental verification and analytical study of influence of rotor eccentricity on electromagnetic characteristics of permanent magnet machine," *IEEE Transactions on Applied Superconductivity*, vol. 30, no. 4, pp. 1–5, 2020.

[10] F. Ito, K. Takeuchi, T. Kotsugai, and M. Matsushita, "A study on asymmetry of electromagnetic force modes of permanent magnet synchronous motors with rotor eccentricity," *IEEE Transactions on Magnetics*, vol. 57, no. 2, pp. 1–6, 2021.

[11] S. Reza Mortezaei, M. Hosseini Aliabadi, and S. Javadi, "Eccentricity fault detection in surface-mounted permanent magnet synchronous motors by analytical prediction, fem evaluation, and experimental magnetic sensing of the stray flux density," *Journal of Magnetism and Magnetic Materials*, vol. 589, p. 171441, 2024.

[12] I. Zamudio-Ramirez, J. J. Saucedo-Dorantes, J. Antonino-Daviu, R. A. Osornio-Rios, and L. Dunai, "Detection of uniform gearbox wear in induction motors based on the analysis of stray flux signals through statistical time-domain features and dimensionality reduction techniques," *IEEE Transactions on Industry Applications*, vol. 58, no. 4, pp. 4648–4656, 2022.

[13] P. A. Panagiotou, I. Arvanitakis, N. Lophitis, J. A. Antonino-Daviu, and K. N. Gyftakis, "A new approach for broken rotor bar detection in induction motors using frequency extraction in stray flux signals," *IEEE Transactions on Industry Applications*, vol. 55, no. 4, pp. 3501–3511, 2019.

[14] Z. Gong, X. Ba, C. Zhang, and Y. Guo, "Enhanced maximum torque per ampere control with predictable core loss for the interior permanent magnet synchronous motor," *IEEE Transactions on Applied Superconductivity*, vol. 34, no. 8, pp. 1–4, 2024.

[15] G. Feng, Y. Lu, C. Lai, B. Ding, and N. C. Kar, "Fault tolerant maximum torque per ampere (ft-mtpa) control for dual three-phase interior pmsms under open-phase fault," *IEEE Transactions on Industrial Electronics*, vol. 69, no. 12, pp. 12 030–12 041, 2022.

[16] Z. Mei, G.-J. Li, Z. Q. Zhu, R. Clark, A. Thomas, and Z. Azar, "Scaling effect on inter-turn short-circuit fault of pm machines for wind power application," *IEEE Transactions on Industry Applications*, vol. 59, no. 1, pp. 789–800, 2023.

[17] B. Vaseghi, B. Nahid-mobarakh, N. Takorabet, and F. Meibody-Tabar, "Inductance identification and study of pm motor with winding turn short circuit fault," *IEEE Transactions on Magnetics*, vol. 47, no. 5, pp. 978–981, 2011.

[18] A. Femia, G. Sala, M. Mengoni, L. Vancini, G. Rizzoli, L. Zarri, and A. Tani, "Stator imbalance in asymmetrical six-phase synchronous motor drives: High-resistance connections and mismanufactured winding," in *2023 IEEE 14th International Symposium on Diagnostics for Electrical Machines, Power Electronics and Drives (SDEMPED)*, 2023, pp. 172–178.

Chapter 4

Machine Learning for Fault Diagnosis

Artificial Intelligence has had a significant increase in popularity in recent years, making it one of the most attractive and promising technological developments of our time. This intriguing field not only provides new prospects but also covers almost all aspects of industry and scientific inquiry. This chapter presents two fault detection strategies that utilize Machine Learning (ML) for detecting, identifying and distinguishing stator faults such SCs, HRCs and MDs.

4.1 Machine Learning Algorithms

ML algorithms are divided into three main families: supervised learning, unsupervised learning, and reinforcement learning.

Supervised learning involves a collection of training instances (samples), whereby the input data comes along with pre-existing knowledge of the expected outputs, referred to as labels, targets or classes [1]. Regression and classification algorithms are part of this group. In regression, labeled instances are passed to an algorithm to fit a predictive model that can make predictions on new input data. In classification, the goal is to predict class category labels for new instances, based on previous observations.

In unsupervised learning ML algorithms are used to analyze and cluster unlabeled data sets. Techniques such as clustering and association belong to this family.

Reinforcement learning pertains to the process of acquiring the best behavior within a given environment with the objective of attaining the highest possible reward. The acquisition of optimum behavior occurs via the process of interacting with the environment and observing its responses. By virtue of its structure, it is widely used in the field of robotics.

The works presented in the following sections use classification methods to detect and estimate stator faults such as SCs, MDs and HRCs in dual-three-phase electric drives.

4.2 Short Circuit and Manufacturing Defects Fault Diagnosis Using Machine Learning

To meet the demands for reliability and performance, the use of advanced control and diagnostic methods is necessary due to the progress made in multiphase drives. AI approaches offer a highly successful solution to these problems [2; 3]. Indeed, the conventional analytical approach to defect identification sometimes requires making significant assumptions in order to establish the physical relationship among various variables. ML overcomes this issue by employing algorithms that have an inherent comprehension of how input and output data are correlated. Therefore, ML is extensively utilized in the field of faults diagnostics for power electronic converters [4] and electric motors [5–8]. Both domains utilize ML techniques in combination with model- and signal-based approaches to improve the advancement of fault-tolerant controls [9].

As detailed extensively in Section 3.1.3, inter-turn SCs play a significant role in the dangerous failures of electrical machines. Indeed, SC faults generate large uncontrollable circulating currents, resulting in torque fluctuations, vibrations, and rapid temperature rise. Therefore, it becomes essential to diagnose intern-turn SC failures in order to avoid catastrophic breakdowns. Fig. 4.1 depict an SC affecting a certain number of turns of the stator windings.

It is important to identify and distinguish SC from other faults that have less severity, such as MDs, in order to promptly intervene and assist in repairing the machine once it has been powered off. The fault localization is particularly helpful in multi-three-phase drives since, in the event of a fault, the specific set of three phase windings where the fault occurs can be disconnected to preserve the overall functionality of the drive, depending on the nature and severity of the fauilure.

The next section present a machine learning-based technique that enables the identification and differentiation of a short circuit fault.

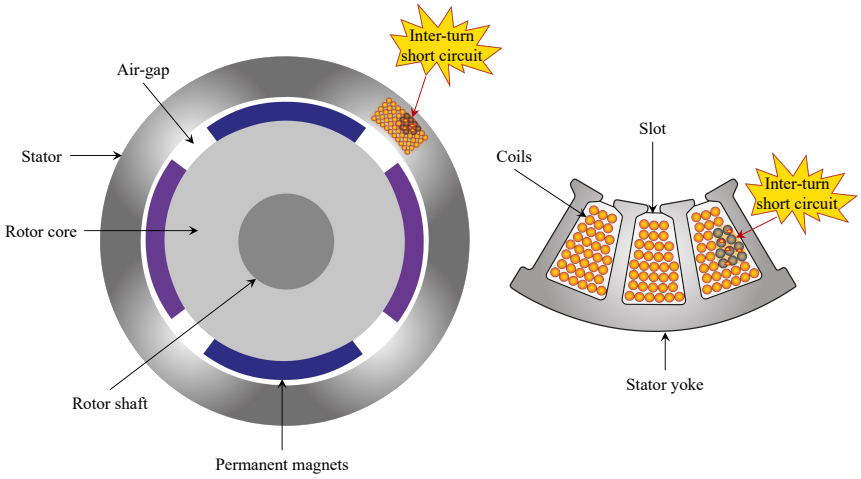

FIGURE 4.1: View of a short-circuit affecting 10 turns of the stator winding.

4.2.1 Vector Representation for Training Dataset

According to Sec. 2.2.3, through VSD approach, the six quantities of the dual-three-phase motor can be fully represented in terms of space vectors, which can be calculated by applying an extended Clarke transformation. Therefore, at steady-state operating conditions, when the motor rotates at constant angular speed ω, an ideal cotrol system ensures that the current space vectors are:

$$\begin{aligned} \bar{i}_1 &= \bar{i}_{ref} e^{j\omega t} \\ \bar{i}_5 &= 0. \end{aligned} \tag{4.1}$$

For a healthy motor, without asymmetries, thevoltage and flux vectors given for $\rho = 1$ and $\rho = 5$ are enough to fully describe the whole dual-three-phase drive. They can be expressed as complex Fourier series as follows:

$$\begin{aligned} \overline{v}_\rho &= \sum_{h=1}^{\infty} \overline{v}_\rho^{h+} e^{jh\omega t} + \sum_{h=1}^{\infty} \overline{v}_\rho^{h-} e^{-jh\omega t} \\ \overline{\varphi}_\rho &= \sum_{h=1}^{\infty} \overline{\varphi}_\rho^{h+} e^{jh\omega t} + \sum_{h=1}^{\infty} \overline{\varphi}_\rho^{h-} e^{-jh\omega t} \end{aligned} \tag{4.2}$$

where the notation $h+$ and $h-$ is used to identify the h-th harmonic component of the positive and negative sequences, respectively.

The stator voltage equation of the healthy machine can be written in terms of space vectors as follows:

$$\overline{v}_\rho = R_s \bar{i}_\rho + \frac{d\overline{\varphi}_\rho}{dt}. \tag{4.3}$$

If (4.1) and (4.2) are combined with (4.3), the balance of the fundamental harmonic (1+) for $\rho = 1$ yields:

$$\overline{v}_1^{1+} = R_s \bar{i}_{ref} + j\omega \overline{\varphi}_1^{1+} \tag{4.4}$$

while the other harmonic components are as follows:

$$\begin{aligned}
\overline{v}_1^{h+} &= jh\omega\overline{\varphi}_1^{h+} \\
\overline{v}_1^{h-} &= -jh\omega\overline{\varphi}_1^{h-} \\
\overline{v}_5^{h+} &= jh\omega\overline{\varphi}_5^{h+} \\
\overline{v}_5^{h-} &= -jh\omega\overline{\varphi}_5^{h-}.
\end{aligned} \tag{4.5}$$

In contrast, additional voltage contributions are required to keep the current waveform sinusoidal if a fault occurs or an asymmetry is present. In the case of asymmetrical windings, the main additional voltage contributions are expected to affect the positive and negative sequences at the fundamental frequency ($\overline{v}_1^{1+}$, $\overline{v}_1^{1-}$, $\overline{v}_5^{1+}$, $\overline{v}_5^{1-}$). Instead, in case of an Extra Turn (ET) in a phase or a short-circuit fault, the unbalanced electromotive forces produced by the rotor magnets cause time harmonics with an order higher than 1. The most important harmonic components are often at three times the fundamental frequency ($\overline{v}_1^{3+}$, $\overline{v}_1^{3-}$, $\overline{v}_5^{3+}$, $\overline{v}_5^{3-}$). Furthermore, since an SC current produces a pulsating airgap flux and, consequently, a torque ripple, the speed regulator is expected to partially compensate for this torque disturbance by generating distortion in both the current vector $\overline{i}_1$ and the voltage vector $\overline{v}_1$, while $\overline{v}_5$ is controlled to keep the current $\overline{i}_5$ at zero.

A change in $\overline{v}_5$ is a necessary but not sufficient condition to detect the presence of a fault. To diagnose the fault, $\overline{v}_5$ must include some specific harmonic components, i.e., those with order -1, +1, -3, and +3. The other harmonics of $\overline{v}_5$ are not used as diagnostic indices due to their lower magnitudes and because they are mainly caused by magnet-induced back-emf harmonics and slotting effects.

Fig. 4.2 illustrates the harmonics that arise in $\overline{v}_5$ in case of a SC fault. In what follows, a Diagnosis Strategy (DS) focused on the first and third time harmonic components of $\overline{v}_5$ is presented:

$$\overline{v}_{5,DS} = \overline{v}_5^{1+}e^{j\omega t} + \overline{v}_5^{1-}e^{-j\omega t} + \overline{v}_5^{3+}e^{j3\omega t} + \overline{v}_5^{3-}e^{-j3\omega t}. \tag{4.6}$$

The contributions to the diagnostic space vector $\overline{v}_{5,DS}$ in (4.6) are zero in the case of a healthy machine with sinusoidal back-emfs due to the rotor magnets, according to (4.5).

In contrast, the components $\overline{v}_5^{1+}$ and $\overline{v}_5^{1-}$ are expected to be present in case of asymmetries in the phase inductances and resistances. Finally, $\overline{v}_5^{3+}$ and $\overline{v}_5^{3-}$ arise from a MD such an ET in a stator winding , or a SC. These four complex vector contributions represent the diagnostic variables used to train the ML algorithms.

A dataset of the selected outputs ($\overline{v}_5^{1+}$, $\overline{v}_5^{1-}$, $\overline{v}_5^{3+}$ and $\overline{v}_5^{3-}$) for various operating conditions, including asymmetries and faults, for different values of i_d, i_q, and speed can be quickly evaluated

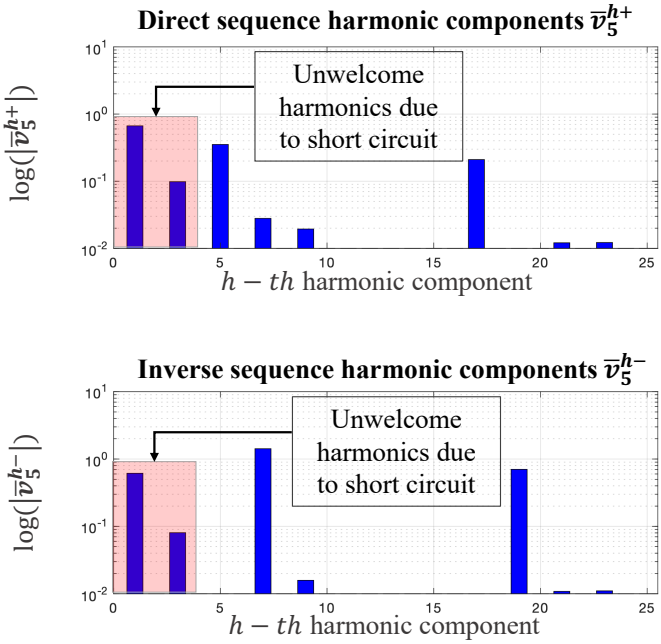

FIGURE 4.2: Time-harmonic contributions to the space vector $\overline{v}_5$. The significant terms that appear in $\overline{v}_{5,DS}$ due to a short circuit fault are highlighted.

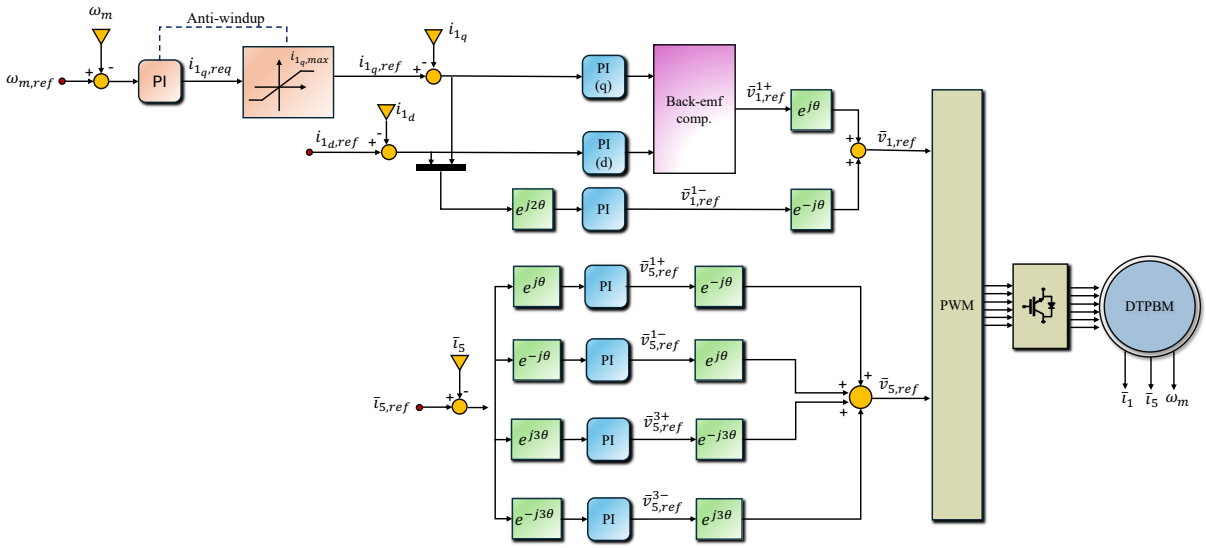

FIGURE 4.3: Control architecture.

by using the finite element model of the dual-three-phase motor presented in Sec. 3.1.4. The control architecture adopted for obtaining the just mentioned voltage harmonic components is illustrated in Fig. 4.3

4.2.2 Algorithms Used for Classification.

To test the effectiveness of the proposed diagnostic strategy, five ML models (see Fig. 4.4) have been implemented:

1. The Support Vector Machine (SVM) model aims to find a hyperplane in an N-dimensional

space (N is the number of features) able to separate data points so that they can be correctly classified;

2. The K-Nearest Neighbors (KNN) model classifies each data point according to the similarity with those previously stored;

3. The Multilayer Perceptron (MPL) model is a feedforward algorithm including input and output layers, and one or more hidden layers with many neurons stacked together. Therefore, it is a "deep method", and its classification ability is based on the back-propagation mechanism;

4. The eXtreme Gradient Boosting (XGBoost) model is a decision-tree-based algorithm, which applies the principle of "boosting weak learners", using the gradient descent architecture to carry out the classification task;

5. The Gaussian Naive Bayes (GNB) model uses the Bayes theorem for the classification, assuming that each class follows a Gaussian distribution and the independence of the features.

Before starting the training task, the dataset was preprocessed to reduce its dimensionality. This approach is common in ML as it allows a smaller dataset size to be used without losing the information needed for classification. Since the data are not separable in a linear way, Kernel Principal Component Analysis (KernelPCA) is used for dimensionality reduction. KernelPCA employs a spectral decomposition to determine the directions (eigenvectors) of the maximum variance, i.e., the directions where more information about the data frame is contained. This decomposition allows obtaining a smaller set of "artificial" orthogonal variables, starting from a set of correlated numerical variables, without losing information. Moreover, the variables are normalized in advance to prevent their variability from affecting the results of the KernelPCA. Normalization, which entails the reshaping of numerical columns so they conform to a standard scale, is a critical process for data sets that have diverse units or magnitudes across various features. The primary objective of normalization is to establish a shared scale for the data while

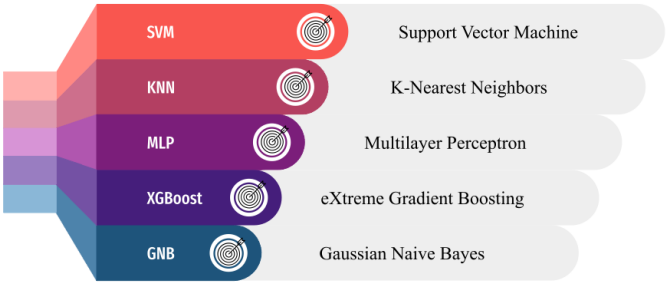

FIGURE 4.4: Employed machine learning models.

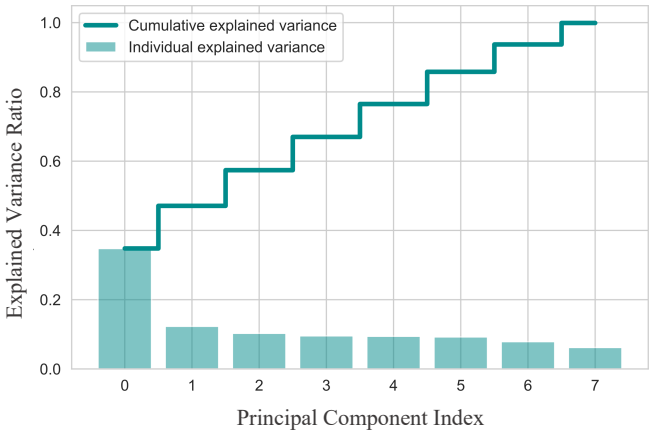

FIGURE 4.5: PCA results for the training data frame.

preserving the inherent variations in the range of values. This typically entails the rescaling of features to a standard range, which is typically between 0 and 1. At the same time, features may be modified to have a mean of 0 and a standard deviation of 1. The latter approach is implemented in this investigation. The mean column value is subtracted from each sample, and the resulting value is then divided by the standard deviation. Fig. 4.5 displays the variance of the variables in the data frame along the new orthogonal directions. This result shows that eight directions (eigenvectors) are sufficient to describe 100% of the total data frame variance. Obviously, for a graphical representation, just three directions are needed. Fig. 4.6 shows the samples of the training data frame in a space with lower dimensionality defined by the first three principal components. Although these three directions account for just 60% of the total variance, it is worth noting that some of the attributes are separable in the $3D$ space. For example, samples reflecting ET in different phases are distinctly represented by separable lines. This makes it easier for ML algorithms to perform the classification task. Once pre-processed, the data frame is used for training (see Fig. 4.7).

Another essential aspect of an ML model concerns the hyperparameters, which directly control the learning process and determine the values of the model parameters that a learning algorithm ends up learning. The hyperparameters of each ML model are optimized with the Grid-Search technique in order to customize the models for the training task. The data frame used for the training task includes the following variables:

- **Targets**: labels for each class to be classified (Tab. 4.1);
- $\boldsymbol{\omega}$: mechanical speed of the rotor;
- $\boldsymbol{i_d}$: $d-$axis current (directly correlated to the stator flux);
- $\boldsymbol{i_q}$: $q-$axis current (directly correlated to the torque);

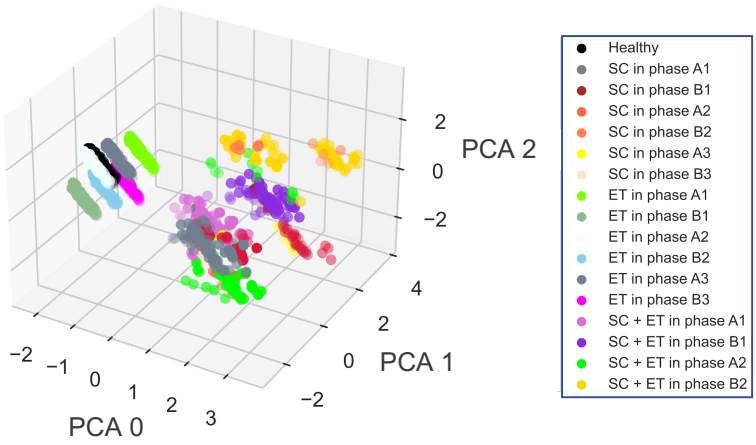

FIGURE 4.6: Samples of the training data frame mapped in a space defined by the first three principal components.

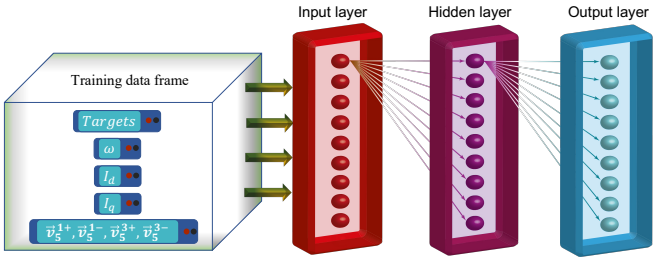

FIGURE 4.7: Proposed training data frame as input to a general multilayer neural network structure.

- $\overline{\boldsymbol{v}}_{\boldsymbol{5,DS}}$: harmonics contributions, in magnitude and phase, due to SC and ET.

TABLE 4.1: Targets explanation

Target	Short circuit (SC)	Extra turn (ET)
0	No	No
1	In phase A_1	No
2	In phase B_1	No
3	In phase A_2	No
...	...	...
7	No	In phase A_1
8	No	In phase B_1
...	...	...
13	In phase A_1	Yes (phase not predicted)
14	In phase B_1	No (phase not predicted)
...	...	...

4.2.3 Experimental Results

Considering the nomenclature for a general multi-class confusion matrix shown in Fig. 4.9, the performance of the ML models is evaluated through the following metrics (Tab. 4.2):

- Training accuracy: accuracy of the model on actual data used for training (70% of the data frame obtained with Matlab/FEMM simulations);

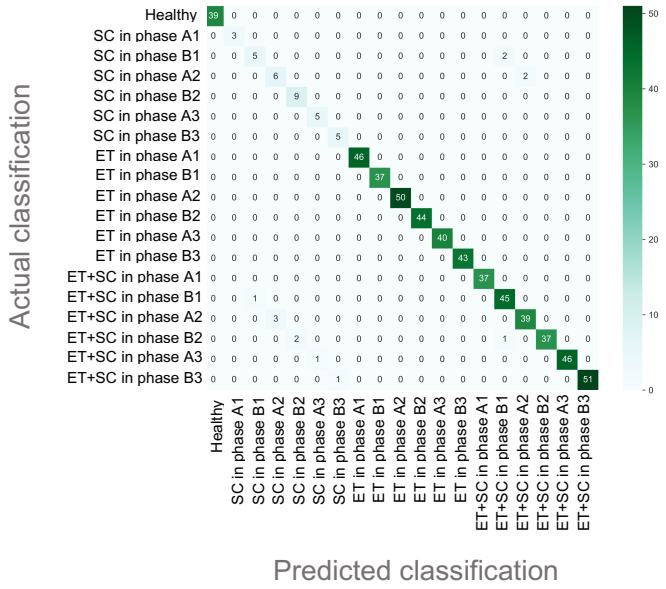

FIGURE 4.8: Confusion matrix obtained from the test data frame with the SVM technique.

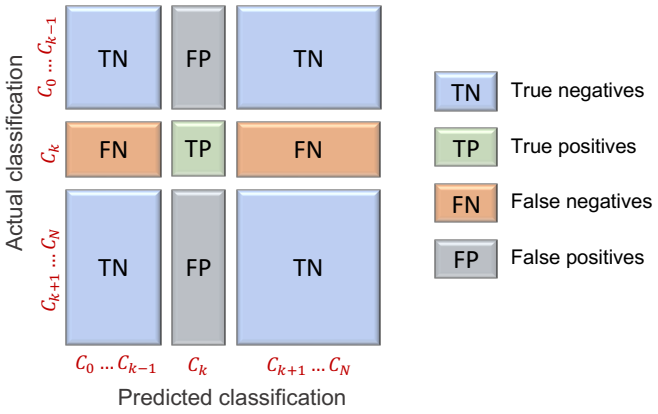

FIGURE 4.9: General confusion matrix for a multi-class model. The generic predicted class is labeled with C_k.

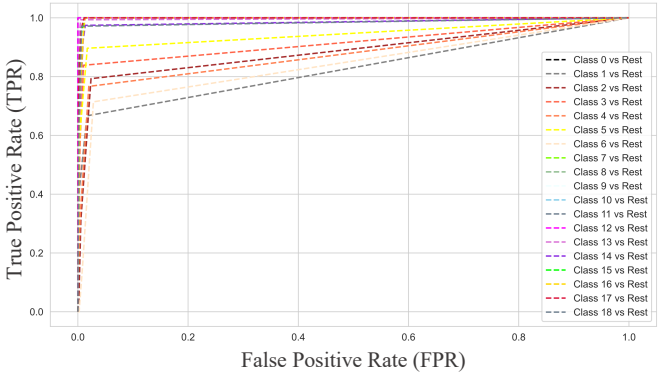

FIGURE 4.10: ROC (OvR strategy) curves obtained from the KNN model considering the test data.

- Test accuracy: accuracy of the model on data never used for training (30% of the data frame obtained with Matlab/FEMM simulations);

- Test bench accuracy: accuracy of the model on data directly obtained from the test bench acquisitions;
- k-fold accuracy: accuracy of the model on a limited set of data obtained by dividing the overall Matlab/FEMM data frame into k non-overlapping folds. Each kth fold can be used as a retained test set, while all other bends are collectively used as a training dataset;
- Precision (PRE): the number of instances that are relevant, out of the total instances the model retrieved, calculated as $PRE = \frac{TP}{TP+FP}$;
- Recall (REC): the number of instances that the model correctly identified as relevant out of the total significant instances, calculated as $REC = \frac{TP}{TP+FN}$;
- AUC: the area under the Receiver Operator Characteristic (ROC), which are probability curves that plot the True Positive Rate (TPR) against the False Positive Rate (FPR), which are respectively defined as $TPR = \frac{TP}{FN+TP}$ and $FPR = \frac{FP}{FP+TN}$. AUC measures the ability of an ML model to distinguish among classes and is usually adopted for binary classification. AUC may be interpreted as the likelihood that a randomly chosen sample would be properly classified for various thresholds of the decision boundary. A model whose predictions are 100% wrong has an AUC equal to zero, whereas the AUC is one when the predictions are 100% correct.
- F1-score: it combines the precision and recall of a classifier into a single metric by taking their harmonic mean, calculated as $F1 = 2\frac{PRE \times REC}{PRE+REC}$.

Since the problem involves 19 classes, the last four metrics (PRE, REC, AUC, and F1-score) are determined using a "One vs Rest" (OvR) approach. It entails choosing one class and treating it as positive while treating the remaining ("the rest") as negative. This approach allows each class to be compared against all the others at the same time. For instance, Fig. 4.10 shows the ROC curves obtained with the OvR strategy considering the K-Nearest Neighbors (KNN) algorithm. OvR approach leads to consider the percentages in Tab. 4.2 as a macro average value.

Fig. 4.8 shows the confusion matrix resulting from the classification that the SVM model performs on the test data frame. As can be seen, almost all values are on the diagonal. This implies a match between predicted and actual values.

Choosing the correct number of instances (rows of the data frame) for the training task is always an important matter. In fact, a wrong choice could lead to problems such as overfitting (too many parameters in the model and a high variability of the classification) and underfitting (few parameters in the model and a high discrepancy in classification). In the first case, the

TABLE 4.2: Metrics adopted for evaluating the ML models

Model	Training accuracy	Test accuracy	Test bench accuracy	...
SVM	99.5%	97.3%	96.2%	...
KNN	96.6%	93.5%	93%	...
MLP	99.9%	95%	66.6%	
XGB	99.9%	95%	66%	
GNB	90.5%	88.1%	38.5%	
...	k-fold (k=5)	Precision	Recall	...
...	$97 \pm 2\%$	92.8%	95.2%	...
...	$93 \pm 1\%$	80.9%	78.9%	...
...	$94 \pm 1\%$	81.3%	82%	
...	$94 \pm 2\%$	90.9%	82.6%	
...	$89 \pm 2\%$	72.9%	74.1%	
...	AUC	F1-measure		
...	99.9%	93.7%		
...	78.9%	79.68%		
...	82%	80.7%		
...	82.6%	84.7%		
...	74.1%	72%		

model is too complex and sensitive to training data (high variance and low bias). In the second case, the model can not accomplish a good classification since it has insufficient complexity (high bias and low variance). Thereby, the suspicion of overfitting arises when training accuracy and test accuracy curves are too far from each other. In contrast, when the models suffer from underfitting, both the mentioned curves drop rapidly to very low levels of accuracy.

An effective ML model has to achieve a balance between variance and bias. Additionally, the number of samples should not be excessively high to avoid needless computational work. Fig. 4.11 shows the accuracy curves and the optimal point representing the chosen number of instances of the training data frame for the Support Vector Machine (SVM) model. This approach allows one to find the optimal number of instances for each ML model, avoiding overfitting and underfitting.

The performance of the proposed AI-based fault detection strategies has been verified by experimental tests on the dual-three-phase prototype shown in Fig. 3.14. The main motor parameters are listed in Tab. 4.4.

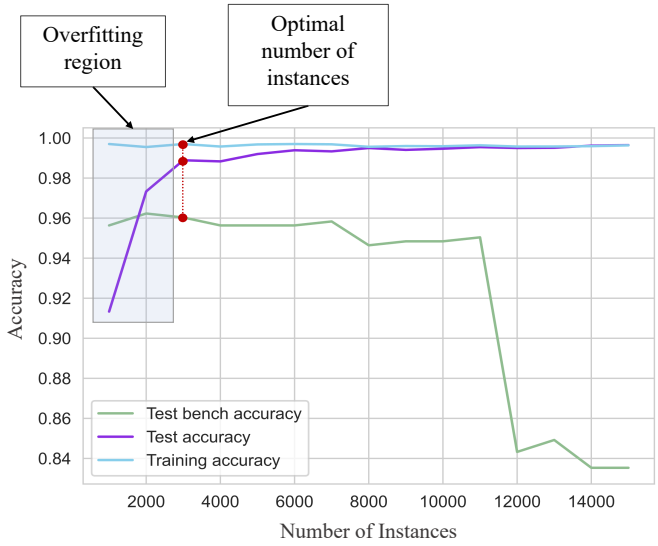

FIGURE 4.11: Accuracies obtained from SVM model by varying the training data frame number of instances.

4.2.4 Experimental Setup and Data Collection

The control system is implemented by using a dSPACE platform (MicroLabBox, DS1104), which manages the six-phase power converter through fiber-optic cables. The switching frequency of the converter is nearly 8.8 kHz. An Elektro-Automatik power supply (EA-PS 9500−20) provides the drive DC link voltage, and a DC generator is employed as a mechanical load.

Experimental tests are performed at reduced speed to avoid damaging the electric motor under test (e.g., overheating and demagnetization). In particular, the maximum speed of the tests is set to about 700 RPM to maintain the SC current below 60 A.

A SC of 10 turns coincides with a short circuit of a coil. This means shorting 1/8 of the machine (12.5%). Conversely, 1 ET represents a variation of 1/81, that is 1.234%.

Fig. 4.12 shows a comparison between experimental and semi-analytical results when the motor features an SC of 10 turns in phase B3 and an ET in phase A3, while rotating at 700 rpm and controlled with a current i_{d1} of -5 A and a current i_{q1} of 2 A. The results show that the phase and short circuit currents have similar waveforms, whereas the diagnostic vectors ($\overline{v}_5^{1+}$, $\overline{v}_5^{1-}$, $\overline{v}_5^{3+}$ and $\overline{v}_5^{3-}$) match the predicted values less precisely but still represent the signature of the motor asymmetrical behavior. The mismatch between the simulation and experimental results is relatively small, and it is not simple to identify the primary cause. Some improvements may be expected if a more accurate system model is used. Also, the motor control algorithm cannot perfectly track the current references due to the PI regulators bandwidth and finite gains.

The SC resistance R_{sc} was updated to match the SC current(red) with the measured value (blue).

Three significant operating conditions are considered: no SC, a SC of 10 series turns in phase A_3 and a SC of 10 series turns in phase B_3. Furthermore, the motor has an ET in one coil (not

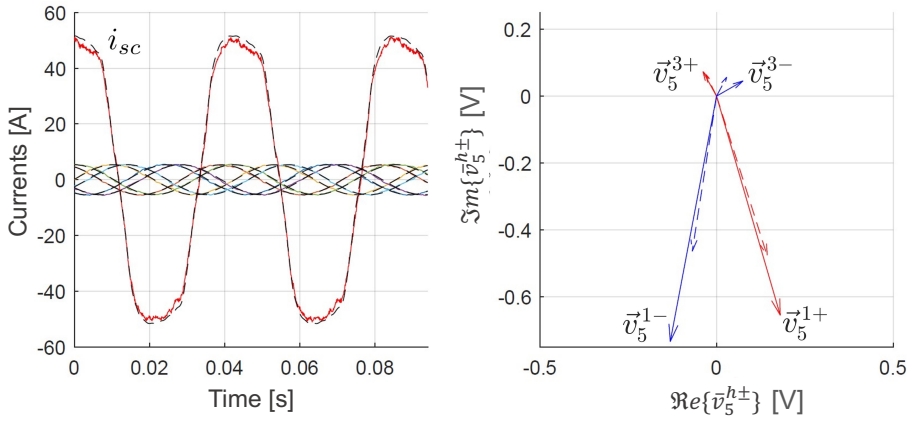

FIGURE 4.12: Experimental results in the case of a short circuit in phase B_3: currents $i_{A_1}, i_{B_1}, i_{A_2}, i_{B_2}, i_{sc}$ and diagnostic vectors $\overline{v}_5^{h+}$ (red) and $\overline{v}_5^{h-}$ (blue). The semi-analytical results are in dashed lines.

affected by short circuit faults) of the phase A_3.

All the operating conditions mentioned above have been simulated to derive a wide experimental dataset (504 instances). Each instance is labeled with a target index, depicting the operating condition, according to the training data frame structure. Thus, the test bench data is employed to assess the effectiveness of the proposed strategy in correctly classifying the type of fault and its localization.

4.2.5 Models Assessment

Tab. 4.2 illustrates the results of the considered ML models. This comparative study clearly shows that the best of the investigated ML techniques, in terms of metrics, is the SVM. It reaches an accuracy of 96.2% on the experimental data, which means that the ML algorithm can almost flawlessly predict the health state of the machine among all the 504 operating conditions. The KNN model exhibits good performance, although the precision and recall metrics differ by about 10% from the SVM. The MLP and XGB models show very similar performance and are both unable to reach high accuracy when assessed with the test bench data frame. Finally, GNB exhibits the poorest performance among all the metrics. The difference in the outcomes is attributable to the intrinsic characteristics of ML techniques. Each ML algorithm statistically identifies the class to which each sample belongs. The SVM technique relies on identifying hyperplanes that can distinguish samples according to their class membership. After identifying the plane of separation between classes, the likelihood of a sample belonging to a specific class is calculated. Conversely, the KNN algorithm assesses the similarity degree of each sample in relation to its adjacent sample. The likelihood that the two samples belong to the same class is then determined. In this investigation, the SVM technique turned out to be the most effective. Consequently, it can be deduced that the algorithm effectively identifies the separating

hyperplanes across classes. Hosseini et al. [10] provide a detailed explanation of how ML models work.

The investigation that has been presented was enhanced with a more sophisticated control system in the subsequent section. This enabled the achievement of better results.

4.3 Short Circuit and High-Resistance-Connection Diagnosis Using Machine Learning

The diagnostic method presented in Sec. 4.2 is focused on the detection of SCs and MDs, such as variations in the number of turns, without estimating the failure entity. In addition, the drive was supposed to have sinusoidal reference currents, as stated by (4.1), that are obtained by implementing a complex control architecture including several resonant PI regulators. Under this assumption, the estimated voltage harmonic components due to the faults were the only variable including the signature of the faults. However, that control was highly demanding in terms of computational efforts and most of the current regulators were not exploited during the healthy motor operation, making the solution critical for drives in industrial applications. The solution provided in this Section addresses those issues by utilizing only the minimum number of current PI regulators, hence significantly reducing the complexity of the control system. Furthermore, the inevitable ripple of the phase currents is taken into account.

The asymmetry in the phase impedances due to HRC is also considered and the phase in which it occurs is accurately predicted. Hence, the dissertation can be seen as an extension of the research reported in Sec. 4.2.

4.3.1 Control System

In Sec. 4.2, as anticipated, the phase currents have been supposed sinusoidal considering PI regulators with an infinite bandwidth. Conversely, in the actual control algorithm (see Fig. 4.13) the tuning of the control parameters K_{p1}, K_{i1}, K_{p5}, and K_{i5} translates into transfer functions that can be analyzed separately for each harmonic component as follows:

$$\begin{aligned} \bar{v}_{dq1} &= (K_{p1} + \tfrac{K_{i1}}{s})[(i_{d1,ref} + j i_{q1,ref}) - (i_{d1} + j i_{q1})] \\ \bar{v}_{dq5} &= (K_{p5} + \tfrac{K_{i5}}{s})[(i_{d5,ref} + j i_{q5,ref}) - (i_{d5} + j i_{q5})]. \end{aligned} \tag{4.7}$$

At steady-state operation, the synchronous PI regulators ensure zero tracking error of the current sequences they are synchronized with. Because of the angles chosen for the synchronization of the PI regulators and the zero reference current for space 5, the fundamental direct sequence in space 1 and the inverse sequence in space 5 are perfectly tracked. Conversely, all

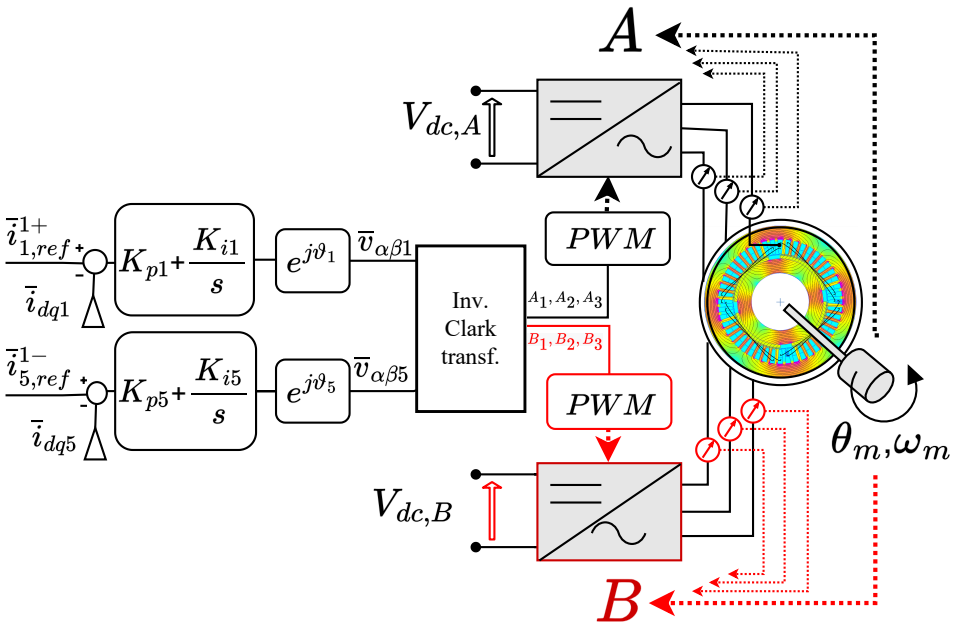

FIGURE 4.13: Control architecture of the dual three-phase drive. the transfer functions for the pair of PI regulators for the control of the d-q currents in the subspaces 1 and 5 are highlighted. The eight coils of one of the motor phase A_1 are drawn in the view of an FE simulation result. For one of these coils, the geometry of the simulated slot conductors is also visible..

the other sequences have current values that are not null despite their zero reference values. Therefore, the transfer functions of the PI regulators lead to the following set of equations:

$$\begin{aligned}
&\bar{i}_1^{1+} = i_{d1,ref} + j i_{q1,ref} \\
&\bar{v}_1^{h\pm} = -(K_{p1} + \tfrac{K_{i1}}{j\omega(h\mp1)})\bar{i}_1^{h\pm} \qquad h\pm \neq 1+ \\
&\bar{i}_5^{1-} = 0 \\
&\bar{v}_5^{h\pm} = -(K_{p5} + \tfrac{K_{i5}}{j\omega(h\pm1)})\bar{i}_5^{h\pm} \qquad h\pm \neq 1-.
\end{aligned} \tag{4.8}$$

4.3.2 Equations of the Electric Motor

The phase voltage equation for a motor winding without faults is:

$$v_k = R_k i_k + \sum_{z=1}^{6} L_{z,k}\frac{di_z}{dt} + e_k \tag{4.9}$$

where R_k is the phase resistance of phase k, $L_{z,k}$ identifies the inductances of the six-phase winding, and e_k is the rotor back electromotive force induced in phase k. In steady-state, each phase variable x_k in (6.1) can be rewritten in terms of representative phasors:

$$x_k = \sum_{h=1}^{\infty} \Re\{\overline{X}_{kh}\ e^{jh\omega t}\} = \sum_{h=1}^{\infty} \tfrac{1}{2}[\overline{X}_{kh}\ e^{jh\omega t} + \overline{X}^*_{kh}\ e^{-jh\omega t}] \tag{4.10}$$

and, for each harmonic, the 6-phase variables of the winding identify the representative vector $\overline{\mathbf{X}}_{\mathbf{6ph,h}}$:

$$\overline{\mathbf{X}}_{\mathbf{6ph,h}} = [\overline{X}_{A1h}\,\overline{X}_{A2h}\,\overline{X}_{A3h}\,\overline{X}_{B1h}\,\overline{X}_{B2h}\,\overline{X}_{B3h}]'. \tag{4.11}$$

For each harmonic h the phasor voltage equations derived from (6.1) must be simultaneously solved. In matrix form, remembering that the current derivatives in the phasors domain can be rewritten as $\frac{d\bar{I}_{kh}}{dt} = jh\omega\bar{I}_{kh}$, the problem is written as follows:

$$\overline{\mathbf{V}}_{\mathbf{6ph,h}} = \hat{\mathbf{Z}}_{\mathbf{h}}\bar{\mathbf{I}}_{\mathbf{6ph,h}} + \overline{\mathbf{E}}_{\mathbf{h}}. \tag{4.12}$$

In case of a fault in the motor winding, the main difference in the solution of the problem is in the values of the elements of the 6x6 matrix $\hat{\mathbf{Z}}_{\mathbf{h}}$ and 6 element vector $\overline{\mathbf{E}}_{\mathbf{h}}$. The methodology to identify the elements of $\hat{\mathbf{Z}}_{\mathbf{h}}$ and $\overline{\mathbf{E}}_{\mathbf{h}}$ from an accurate FE-based model was presented in Sec. 3.1.4.

Reminding that the common-mode variables for the two subwindings A and B are not used in the monitoring algorithm, four space vector (i.e., eight equations) are identified by applying the VSD transformation (2.8) for $\rho = 1, 5$ to (6.4). In particular, there are two space vector equations for the direct sequences and two for the inverse sequences of each time harmonic h-th in (6.4):

$$\begin{bmatrix} \overline{\mathbf{X}}_{\mathbf{SV,h+}} \\ \overline{\mathbf{X}}^*_{\mathbf{SV,h-}} \end{bmatrix} = \begin{bmatrix} \hat{\mathbf{C}}_{\mathbf{VSD}} \\ \hat{\mathbf{C}}_{\mathbf{VSD}^*} \end{bmatrix} \overline{\mathbf{X}}_{\mathbf{6ph,h}} \tag{4.13}$$

where $*$ is the cojugate operator.

The matrix $\hat{\mathbf{C}}_{\mathbf{VSD}}$ determines the VSD transformation (2.8) rewritten in terms of matrix form as:

$$\mathbf{x}_{\alpha\beta} = \hat{\mathbf{C}}_{\mathbf{VSD}}\,\mathbf{x}_{\mathbf{6ph}} \tag{4.14}$$

with $\mathbf{x}_{\alpha\beta} = [x_{\alpha 1}\, x_{\beta 1}\, x_{\alpha 5}\, x_{\beta 5}]'$ and $\mathbf{x}_{\mathbf{6ph}} = [x_{A1}\, x_{A2}\, x_{A3}\, x_{B1}\, x_{B2}\, x_{B3}]'$.

The eight space vector equations, which must be solved together with the eight space vector control transfer functions relationships in (4.8), are found by applying (4.13) to (6.4) as follows:

$$\begin{bmatrix} \overline{\mathbf{V}}_{\mathbf{SV,h+}} \\ \overline{\mathbf{V}}^*_{\mathbf{SV,h-}} \end{bmatrix} = \begin{bmatrix} \hat{\mathbf{C}}_{\mathbf{VSD}} \\ \hat{\mathbf{C}}_{\mathbf{VSD}^*} \end{bmatrix} \left(\hat{\mathbf{Z}}_{\mathbf{h}} \begin{bmatrix} \hat{\mathbf{C}}_{\mathbf{VSD}} \\ \hat{\mathbf{C}}_{\mathbf{VSD}^*} \end{bmatrix}^{-1} \begin{bmatrix} \bar{\mathbf{I}}_{\mathbf{SV,h+}} \\ \bar{\mathbf{I}}^*_{\mathbf{SV,h-}} \end{bmatrix} + \overline{\mathbf{E}}_{\mathbf{h}} \right) \tag{4.15}$$

for each h-th time harmonic, where $\overline{\mathbf{X}}_{\mathbf{SV,h\pm}} = [\Re_e\{\bar{x}_1^{h\pm}\}, \Im_m\{\bar{x}_1^{h\pm}\}, \Re_e\{\bar{x}_5^{h\pm}\}, \Im_m\{\bar{x}_5^{h\pm}\}]'$. The sixteen equations included in (4.8) and (4.15) completely identify the solution for sixteen phase variables (eight currents and eight voltages). This can be understood by reminding that for each

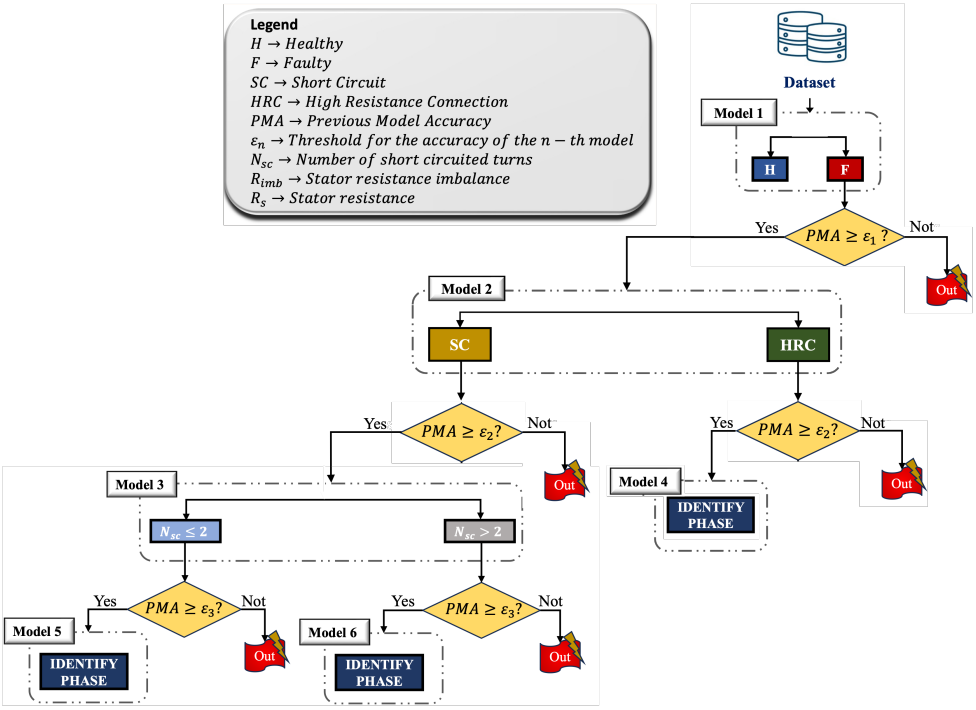

FIGURE 4.14: Proposed tree-based schema for fault classification.

of the six phase currents (or voltages) there are four degrees of freedom due to the two common-mode components which are not analyzed. These four degrees of freedom are represented in the steady state solution by four phasors, which are complex numbers made of a magnitude and a phase angle, resulting in a total of eight variables to be determined for the solution of the problem.

4.3.3 Imbalanced Classes

The majority of ML models are specifically intended to optimize accuracy and minimize errors. Therefore, ML algorithms tend to exhibit optimal performance when the number of samples in each class is nearly balanced. In circumstances of an imbalanced class distribution within the dataframe, the accuracy of the model is significantly affected. In such scenarios, a high accuracy may be attained by only predicting the majority class, but this approach fails to adequately capture the minority class. For instance, when the class distribution indicates that the majority class accounts for 99% of the data, it becomes challenging to accurately identify the minority class samples.

In order to address the issue of imbalanced classes, one potential approach involves using oversampling techniques that include duplicating random samples from the minority class, or undersampling techniques that involve deleting random samples from the majority class. In the first scenario, there is a concern that the ML model may exhibit overfitting, which refers to the acquisition of excessive information beyond what is required for effective learning. Conversely,

in the second scenario, there is a danger of underfitting, where crucial information may be overlooked, resulting in poor performance.

The suggested tree-based methodology (see Fig. 4.14) allows for independent optimization of each ML algorithm, allowing for optimum selection of whether to oversample or undersample the data in each branch of the tree architecture. The Synthetic Minority Oversampling Technique (SMOT) and the NearMiss approach are employed for class balancing in this study [11; 12].

4.3.4 Feature Selection

When implementing ML techniques, it is important to ascertain the selection of features (i.e., columns of the dataset) to be provided to the algorithms. This selection process aims to reach a balance between underfitting and overfitting, which is sometimes referred to as the bias-variance trade-off. Furthermore, the reduction in the number of features leads to a decrease in the computing time required for the training phase. Several types of feature selection strategies have been extensively documented in the academic literature [13], exhibiting varied degrees of appropriateness for the specific characteristics of the dataset being analyzed.

As stated in Sec. 2.2.3, when the motor is operating in healthy conditions, the quantities given in subspace α_5-β_5 are equal to zero and just the fundamental component rotating in the subspace α_1-β_1 is present. On the other hand, in the event of a failure, the control system acts by applying voltage harmonics at a certain frequency to address the existing imbalances caused by the fault. Consequently, specific additional harmonics emerge in the subspace α_5-β_5. That is why the variables defined in α_5-β_5 are appropriate for diagnosing and characterizing motor faults.

In this study, two feature selection algorithms are utilized: ANOVA and Chi2. In order to strengthen the outcome, the results in common between the two outcomes obtained from the aforementioned algorithms was taken into account. The features that were visually emphasized in yellow in Fig. 4.15 were subsequently chosen.

The importance of each selected feature is evident by using a partial dependence plot, which shows the marginal effect that a feature have on the predicted outcome of the ML model. For instance, the partial dependence analysis conducted on $\bar{v}_5^{5+}$ and $\bar{v}_5^{7-}$ is depicted in Figure 4.16. By examining the points highlighted by red crosses, it can be observed that when $\bar{v}_5^{5+}$ is equal to 0.5 V, there is an 80% probability of the machine being faulty and a 20% probability of it being healthy. As expected, a higher amplitude of voltage harmonics $\bar{v}_5^{7-}$ is directly associated with a higher probability of machine malfunctioning.

It is noteworthy to note that, as depicted in Fig. 4.14, each branch of the tree represents an independent ML model. Consequently, the feature selection procedure could be implemented for

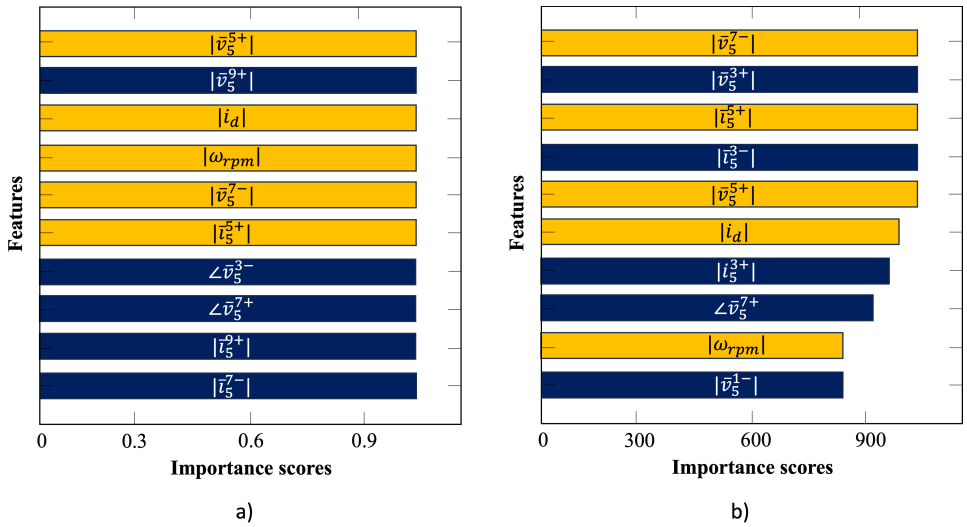

FIGURE 4.15: Feature importance scores. a) Using Chi2 algorithm. b) Using ANOVA algorithm. The yellow columns indicate where the two findings meet.

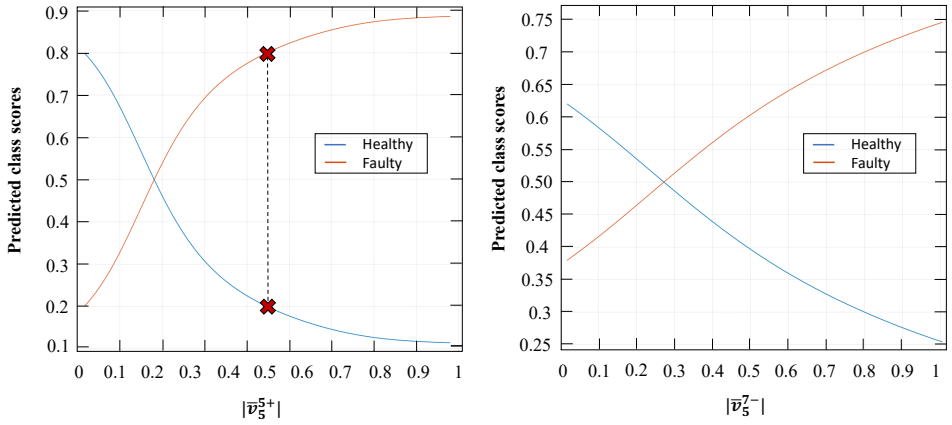

FIGURE 4.16: Partial dependence results usig two featurs of the training data.

each single model. Notwithstanding this, the features emphasized in Fig. 4.15 have been found to be the most relevant for accurate fault prediction in all ML models included in the tree-based schema, except for those responsible to localize the faulty phase (model 4, model 5, model 6), which utilized the phase in degrees rather than the magnitude of features selected. The parallel coordinate plot in Fig. 4.17 shows how the selected features contribute to the specific outcomes in model 6, which is responsible for localizing the phase in which a SC with a number of shorted turns greater than 2 ($N_{sc} > 2$) occurs.

4.3.5 Training Procedure

The training procedure enables the generation of knowledge by ML models, allowing them to discern patterns and relationships within data. The latter are organized in a tabular format, with each row representing a certain class.

The FE approach described in Sec. 3.1.4, along with the equations of the dual-three-phase

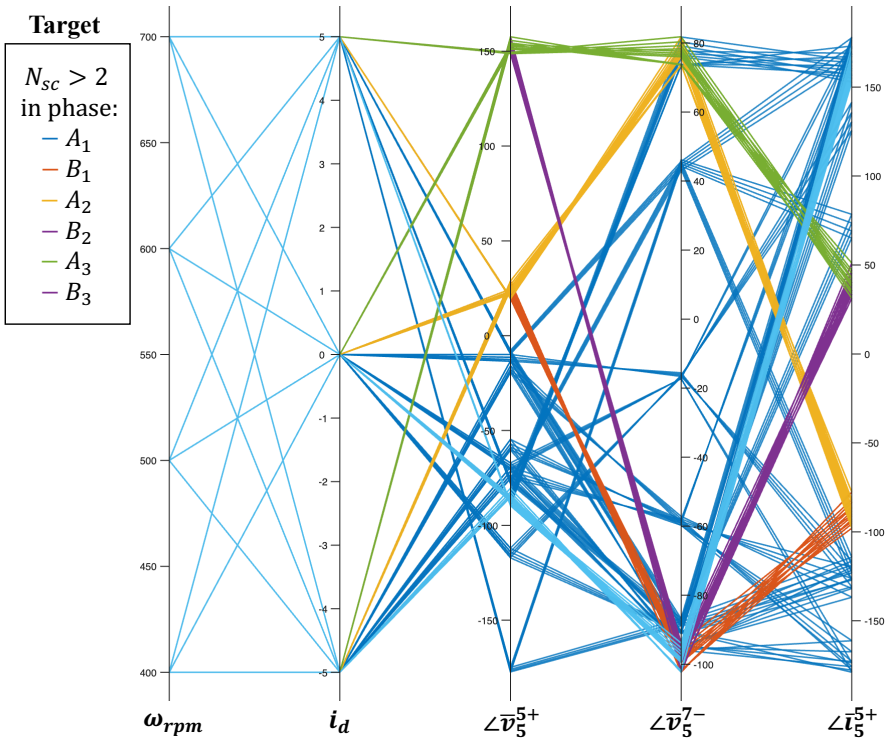

FIGURE 4.17: Parallel coordinates results for model 6 using training data.

machine, allows simulating various failure scenarios related to HRCs and SCs. It enables the extraction of the voltage and current harmonics components in the α_1-β_1 and α_5-β_5 subspaces that result from SC and HRC. Among all the harmonics components, just those selected by the feature selection process have been used for training purpose. The simulation and the training processes have been implemented using an Workstation with an Intel Core i9-13900K Processor, 128GB DDR5 RAM and NVIDIA Quadro RTX A4000 16GB GDDR6 Graphic Card.

The tree-based methodology shown in Fig. 4.14 enables the partitioning of the collected data into several smaller datasets. Each of these sub-dataset is then used for classification inside its respective branch of the tree. This enables the reduction of the number of samples (rows of the dataset) preventing overfitting.

After training each model individually, they were evaluated using a test dataset that includes samples obtained from the PMMTP prototype whose main parameters are listed in Tab. 4.4.

4.3.6 Test Operating Conditions

Data for creating the test dataset were gathered using the control system architecture shown in Fig. 4.13. The control system is executed utilizing a dSPACE platform (MicroLabBox, DS1104), which controls the operation of the six-phase power converter via fiber-optic cables. A power supply unit from Elektro-Automatik (EA-PS 9500 - 20) is used to provide the DC link

voltage for the drive system. Additionally, a DC generator is used as a mechanical load. Fig. 3.14 shows the overall setup.

Since no extra resistance was used for limiting the SC current, the data have been collected at a speed that is half of the rated one. Indeed, at this speed, the magnitude of the SC current is around five times the rated current of the motor, which is a value reachable without the risk to demagnetize the motor. Furthermore, the objective of the work is to examine the fault at its first phase, prior to it attaining catastrophic circumstances. Therefore, there is no need to reach high speeds.

The dual-thee-phase motor prototype permits access to the stator windings, allowing the possibility to shorten either 2 or 10 turns of phase B_3 (or A_3) via an external switch. These two faulty circumstances are denoted as $N_{sc} \leq 2$ and $N_{sc} > 2$, respectively. Furthermore, an extra resistance may be incorporated into phase A_2 to emulate an HRC that is about 60% of the stator phase resistance.

Finally, some samples were randomly removed to create an unbalanced test dataset and asses the ability of the ML models to predict even unbalanced classes.

4.3.7 Models Assessment

The resulting tree structure (see Fig. 4.14) enables the evaluation of many ML models for each branch of the tree, then choosing the one that demonstrates superior performance. The results obtained using the test data and the best algorithms are shown in Fig. 4.18. The use of four distinct algorithms, namely Random Forest (RF), K-Nearest Neighbors, Feedforward Neural Network (FNN), and Support Vector Machine (SVM), was crucial in achieving the best possible results. The application of these models yielded the outcomes shown in Tab. 4.3.

The test data's confusion matrix, obtained using the best model (SVM) without a tree structure, is shown in Figure 4.19. The SVM achieves a global accuracy of 61.8%. As anticipated, the accuracy of processing a large dataset containing several categories is relatively low. The lack of accuracy is demonstrated by the inability to accurately characterize the type of a fault that is occurring. On the other hand, the overall test accuracy of the three-based structure can be determined by evaluating the decrease in accuracy for each branch of the tree. As an example, model 1 achieves an accuracy of 93.7%, resulting in a loss of 6.3%. The overall accuracy achieved by applying this method to all branches is 74.5%, which is 12.7% higher than that of a single ML model. Furthermore, the hierarchical arrangement of the tree enables the extraction of key information from each separate branch. If the sole interest lies in distinguishing between a SC and HRC, this can be accomplished with a precision of 86%. Such a result cannot be achieved using a single ML model that has an array of classes. Notably, using just a single ML model is

inadequate in accurately categorizing HRC, as the model mistakenly identifies it as a SC with 2 or 10 turns shorted. This result is justified theoretically since a SC induces both a resistance change and an inductance imbalance. Due to the uncertain nature of the resistance along the path of the SC current, a basic measurement of the phase impedance conducted offline may result in mistakenly classifying a SC as a HRC, therefore overlooking the potential damage that the SC current could cause. However, the suggested technique successfully distinguishes SC and HRC using a KNN algorithm with an accuracy of 86%, as anticipated.

TABLE 4.3: Metrics adopted for evaluating the ML models

Model	Training accuracy	Training 3-fold	Test accuracy	...
RF	100%	$98.6 \pm 2\%$	93.7%	...
KNN	86.6%	$85.2 \pm 2\%$	92.2%	...
$SVM3$	100%	$98.9 \pm 2\%$	97.5%	...
FNN	99.9%	$97 \pm 2\%$	100%	...
$SVM5$	95.1%	$93.7 \pm 2\%$	92.6%	...
$SVM6$	97.7%	$95.4 \pm 2\%$	100%	...

...	Test precision	Test recall	Test AUC	Test F1-score
...	100%	85.1%	95%	91.9%
...	91.8%	96.3%	93.3%	94%
...	100%	96.7%	95.65%	98.32%
...	100%	100%	100%	100%
...	92.6%	100%	100%	96.15%
...	100%	100%	100%	100%

4.4 Conclusions

In this chapter have been presented two ML strategies to diagnose different types of faults, even occurring simultaneously, in a dual-three-phase elctric motor.

A semi-analytical model, based on a preliminary finite-element analysis to estimate the motor inductances, is developed. This model allows to obtain a large amount of data in a brief amount of time, corresponding to both healthy and faulty conditions for different operating points of the electric motor.

The strategy proposed in Sec. 4.2 is a diagnostic method to detect and localize a SC fault using five machine-learning models. Moreover, the proposed strategy distinguishes a SC fault from an unbalance due to an ET.

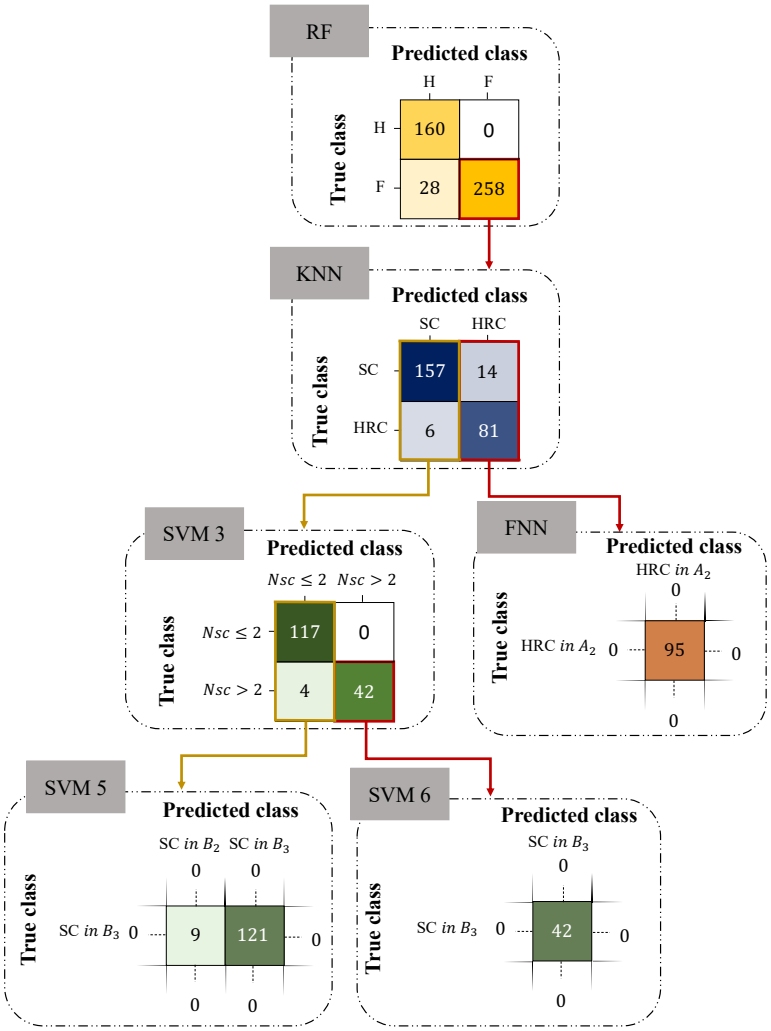

FIGURE 4.18: Confusion matrix results obtained with test data for all the six ML models used.

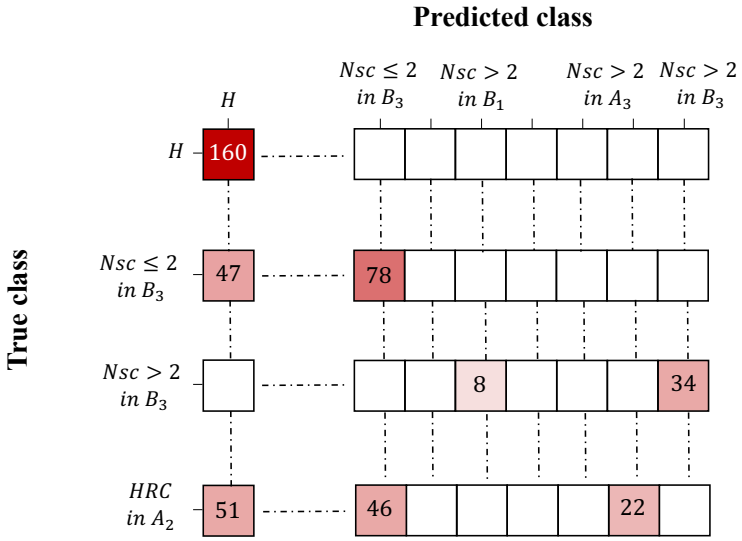

FIGURE 4.19: Confusion matrix for test dataset using a single SVM model for all classes.

Sec. 4.3 presents a ML-based diagnostic method for the diagnostic of two types of stator winding faults that may occur in a dual-three-phase electric motor, i.e., SCs and HRCs. A tree-based structure has been suggested as a means to prevent overfitting and enhance the accuracy

Table 4.4: Motor parameters

Motor data	Values	Units
Rated speed	1500	RPM
Rated torque	25	Nm
Rated current	15	A
Pole pairs, p	2	-
Fundamental harmonic of the magnets flux	0.393	Wb
Magnetic airgap thickness (including magnets)	7	mm
Magnet thickness	5	mm
Number of slots	48	-
Conductors per slot	20	-
Phase resistance, R_s	0.442	Ω
Inductance of the first Clark space, L_1	0.0056	H
Inductance of the fifth Clark space, L_5	0.00081	H
Axial active length	70	mm
Stator inner radius	75	mm

of fault class prediction.

The fault diagnosis often involves the use of measurement sensors, which are known for their expensive cost and additional space requirements. Furthermore, measurement sensors have a maximum measurement accuracy equal to their full scale, so, they might mistakenly confuse a low severity fault with noise. Ultimately, the measurement sensors are unable to detect patterns or correlations among the measured variables. On the contrary, the implementation of ML techniques, such as the two proposed in this Chapter, does not necessitate the utilization of any sensors or measurement device and may be integrated directly into the control system.

Bibliography

[1] J. E. T. Akinsola, "Supervised machine learning algorithms: Classification and comparison," *International Journal of Computer Trends and Technology (IJCTT)*, vol. 48, pp. 128 – 138, 06 2017.

[2] S. Zhao, F. Blaabjerg, and H. Wang, "An overview of artificial intelligence applications for power electronics," *IEEE Transactions on Power Electronics*, vol. 36, no. 4, pp. 4633–4658, 2021.

[3] S. Zhang, O. Wallscheid, and M. Porrmann, "Machine learning for the control and monitoring of electric machine drives: Advances and trends," *IEEE Open Journal of Industry Applications*, vol. 4, pp. 188–214, 2023.

[4] B. D. E. Cherif, M. Chouai, S. Seninete, and A. Bendiabdellah, "Machine-learning-based diagnosis of an inverter-fed induction motor," *IEEE Latin America Transactions*, vol. 20, no. 6, pp. 901–911, 2022.

[5] K.-J. Shih, M.-F. Hsieh, B.-J. Chen, and S.-F. Huang, "Machine learning for inter-turn short-circuit fault diagnosis in permanent magnet synchronous motors," *IEEE Transactions on Magnetics*, vol. 58, no. 8, pp. 1–7, 2022.

[6] M. Z. Ali, M. N. S. K. Shabbir, X. Liang, Y. Zhang, and T. Hu, "Machine learning-based fault diagnosis for single- and multi-faults in induction motors using measured stator currents and vibration signals," *IEEE Transactions on Industry Applications*, vol. 55, no. 3, pp. 2378–2391, 2019.

[7] M. Z. Ali, M. N. S. K. Shabbir, S. M. K. Zaman, and X. Liang, "Single- and multi-fault diagnosis using machine learning for variable frequency drive-fed induction motors," *IEEE Transactions on Industry Applications*, vol. 56, no. 3, pp. 2324–2337, 2020.

[8] I. Martin-Diaz, D. Morinigo-Sotelo, O. Duque-Perez, and R. J. Romero-Troncoso, "An experimental comparative evaluation of machine learning techniques for motor fault diagnosis under various operating conditions," *IEEE Transactions on Industry Applications*, vol. 54, no. 3, pp. 2215–2224, 2018.

[9] Z. Gao, C. Cecati, and S. X. Ding, "A survey of fault diagnosis and fault-tolerant techniques—part i: Fault diagnosis with model-based and signal-based approaches," *IEEE Transactions on Industrial Electronics*, vol. 62, no. 6, pp. 3757–3767, 2015.

[10] M.-P. Hosseini, A. Hosseini, and K. Ahi, "A review on machine learning for eeg signal processing in bioengineering," *IEEE Reviews in Biomedical Engineering*, vol. 14, pp. 204–218, 2021.

[11] D. Dablain, B. Krawczyk, and N. V. Chawla, "Deepsmote: Fusing deep learning and smote for imbalanced data," *IEEE Transactions on Neural Networks and Learning Systems*, vol. 34, no. 9, pp. 6390–6404, 2023.

[12] Y.-S. Jeon and D.-J. Lim, "Psu: Particle stacking undersampling method for highly imbalanced big data," *IEEE Access*, vol. 8, pp. 131 920–131 927, 2020.

[13] H. Liu and L. Yu, "Toward integrating feature selection algorithms for classification and clustering," *IEEE Transactions on Knowledge and Data Engineering*, vol. 17, no. 4, pp. 491–502, 2005.

Chapter 5

Current Ripple in Odd-Phase Inverters

A reduction in the switching ripple of the phase currents has a visible impact on the electric drive. The transition from a sinusoidal AC supply to a PWM supply may increase the losses within the magnetic circuit of electric machines by more than 15% because the current and voltage waveform can be significantly distorted in comparison to the sinusoidal form. This chapter focuses on the modulation strategy with the minimum RMS value of the output current switching ripple for multiphase inverters with an odd number of phases. In addition, the strategy proposed allows to minimize the number of commutations of the power electronic components, hence, decreasing the switching losses.

5.1 Analysis of the Output Current Ripple

Establishing appropriate and adaptable control strategies for N-phase Voltage Source Inverters (VSIs) is crucial to exploit the strengths of N-phase motor drives. Two modulation techniques, Space-Vector Modulation (SVM)[1; 2] and carrier-based Pulse-Width Modulation (PWM) [3–5], have been developed, but they have been demonstrated to be inherently equivalent [6; 7]. Currently, PWM is often preferred owing to its simplicity. Over the years, various efforts have been made to enhance the performance of multiphase drives in terms of efficiency, quality of output voltages and input currents, common-mode disturbances, operating range, and

flexibility [8–12]. A frequent subject concerning power converters is the quality of the output current, as it affects motor behavior.

5.1.1 Fundamentals of Carrier-Based PWM for Multiphase Inverters

A schematic of a multiphase inverter is shown in Fig. 5.1.

According to the VSD described deeply in Sec. 2.2, given an odd set of N real quantities $x_1, x_2, \ldots, x_N$, the following linear transformations define a new set of variables:

$$\begin{aligned} x_0 &= \frac{1}{N}\sum_{k=1}^{N} x_k \\ \bar{x}_\rho &= \frac{2}{N}\sum_{k=1}^{N} x_k \bar{\alpha}_k^\rho \quad \rho = 1, 3, ..., N-2 \end{aligned} \tag{5.1}$$

where

$$\bar{\alpha}_k = e^{j\frac{2\pi}{N}(k-1)}. \tag{5.2}$$

The real quantity x_0 is the zero-sequence component, whereas $\bar{x}_1, \bar{x}_3, ..., \bar{x}_{N-2}$ are complex quantities called "space vectors." If $m_1, m_2, ..., m_N$ are the command signals of the inverter legs, with values of 0 or 1, and E_{dc} is the dc-link voltage, the instantaneous output voltage vectors are as follows:

$$\bar{v}_\rho = \frac{2}{N} E_{dc} \sum_{k=1}^{N} m_k \bar{\alpha}_k^\rho \quad \rho = 1, 3, ..., N-2. \tag{5.3}$$

Given the desired average voltage vectors $\bar{v}_{1,ref}, \bar{v}_{3,ref}, ..., \bar{v}_{N-2,ref}$ over a switching period, solving the modulation problem of a multiphase inverter requires finding the N command signals of the inverter legs. Cosidering the principles of PWM, the command signals can be generated

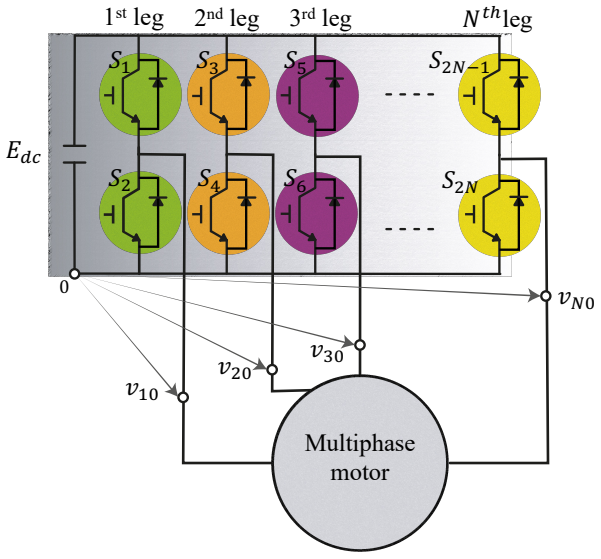

FIGURE 5.1: Multiphase inverter supplying a multiphase machine.

by comparing N modulating signals $m_{1,ref}, m_{2,ref}, ..., m_{N,ref}$ with a triangular carrier. The k-th modulating signal $m_{k,ref}$ can be calculated by inverting (5.1):

$$\begin{aligned} m_{k,ref} &= m_{0,ref} + n_{k,ref} \\ n_{k,ref} &= \frac{1}{E_{dc}} \sum_{k=1}^{N-2} \bar{v}_{\rho,ref} \cdot \bar{\alpha}_k^{\rho} \quad k = 1, 2, ..., N \end{aligned} \tag{5.4}$$

where "$\cdot$" is the dot operator, defined as the real part of the product of the first operand multiplied by the complex conjugate of the second operand, and $m_{0,ref}$ is the zero-sequence component of the modulating signals.

The zero-sequence component $m_{0,ref}$ is a degree of freedom that can be chosen to improve the PWM performance. To prevent overmodulation, the modulating signals must remain within the following range:

$$m_{k,ref} \in [0, 1] \quad k = 1, 2, ..., N. \tag{5.5}$$

Tab. 5.1 lists some noteworthy values of $m_{0,ref}$, which correspond to well-known modulation strategies for multiphase inverters. In Tab. 5.1, the quantity $\bar{m}_{\rho,ref}$ is defined as the ratio of $\bar{v}_{\rho,ref}$ and E_{dc}.

Constraints (5.5) result in lower and upper limits for the magnitude of the modulating signals, which define the output voltage range of the converter [13; 14].

As can be seen in (5.4), the modulation process for multiphase inverters is similar to that for three-phase inverters, i.e., the modulating signals are compared with the carrier signal to generate the gate control signals over the switching period T_{sw}, as shown in Fig. 5.2. However, the calculation of the modulating signals may be more complex, as it depends on the reference voltage vectors in all subspaces according to the VSD. If the reference voltage vectors in the harmonic subspaces are zero, the control system complexity does not change significantly. On the other hand, if the control system aims to manage the extra spatial harmonic components

TABLE 5.1: Value of $m_{0,ref}$ for different PWM modulation strategies.

Name	$m_{0,ref}$
Sinusoidal (S)	$m_{0,S} = \frac{1}{2}$
Discontinuous (DMIN)	$m_{0,DMIN} = -\min_{k=1,...,N} \left(\sum_{\rho} \bar{m}_{\rho,ref} \cdot \bar{\alpha}_k^{\rho} \right)$
Discontinuous (DMAX)	$m_{0,DMAX} = 1 - \max_{k=1,...,N} \left(\sum_{\rho} \bar{m}_{\rho,ref} \cdot \bar{\alpha}_k^{\rho} \right)$
Space Vector (SVPWM)	$m_{0,SV} = \frac{1}{2}(m_{0,DMIN} + m_{0,DMAX})$

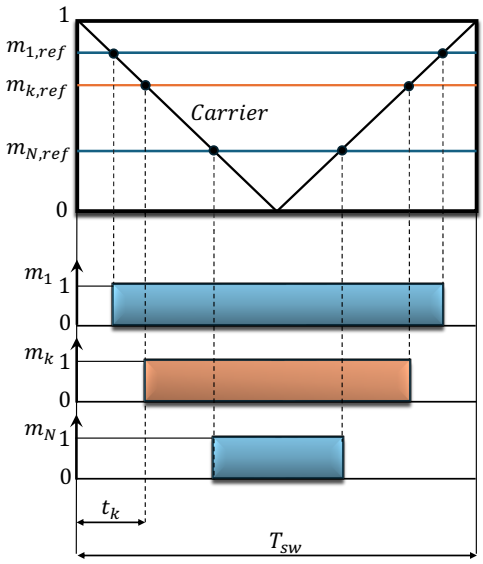

FIGURE 5.2: Generation of the switching signals in a N-phase inverter according to the carrier-based PWM.

of the magnetic field, the calculation of the reference voltage vectors may become challenging, depending on the specific feature that the control system is targeting, such as high-torque density, fault-tolerant operation, and online parameter estimation.

5.1.2 Modulation Strategy with Minimum RMS Value of the Output Current Ripple

The output current vectors $\bar{i}_1, \bar{i}_3, ..., \bar{i}_{N-2}$ deviate from their desired trajectories owing to the discrepancy between the actual voltage vectors $\bar{v}_1(t), \bar{v}_3(t), ..., \bar{v}_{N-2}(t)$ and the desired values $\bar{v}_{1,ref}, \bar{v}_{3,ref}, ..., \bar{v}_{N-2,ref}$. However, the switching pattern of the actual voltage vectors is arranged to match the desired average values over the switching period.

The deviation $\Delta\bar{i}_\rho$ of each current vector from its average value over a switching period T_{sw} is governed by the following approximated differential equation, which neglects the effect of the load resistance in high-frequency transients:

$$L_\rho \frac{d\Delta\bar{i}_\rho}{dt} = \bar{v}_\rho - \bar{v}_{\rho,ref} \tag{5.6}$$

where $\bar{v}_\rho$ and L_ρ ($\rho = 1, 3, ..., N-2$) are the actual voltage space vector and the high-frequency equivalent load inductance in subspace ρ. The average deviations of the currents and voltages from their desired values can be assumed zero over T_{sw}, so the following constraints are satisfied:

$$\int_0^{T_{sw}} \Delta\bar{i}_\rho \, dt = 0 \tag{5.7}$$

$$\int_0^{T_{sw}} (\bar{v}_\rho - \bar{v}_{ref,\rho})\, dt = 0. \tag{5.8}$$

It is assumed that the modulation strategy generates a symmetric switching pattern with respect to the midpoint of the switching period. This property implies that the sequence of transitions from one inverter configuration to the next in the first half period is repeated backward in the second half. Fig. 5.3 shows an example of the trajectory of the current ripple over a switching period for a five-phase inverter. The deviation $\Delta\bar{i}_\rho$ is zero at $t = 0$, $t = T_{sw}/2$, and $t = T_{sw}$. Each color vector corresponds to a specific inverter configuration. The trajectory of $\Delta\bar{i}_\rho$ is symmetric with respect to the origin of the reference frame, so the analysis of the current ripple can be limited to half of the switching period, T (i.e., $T = \frac{T_{sw}}{2}$).

Furthermore, the current ripple $\Delta\bar{i}_\rho$ can be expressed as the sum of its average value $\bar{i}^0_{rip,0}$ over the half period T and the zero-mean deviation $\bar{i}_{rip}$, as stated below:

$$\Delta\bar{i}_\rho = \bar{i}^0_{rip,\rho} + \bar{i}_{rip,\rho} \tag{5.9}$$

$$\bar{i}^0_{rip,\rho} = \frac{1}{T}\int_0^T \Delta\bar{i}_\rho dt. \tag{5.10}$$

The total RMS value of the current ripple, extended to all phases and over a switching period T_{sw}, is as follows:

$$T_{sw}\Delta I^2_{RMS} = \sum_{k=1}^{N}\int_0^{T_{sw}} \Delta i_k^2 dt = \frac{N}{2}\sum_{\rho=1,3,\ldots}^{N-2}\int_0^{T_{sw}} |\Delta\bar{i}_\rho|^2 dt \tag{5.11}$$

where Δi_k is the deviation in the k-th load current. Due to the symmetric trajectory of the current ripple, the integrals in (5.11) can be rewritten as integrals over a half period. In addition, by combining (5.9) and (5.11), the following result can be obtained:

$$T_{sw}\Delta I^2_{RMS} = N\sum_{\rho=1,3,\ldots}^{N-2}\left(T|\bar{i}^0_{rip,\rho}|^2 + \int_0^T |\bar{i}_{rip,\rho}|^2 dt\right). \tag{5.12}$$

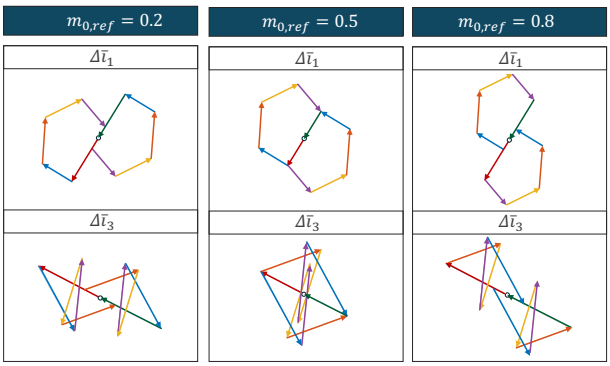

FIGURE 5.3: Deviation of the current space vectors of a five-phase inverter from their ideal trajectories in subspaces 1 and 3 over a switching period for different values of $m_{0,ref}$.

It can be demonstrated that the quantity $\int_0^T |\bar{i}_{rip,\rho}|^2 dt$, which appears in (5.12), is constant and independent of $m_{0,ref}$, similar to the calculation of the center of mass of a plane curve. This result can be readily understood by examining Fig. 5.3, which shows the trajectories of $\Delta\bar{i}_1$ and $\Delta\bar{i}_3$ over a switching period for three increasing values of $m_{0,ref}$ in a five-phase inverter. As can be seen, each curve is composed of two parts, symmetrically disposed with respect to the origin, which rigidly translate without changing their shape as long as $m_{0,ref}$ increases. Consequently, to reduce the RMS value of the current ripple, it is necessary to minimize the quantity $\sum_{\rho=1,3,\ldots}^{N-2} |\bar{i}^0_{rip,\rho}|^2$, the only one sensitive to $m_{0,ref}$ in (5.12).

The derivative of (5.12) with respect to $m_{0,ref}$ is expressed as follows:

$$\frac{d(T_{sw}\Delta I^2_{RMS})}{dm_{0,ref}} = NT \sum_{\rho=1,3,\ldots}^{N-2} 2\bar{i}^0_{rip,\rho} \cdot \frac{d\bar{i}^0_{rip,\rho}}{dm_{0,ref}}. \tag{5.13}$$

To evaluate (5.13) and find the expression of $\bar{i}^0_{rip,\rho}$, two steps are necessary. The initial step is to determine $\Delta\bar{i}_\rho$ by integrating (5.6).

$$\Delta\bar{i}_\rho(t) = \frac{1}{L_\rho}\int_0^t \Big(\bar{v}_\rho(\tau) - \bar{v}_{\rho,ref}\Big)d\tau. \tag{5.14}$$

Then, combining (5.14), (5.10) and (5.3) yields the following expression for $\bar{i}^0_{rip,\rho}$:

$$\bar{i}^0_{rip,\rho} = \frac{1}{T}\frac{2}{N}\frac{E_{dc}}{L_\rho}\sum_{k=1}^{N}\left[\int_0^T\Big(\int_0^t m_k\bar{\alpha}^\rho_k d\tau\Big)dt\right] - \frac{T}{2}\frac{\bar{v}_{\rho,ref}}{L_\rho}. \tag{5.15}$$

Equation (5.15) can be simplified by noting from Fig. 5.2 that the following equality holds:

$$\int_0^t m_k d\tau = \begin{cases} 0 \quad if \quad t < t_k \\ t - t_k \quad otherwise \end{cases} \tag{5.16}$$

where t_k is the transition time of m_k from 0 to 1.

Substituting (5.16) into (5.15) gives the following result:

$$\bar{i}^0_{rip,\rho} = \frac{T}{2L_\rho}\left[\frac{2}{N}E_{dc}\sum_{k=1}^{N}\Big(1 - \frac{t_k}{T}\Big)^2\bar{\alpha}^\rho_k - \bar{v}_{\rho,ref}\right]. \tag{5.17}$$

Fig. 5.2 shows that the quantity $1 - \frac{t_k}{T}$ is equal to $m_{k,ref}$, so (5.17) can be rewritten in a more compact form:

$$\bar{i}^0_{rip,\rho} = \frac{T}{2L_\rho}\left[\frac{2}{N}E_{dc}\sum_{k=1}^{N} m^2_{k,ref}\bar{\alpha}^\rho_k - \bar{v}_{\rho,ref}\right]. \tag{5.18}$$

The leg modulating signals can be expressed as functions of the zero-sequence component $m_{0,ref}$ through (5.4). Consequently, (5.18) becomes as follows:

$$\bar{i}^0_{rip,\rho} = \frac{T}{2L_\rho}\left[\frac{2}{N}E_{dc}\sum_{k=1}^{N} n^2_{k,ref}\bar{\alpha}^\rho_k + (2m_{0,ref}-1)\bar{v}_{ref,\rho}\right]. \tag{5.19}$$

After some calculations, (5.13) turns out to be a linear function of $m_{0,ref}$:

$$\frac{d(T_{sw}\Delta I^2_{RMS})}{dm_{0,ref}} = A(2m_{0,ref}-1)+B \tag{5.20}$$

where

$$\begin{aligned} A &= 2NT^2 \sum_{\rho=1,3,...}^{N-2} \frac{|\bar{v}_{\rho,ref}|^2}{L^2_\rho} \\ B &= 2NT^2 \sum_{\rho=1,3,...}^{N-2} \left(\frac{2}{N}\frac{E_{dc}}{L^2_\rho}\sum_{k=1}^{N} n^2_{k,ref}\bar{\alpha}^\rho_k \cdot \bar{v}_{\rho,ref}\right). \end{aligned} \tag{5.21}$$

To find the value of $m_{0,ref}$ corresponding to the minimum ripple, the derivative must be set equal to zero:

$$m_{0,OPT} = \frac{1}{2}\left(1 - \frac{\sum_{\rho=1,3,...}^{N-2}\frac{2}{N}\sum_{k=1}^{N} n^2_{k,ref}\bar{\alpha}^\rho_k \cdot \frac{\bar{m}_{\rho,ref}}{L^2_\rho}}{\sum_{\rho=1,3,...}^{N-2}\frac{|\bar{m}_{\rho,ref}|^2}{L^2_\rho}}\right). \tag{5.22}$$

The value of $m_{0,OPT}$ resulting from (5.22) corresponds to a minimum of the current ripple because the second derivative, obtained by deriving (5.20) once again, equals A, which is positive.

The value of $m_{0,OPT}$ in (5.22) is valid if the resulting modulating signals satisfy the constraints (5.5); otherwise, $m_{0,OPT}$ must be constrained between $m_{0,DMIN}$ and $m_{0,DMAX}$.

Equation (5.22) is written in a mixed form, i.e., it combines the dimensionless reference voltage vectors $\bar{m}_{1,ref}, \bar{m}_{3,ref}, ..., \bar{m}_{N-2,ref}$, sometimes called duty-cycle space vectors, and the scalar signals $n_{1,ref}, n_{2,ref}, ..., n_{N,ref}$. The expressions of (5.22) as functions of the signals $n_{1,ref}, n_{2,ref}, ..., n_{N,ref}$ or the dimensionless voltage vectors $\bar{m}_{1,ref}, \bar{m}_{3,ref}, ..., \bar{m}_{N-2,ref}$ are derived in the next sections.

5.1.3 Expression of $m_{0,opt}$ as a Function of the Modulating Signals

Let us define the new variables $l_1, l_2, ..., l_N$ as follows:

$$l_k = \sum_{\rho=1,3,...}^{N-2} \frac{\bar{m}_{\rho,ref}}{L^2_\rho} \cdot \bar{\alpha}^\rho_k. \tag{5.23}$$

Then, (5.22) becomes:

$$m_{0,OPT} = \frac{1}{2}\left(1 - \frac{\sum_{k=1}^{N} n^2_{k,ref} l_k}{\sum_{k=1}^{N} n_{k,ref} l_k}\right). \tag{5.24}$$

In an electric machine, the subspace inductances are different from one another. However, if the load is composed of magnetically independent phases, all inductances may be equal to the same value L. Then l_k is equal to $n_{k,ref}/L^2$ for any k, and (5.24) takes a simpler form:

$$m_{0,OPT} = \frac{1}{2}\left(1 - \frac{\sum_{k=1}^{N} n_{k,ref}^3}{\sum_{k=1}^{N} n_{k,ref}^2}\right). \tag{5.25}$$

In conclusion, $m_{0,OPT}$ is independent of the load parameters if $N = 3$ or if all the subspace inductances are equal.

5.1.4 Expression of $m_{0,opt}$ as a Function of the Dimensionless Voltage Vectors

After tedious calculations, a new form for (5.22) can be found using (5.4):

$$m_{0,OPT} = \frac{1}{2}\left(1 - \frac{\sum_{\rho,\sigma,\tau=1,3,\ldots}^{N-2} \frac{1}{L_\rho^2}\Re e\{\bar{f}(\rho,\sigma,\tau)\}}{2\sum_{\rho=1,3,\ldots}^{N-2} \frac{1}{L_\rho^2}|\bar{m}_{\rho,ref}|^2}\right). \tag{5.26}$$

In (5.26), $\bar{f}$ is a complex function defined as follows:

$$\begin{aligned}\bar{f}(\rho,\sigma,\tau) = {} & \bar{m}_{\rho,ref}\bar{m}_{\sigma,ref}\bar{m}_{\tau,ref}\delta(\rho+\sigma+\tau) \\ & +\bar{m}^*_{\rho,ref}\bar{m}_{\sigma,ref}\bar{m}_{\tau,ref}\delta(-\rho+\sigma+\tau) \\ & +\bar{m}_{\rho,ref}\bar{m}^*_{\sigma,ref}\bar{m}_{\tau,ref}\delta(\rho-\sigma+\tau) \\ & +\bar{m}_{\rho,ref}\bar{m}_{\sigma,ref}\bar{m}^*_{\tau,ref}\delta(\rho+\sigma-\tau)\end{aligned} \tag{5.27}$$

where "$*$" is the complex conjugate operator, and the binary operator δ is 1 only if its operand is a multiple of N:

$$\delta(n) = \begin{cases} 1, & \text{if } n \bmod N = 0, \\ 0, & \text{otherwise.} \end{cases} \tag{5.28}$$

The expression of $m_{0,OPT}$ resulting from (5.26) for three-phase inverters ($N = 3$) is independent of the load inductance:

$$m_{0,OPT}^{(3)} = \frac{1}{2}\left(1 - \frac{\Re e\{\bar{m}_{1,ref}^3\}}{2|\bar{m}_{1,ref}|^2}\right). \tag{5.29}$$

If $\bar{m}_{1,ref}$ is written in polar form as $M_1 e^{j\theta}$, (5.29) becomes as follows:

$$m_{0,OPT}^{(3)} = \frac{1}{2} - \frac{1}{4}M_1\cos 3\theta. \tag{5.30}$$

This result was originally presented by S. R. Bowes in 1985 [15] and has been known for approximately 40 years.

The expression of $m_{0,OPT}$ for the case $N = 5$ is as follows:

$$m_{0,OPT}^{(5)} = \frac{1}{2}\left[1 - \frac{\Re e\{\bar{f}_1^{(5)} + \bar{f}_2^{(5)}\}}{2(\frac{|\bar{m}_{1,ref}|^2}{L_1^2} + \frac{|\bar{m}_{3,ref}|^2}{L_3^2})}\right] \tag{5.31}$$

where the functions $\bar{f}_1^{(5)}$ and $\bar{f}_2^{(5)}$ are defined below:

$$\begin{aligned} \bar{f}_1^{(5)} &= \bar{m}_{1,ref}^2 \bar{m}_{3,ref}\left(\frac{2}{L_1^2} + \frac{1}{L_3^2}\right) \\ \bar{f}_2^{(5)} &= \bar{m}_{1,ref}^* \bar{m}_{3,ref}^2\left(\frac{1}{L_1^2} + \frac{2}{L_3^2}\right). \end{aligned} \tag{5.32}$$

This result aligns with the findings presented in a paper by Casadei et al. in 2011 [16], where $m_{0,OPT}$ was obtained through complex analytical calculations.

Finally, the expression of $m_{0,OPT}$ for the cases $N = 7$ is as follows:

$$m_{0,OPT}^{(7)} = \frac{1}{2}\left[1 - \frac{\Re e\{\bar{f}_1^{(7)} + \bar{f}_2^{(7)} + \bar{f}_3^{(7)} + \bar{f}_4^{(7)}\}}{2(\frac{|\bar{m}_{1,ref}|^2}{L_1^2} + \frac{|\bar{m}_{3,ref}|^2}{L_3^2} + \frac{|\bar{m}_{5,ref}|^2}{L_5^2})}\right] \tag{5.33}$$

where the functions $\bar{f}_1^{(7)}$, $\bar{f}_2^{(7)}$, ... , $\bar{f}_4^{(7)}$ are defined hereafter:

$$\begin{aligned} \bar{f}_1^{(7)} &= \bar{m}_{1,ref}\bar{m}_{3,ref}^2\left(\frac{1}{L_1^2} + \frac{2}{L_3^2}\right) \\ \bar{f}_2^{(7)} &= \bar{m}_{1,ref}^2\bar{m}_{5,ref}\left(\frac{2}{L_1^2} + \frac{1}{L_5^2}\right) \\ \bar{f}_3^{(7)} &= \bar{m}_{3,ref}^*\bar{m}_{5,ref}^2\left(\frac{1}{L_3^2} + \frac{2}{L_5^2}\right) \\ \bar{f}_4^{(7)} &= \bar{m}_{1,ref}^*\bar{m}_{3,ref}\bar{m}_{5,ref}\left(\frac{2}{L_1^2} + \frac{2}{L_3^2} + \frac{2}{L_5^2}\right). \end{aligned} \tag{5.34}$$

The previous results unequivocally demonstrate that sinusoidal PWM, which maintains $m_{0,ref}$ equal to 1/2, provides the minimum ripple of the output currents in multiphase machines whenever only one harmonic sub-space is excited.

5.2 Simulation Results

5.2.1 General Results

A series of numerical simulations was conducted to assess the effectiveness of the developed strategy in comparison with SPWM and SVPWM, which are commonly used when a low output current ripple is desired. Two multi-phase induction machine models with five and seven phases,

respectively, were developed in Matlab/Simulink to emulate the behavior of the prototypes utilized in the experimental tests. The parameters of the five-phase machine are presented in Tab. 5.2, while those of the seven-phase machine are reported in Tab. 5.3.

The inductance L_ρ that limits the current ripple in subspace ρ is approximately equal to the leakage inductance, which can be calculated as follows:

$$L_\rho = L_{S\rho} - \frac{L_{M\rho}^2}{L_{R\rho}}. \tag{5.35}$$

The numerical simulations assume that both machines operate in a steady state. Each dimensionless voltage space vector $\bar{m}_{\rho,ref}$ rotates with a constant angular frequency $\rho\omega_1$ and

TABLE 5.2: Parameters of the five-phase wound-rotor induction machine.

Rated power	3.5 kW
Rated speed	1500 RPM
Pole number	6
Self inductances	$L_{S1} = 0.411\ H$, $L_{R1} = 0.939\ H$ $L_{S3} = 0.068\ H$, $L_{R3} = 0.158\ H$
Mutual inductances	$L_{M1} = 0.555\ H$ $L_{M3} = 0.053\ H$
Stator resistances	$R_{S1} = R_{S3} = 1.7\ \Omega$
Rotor resistances	$R_{R1} = R_{R3} = 2.03\ \Omega$

TABLE 5.3: Parameters of the seven-phase induction machine.

Rated power	3.5 kW
Rated speed	1450 RPM
Pole number	4
Self inductances	$L_{S1}, L_{R1} = 0.1798\ H$ $L_{S3}, L_{R3} = 0.0244\ H$ $L_{S5}, L_{R5} = 0.0120\ H$
Mutual inductances	$L_{M1} = 0.1748\ H$ $L_{M3} = 0.0194\ H$ $L_{M5} = 0.070\ H$
Stator resistances	$R_{S1} = R_{S3} = R_{S5} = 1.1\ \Omega$
Rotor resistances	$R_{R1} = 1.01\ \Omega$ $R_{R3} = 0.8\ \Omega$ $R_{R5} = 0.6\ \Omega$

constant magnitude M_ρ, as follows:

$$\bar{m}_{\rho,ref} = M_\rho e^{j\rho\omega_1 t}. \tag{5.36}$$

where ω_1 is the fundamental frequency of the output voltage.

The average RMS value of the current ripple is calculated over a fundamental period $\frac{2\pi}{\omega_1}$ resulting from the contributions of all the switching periods.

$$\Delta I^2_{RMS,avg} = \frac{\omega_1}{2\pi} \int_0^{\frac{2\pi}{\omega_1}} \Delta I^2_{RMS} dt \tag{5.37}$$

Equation (5.37) is calculated for all points of the linear-modulation domain [13; 14].

The optimal modulation, SVPWM and SPWM have been compared for the five-phase and seven-phase inverters for three different switching frequencies (3, 5 and 8 kHz) in a range of operational scenarios. The simulation results are presented in tabular form. Tabs. 5.4 and 5.5 report the values of the modulation indexes, the RMS value squared of the current ripple for all strategies, and the ratio squared of the RMS value of the current ripple for SVPWM or SPWM over the RMS value of the current ripple for the optimal modulation. In all simulations, these ratios are greater than or equal to 1, indicating that the optimal modulation generates the best current quality.

Numerical simulations have been conducted to replicate the experimental results as closely as possible.

- In some instances, the modulation index is nearly, but not precisely, equal to the maximum value (e.g., 0.47 instead of 0.5). This discrepancy arises due to two factors. First, the inverter dead times [1] preclude the theoretical limit from being reached without introducing distortions in the voltage due to transient overmodulation conditions. The second reason is related to potential fluctuations in the output voltage. As the control system assigns the reference output voltage depending on the operating conditions and the input DC-link voltage, the modulation index may exhibit slight fluctuations. A small margin ensures that the inverter does not enter the overmodulation region, which would cause distortions not considered in the presented theory, which focuses on the linear modulation region.

- Tabs. 5.4 and 5.5 demonstrate that, as the switching frequency increases, the optimal strategy remains the most effective, yet the ripple tends to decrease in inverse proportion to the switching frequency. In the experimental tests, the increase in switching frequency may potentially introduce spurious phenomena, such as inverter dead times and core losses,

[1] Dead- time is used for PWM-controlled inverter control to avoid "short through" of high-side and low-side power devices.

TABLE 5.4: Simulation results for the five-phase induction motor for three different switching frequencies.

Five-phase inverter																	
Test	M_1	M_3	$\Delta\bar{I}^2_{RMS,avg,OPT}$			$\Delta\bar{I}^2_{RMS,avg,SPWM}$			$\Delta\bar{I}^2_{RMS,avg,SVPWM}$			$\frac{\Delta\bar{I}^2_{RMS,avg,SPWM}}{\Delta\bar{I}^2_{RMS,avg,OPT}}$			$\frac{\Delta\bar{I}^2_{RMS,avg,SVPWM}}{\Delta\bar{I}^2_{RMS,avg,OPT}}$		
			3 kHz	5 kHz	8 kHz	3 kHz	5 kHz	8 kHz	3 kHz	5 kHz	8 kHz	3 kHz	5 kHz	8 kHz	3 kHz	5 kHz	8 kHz
P_1	0.47	0	0.0439	0.0369	0.0266	0.0439	0.0360	0.0266	0.0449	0.0374	0.0270	1	1	1	1.0227	1.0129	1.0167
P_3	0	0.47	0.0442	0.0370	0.0268	0.0442	0.0370	0.0268	0.0456	0.0374	0.0272	1	1	1	1.0235	1.0124	1.0162
P_{13}	0.32	0.17	0.0374	0.0323	0.0232	0.0426	0.0375	0.0272	0.0384	0.0328	0.0239	1.1410	1.1615	1.1818	1.0288	1.0149	1.057

TABLE 5.5: Simulation results for the seven-phase induction motor for three different switching frequencies.

Seven-phase inverter																		
Test	M_1	M_3	M_5	$\Delta\bar{I}^2_{RMS,avg,OPT}$			$\Delta\bar{I}^2_{RMS,avg,SPWM}$			$\Delta\bar{I}^2_{RMS,avg,SVPWM}$			$\frac{\Delta\bar{I}^2_{RMS,avg,SPWM}}{\Delta\bar{I}^2_{RMS,avg,OPT}}$			$\frac{\Delta\bar{I}^2_{RMS,avg,SVPWM}}{\Delta\bar{I}^2_{RMS,avg,OPT}}$		
				3 kHz	5 kHz	8 kHz	3 kHz	5 kHz	8 kHz	3 kHz	5 kHz	8 kHz	3 kHz	5 kHz	8 kHz	3 kHz	5 kHz	8 kHz
P_1	0.3	0	0	0.04001	0.0240	0.0163	0.04001	0.0240	0.01630	0.0399	0.02410	0.01641	1	1	1	1.0098	1.0036	1.0019
P_{13}	0.1	0.25	0	0.03756	0.02281	0.0155	0.03789	0.02341	0.01610	0.03763	0.02275	0.0156	1.0091	1.0263	1.0358	1.0019	1.0015	1.0031
P_{15}	0.27	0	0.12	0.03855	0.02341	0.01650	0.04029	0.02490	0.0173	0.03861	0.02347	0.01654	1.0452	1.0641	1.0502	1.0017	1.0029	1.0052
P_{135}	0.15	0.15	0.12	0.03143	0.02030	0.0140	0.03664	0.02379	0.0170	0.03146	0.02381	0.0141	1.1671	1.1724	1.2164	1.0012	1.0014	1.0062
P_{35}	0	0.15	0.15	0.03332	0.01951	0.01318	0.03357	0.01989	0.01349	0.03342	0.01958	0.01319	1.0078	1.0191	1.0237	1.0031	1.0032	1.0008

which could affect the measurement accuracy. To mitigate these issues, a frequency of 3 kHz is employed in the experimental tests.

Consequently, the analysis of the simulation results continues in Sections 5.2.2 and 5.2.3, respectively, with reference only to the switching frequency of 3 kHz.

5.2.2 Five-Phase Inverter

Fig. 5.4(a) shows the ratio of the RMS values of the current ripple with SVPWM and the optimal modulation resulting from Tab. 5.4 when the switching frequency is 3 kHz (blue columns). This quantity is always greater than 1, meaning the current ripple generated by the optimal strategy is lower. In particular, the proposed strategy performs better in two regions, i.e., for values of M_3 around 0.525, and when M_1 is slightly greater than M_3. In the latter situation, SVPWM generates a higher current ripple than the optimal strategy by 4.5%. When M_1 is close to 0.525, the current ripple is the same for both strategies.

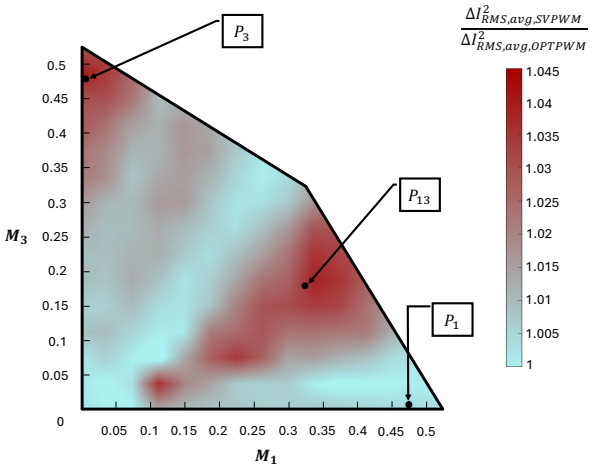

(a)

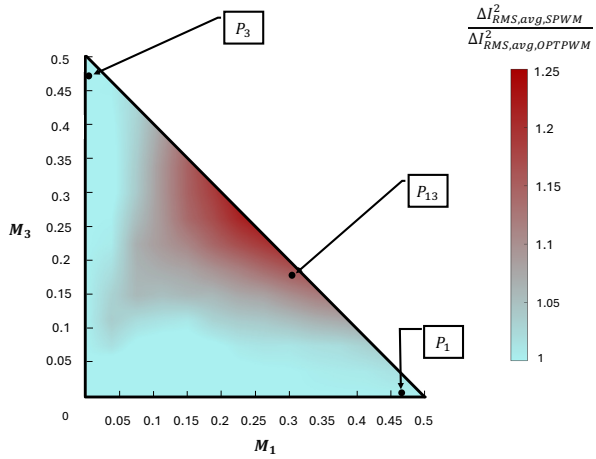

(b)

FIGURE 5.4: Performance of the optimal modulation in a five-phase inverter. a) Ratio between the RMS value of the current ripple with SVPWM and the optimal modulation. b) Ratio between the RMS value of the current ripple with SPWM and the optimal modulation.

Fig. 5.4(b) compares the current ripples resulting from SPWM and the optimal modulation. SPWM generates a current ripple that is 25% higher when M_1 and M_3 tend to coincide.

Fig. 5.5 shows that the optimal strategy is more efficient than SVPWM near the boundary of the linear modulation region. Compared to the optimal modulation, SVPWM causes a number of commutations (N_{sw}) that can be 25% greater when M_1 and M_3 are close to the domain boundary. This result is due to a decrease in the number of commutations of the optimal strategy when $m_{0,OPT}$ is saturated by the lower bound $m_{0,DMIN}$ or the upper bound $m_{0,DMAX}$.

Fig. 5.6 illustrates this phenomenon. The waveform of $m_{0,OPT}$ is shown when M_1 is 0.4, M_3 is 0.2. It turns out that $m_{0,OPT}$ becomes alternately equal to $m_{0,DMAX}$ or $m_{0,DMIN}$, so only four legs of the inverter out of five do switch.

Conversely, SPWM and the optimal modulation exhibit the same number of commutations

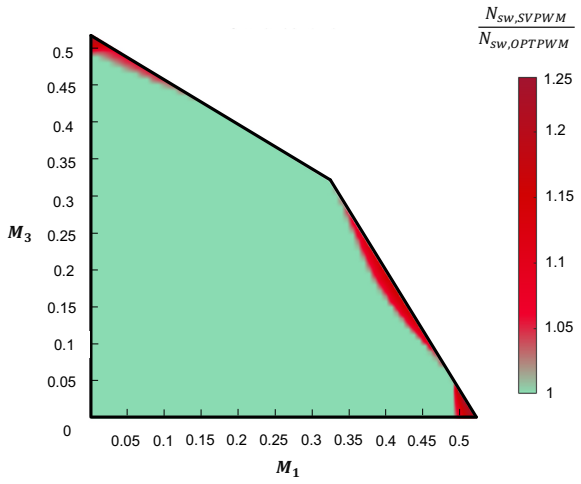

FIGURE 5.5: Ratio among the numbers of commutations obtained with SVPWM and the optimal modulation for a five-phase inverter.

in the shared part of the linear modulation range. However, the achievable voltage range of the optimal modulation is wider and is equal to that of SVPWM [13; 14].

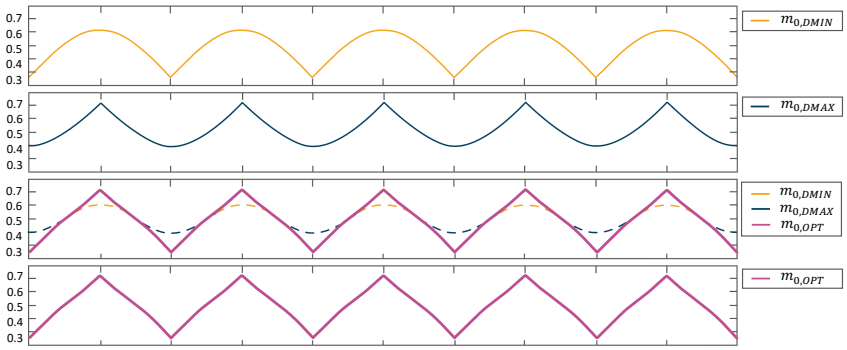

FIGURE 5.6: Waveform of $m_{0,OPT}$ clamped to $m_{0,DMIN}$ or $m_{0,DMAX}$ for $M_1 = 0.4$ and $M_3 = 0.2$. The horizontal scale for ωt is 36°/div.

5.2.3 Seven-Phase Inverter

The 3D plots in Figs. 5.7a and 5.7b show the ratio of the RMS value of the current ripple caused by SVPWM or SPWM and the optimal modulation for a seven-phase induction motor drive resulting from Tab. 5.5 when the switching frequency is 3 kHz (blue columns). The representation is semi-transparent and qualitatively depicts the behavior of the optimal modulation strategy within the linear modulation domain. Fig. 5.7(a) shows that the RMS value of the current ripple generated by SVPWM is up to 2% higher than that of the optimal strategy in the center of the linear modulation region ($M_1 \simeq M_3 \simeq M_5$) or when one of the three dimensionless voltages is near zero.

Fig. 5.7(b) shows a similar behavior for SPWM. Compared to the optimal strategy, SPWM generates a current ripple that is 25% higher when M_1, M_3, and M_5 are in close proximity to one another or when one of them is zero and the other ones tend to coincide.

Finally, it is noteworthy that the proposed method reduces the number of commutations by up to 14% compared to SVPWM when $M_1 \simeq M_3 \simeq M_5$ and at some points on the boundary close to the overmodulation region as shown in Fig. 5.8. Conversely, the optimal modulation and SPWM have the same number of commutations in the shared part of the voltage range. However, the SPWM voltage range is smaller.

5.3 Experimental Results

Some experimental tests were carried out to validate the theoretical analysis. Fig. 5.9 depicts the entire experimental setup, including the five- and seven-phase induction machines. A DC generator operates as a load mechanically coupled to the machines. The machine parameters are the same as those used for the simulation results and reported in Tabs. 5.2 and 5.3. The control system is developed through a dSPACE MicroLabBox platform, which controls a multiphase inverter with a switching frequency of 3 kHz, configured to supply a multiphase motor with a maximum of twelve phases. The inverter power stage consists of two Infineon F12-25R12KT4G power modules, equipped with 1200 V – 25 A class IGBTs and diodes. An Elektro-Automatik power supply (EA-PS 9500 - 20) keeps the DC-link voltage at about 200 V and 250 V respectively for the five- and seven-phase configurations. Two different DC voltages are necessary due to the different characteristics of the two machines.

The current ripple is approximately inversely proportional to the switching frequency and machine high-frequency inductance. However, the machine parameters are contingent upon the specific switching frequency, machine type, and rotor slots. Furthermore, as the frequency varies, other phenomena may occur, which are caused by losses in the machine iron core due to eddy currents and hysteresis (loss phenomena in machines with surface PMs can also occur as a result of induced currents within the magnets). These problems are intricate and complex to address. The use of a constant frequency of 3 kHz in experimental tests has been dictated by these factors:

- The duration of the switching period should be sufficiently long to allow for accurate measurement of the current ripple and to minimize the impact of the inverter dead times .
- Simultaneously, the switching period should not be too long since this would result in the linearization approximation of the equations becoming invalid.
- The impact of high-frequency losses on parasitic phenomena should be negligible.

The use of induction machines for the experimental tests is not accidental. In PM machines, permanent magnets generate high-order harmonic back-electromotive forces that result in the

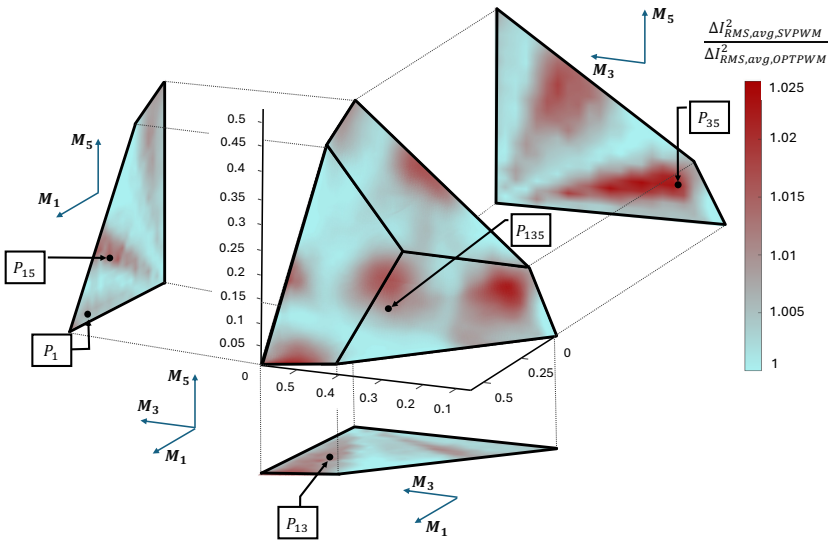

(a)

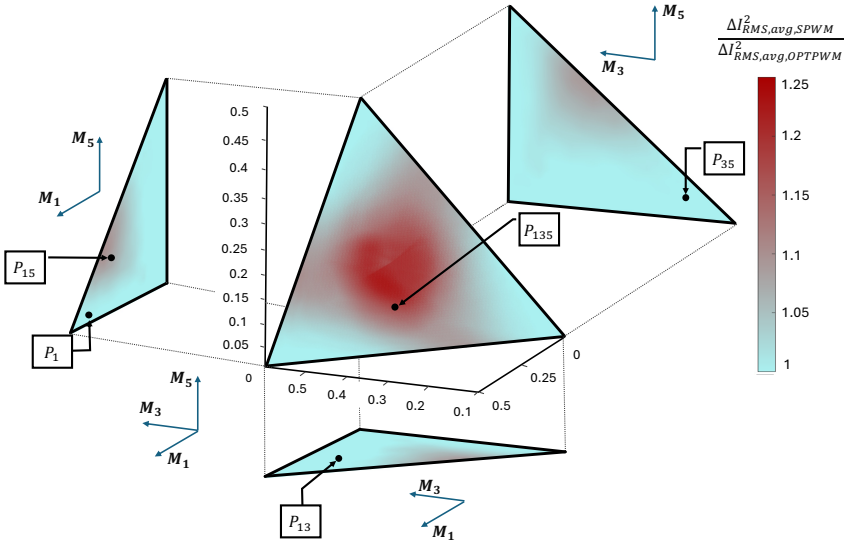

(b)

FIGURE 5.7: Performance of the optimal modulation in a seven-phase inverter. Ratio of the RMS values of the current ripple due to SVPWM (a) or SPWM (b) and the optimal modulation.

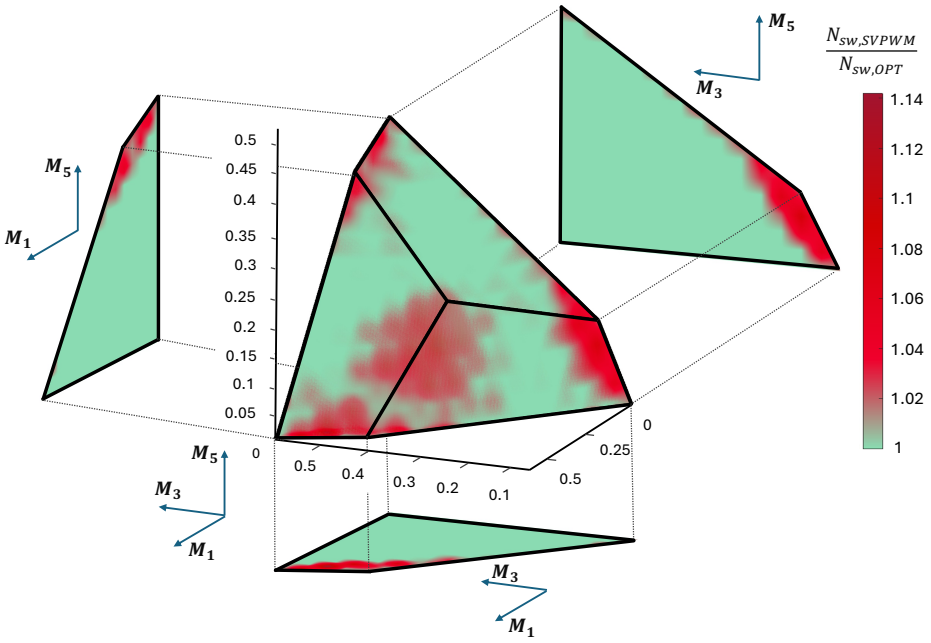

FIGURE 5.8: Ratio of the numbers of commutations due to SVPWM and the optimal strategy for a seven-phase inverter.

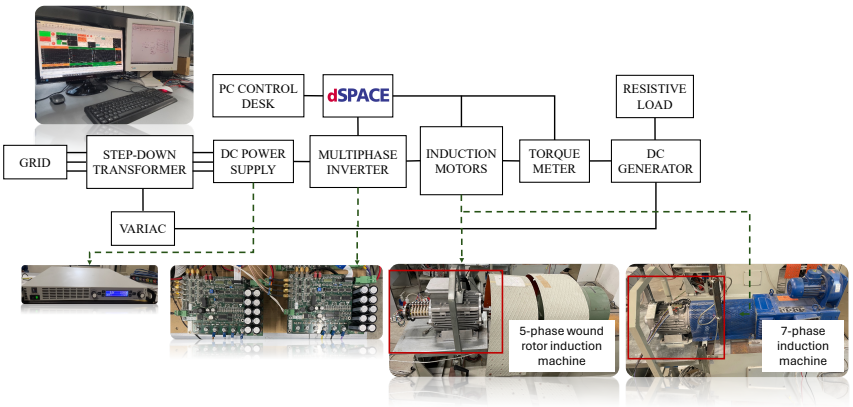

FIGURE 5.9: Experimental setup.

circulation of harmonic currents. These components typically operate at a frequency that is much lower than the switching frequency and do not affect the high-frequency current ripple. However, the control system must compensate for them in order to track the current reference. This control action interferes with the experimental tests and the calculation of the modulation index.

5.3.1 Five-Phase Inverter

The simulation results obtained in Section 5.2.2 have been validated through experimental tests. The test conditions correspond to the values of M_1 and M_3 highlighted in Fig. 5.4. The test results are listed in Tab. 5.6. At points P_1 and P_3, either M_1 or M_3 is zero. In accordance

TABLE 5.6: Performance of the optimal modulation strategy for the five-phase induction machine.

Test	M_1	M_3	$\frac{\Delta I^2_{RMS,avg,SPWM}}{\Delta I^2_{RMS,avg,OPT}}$	$\frac{\Delta I^2_{RMS,avg,SVPWM}}{\Delta I^2_{RMS,avg,OPT}}$
P_1	0.47	0	1	1.0116
P_3	0	0.47	1	1.0206
P_{13}	0.32	0.17	1.1248	1.0265

with the theory developed in Section 5.1.4, $m_{0,ref}$ equals 1/2 in both cases, and the optimal modulation coincides with the SPWM. As expected, the current ripple of SVPWM is slightly higher. At point P_{13}, the current ripple due to SPWM and SVPWM is greater than that of the optimal modulation, although the expected difference is more significant. Finally, Fig. 5.10 shows the waveform of the current ripple generated by the optimal modulation when the motor operates at a fundamental frequency of 10 Hz with and without injection of third harmonic currents. Fig. 5.10(a) presents the operating conditions of point P_1, while Fig. 5.10(b) refers to the operating conditions of point P_{13}.

Fig. 5.11 illustrates the spectrum of the phase current when the five-phase machine is operating at point P_{13}. The reference voltage vectors, which rotate at 10 Hz and 30 Hz, generate harmonic components in the phase current at the same frequencies, as can be observed in the detail window displaying the current spectrum up to 40 Hz. The amplitude of the fundamental component is identical for all strategies. Similarly, the third harmonic component of the phase current is independent of the strategy employed, thereby confirming that the reference voltage vectors are identical for all strategies. As can be observed in the second detail window, the spectrum around 3 kHz exhibits modulation sidebands situated at approximately the switching frequency. The spectral density of the optimal modulation is demonstrably lower than that of the other strategies.

5.3.2 Seven-Phase Inverter

Some experimental tests were performed to verify the results presented in Section 5.2.3. The test points are highlighted in Fig. 5.7, and the experimental results are reported in Tab. 5.7. In accordance with the theoretical predictions, the optimal strategy outperforms SVPWM at all points. Similarly, the RMS value of the current ripple due to SPWM is greater than that of the optimal modulation by up to 15%, except for points where the two strategies coincide, such as P_1 and P_3. Finally, Fig. 5.12 shows the waveform of the current ripple generated by the optimal

modulation when the motor operates at a fundamental frequency of 10 Hz with and without injection of third harmonic currents. Fig. 5.12(a) shows the operating conditions at point P_1, while Fig. 5.12(b) shows the operating conditions at point P_{135}.

Fig. 5.13 illustrates the spectrum of the phase current when the seven-phase machine operates at point P_{135}. The reference voltage vectors rotate at 10 Hz, 30 Hz, and 50 Hz, thereby generating the corresponding current harmonic components, as can be observed in the detail

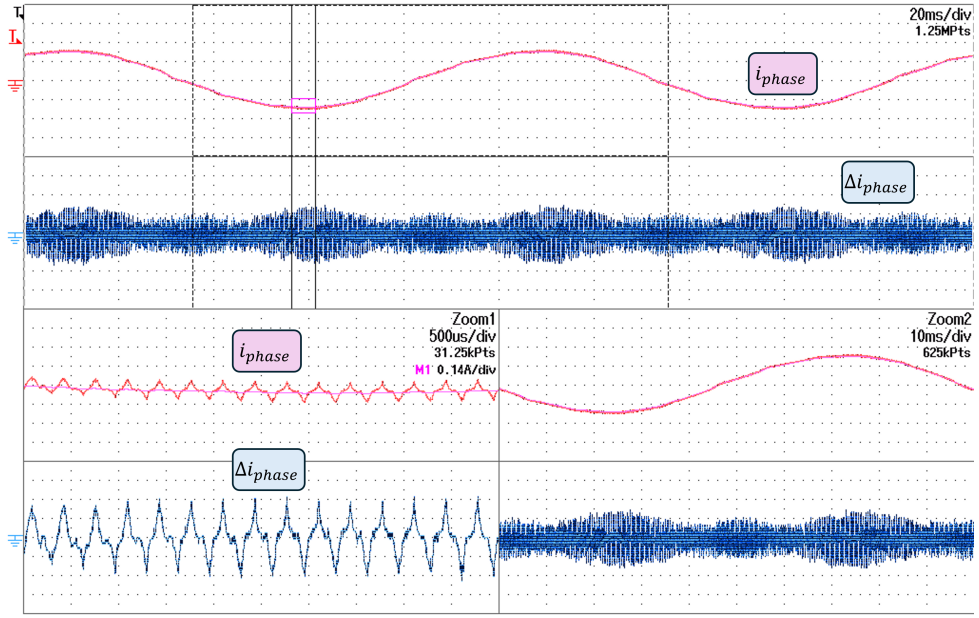

(a)

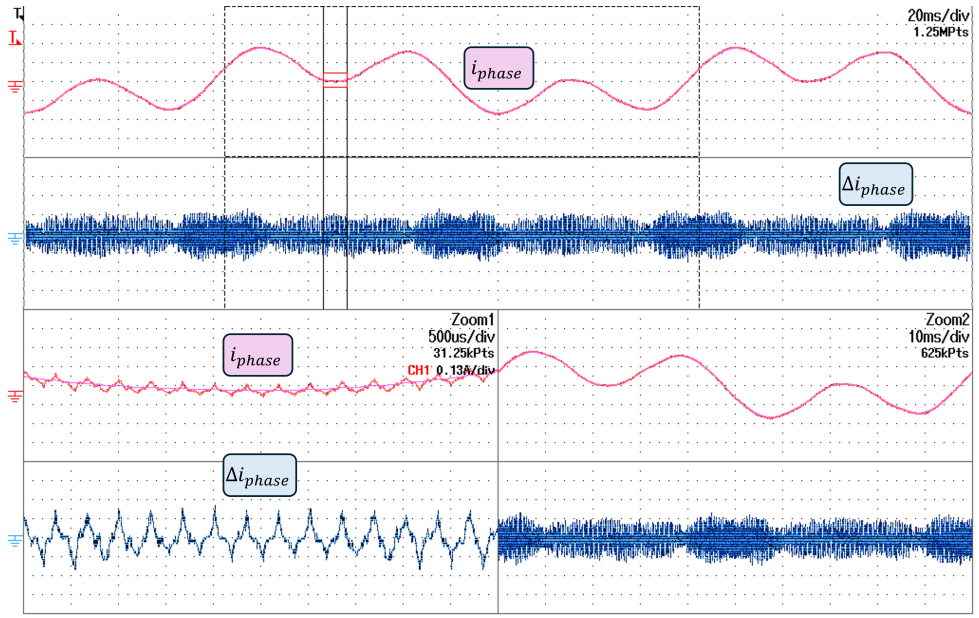

(b)

FIGURE 5.10: Waveform of the phase current of the five-phase induction machine when the fundamental frequency is 10 Hz. a) Operating point P_1. b) Operating point P_{13}. From top to bottom: phase current (1.34 A/div), phase current ripple $\triangle i$ (0.13 A/div).

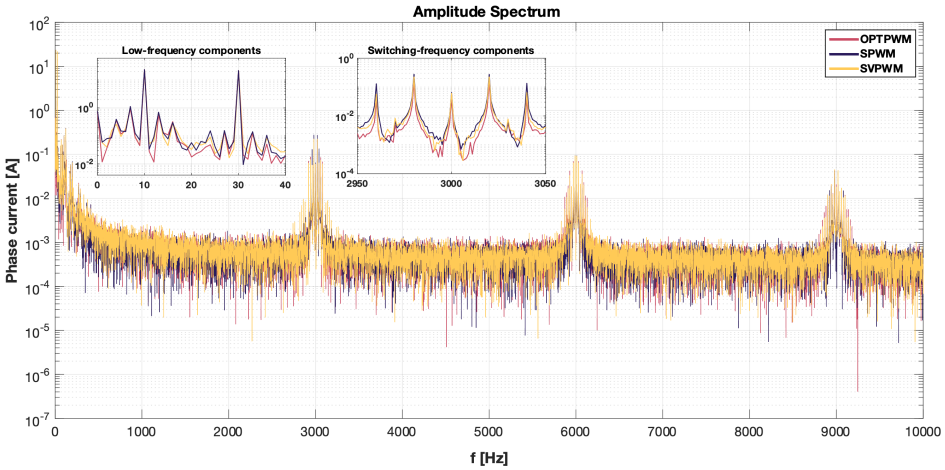

FIGURE 5.11: Spectrum of the phase current in the operating point P_{13} for the five-phase inverter.

TABLE 5.7: Performance of the optimal modulation strategy for the seven-phase induction machine.

Test	M_1	M_3	M_5	$\frac{\Delta I^2_{RMS,avg,SPWM}}{\Delta I^2_{RMS,avg,OPT}}$	$\frac{\Delta I^2_{RMS,avg,SVPWM}}{\Delta I^2_{RMS,avg,OPT}}$
P_1	0.3	0	0	1	1.001
P_{13}	0.1	0.25	0	1.008	1.0013
P_{15}	0.27	0	0.12	1.0359	1.0018
P_{135}	0.15	0.15	0.12	1.1503	1.0146
P_{35}	0	0.15	0.15	1.005	1.021

window displaying the current spectrum up to 70 Hz. All strategies result in the same amplitude for the fundamental, third, and fifth harmonic components. Once more, the spectrum in the vicinity of 3 kHz, as displayed in the second detail window, exhibits modulation sidebands around the switching frequency. The lowest spectral density is that of the optimal modulation.

5.4 Conclusions

In this research chapter a theoretical analysis to minimize the RMS value of the load current ripple in multiphase inverters with any odd number of phases has been presented. The developed approach provides a closed-form solution for the optimal zero-sequence component of the modulating signals, which is a function of the reference voltages or desired voltage vectors and the load high-frequency equivalent inductances. Therefore, this strategy is not limited to sinusoidal signals or steady-state conditions. On average, the proposed approach may theoretically reduce

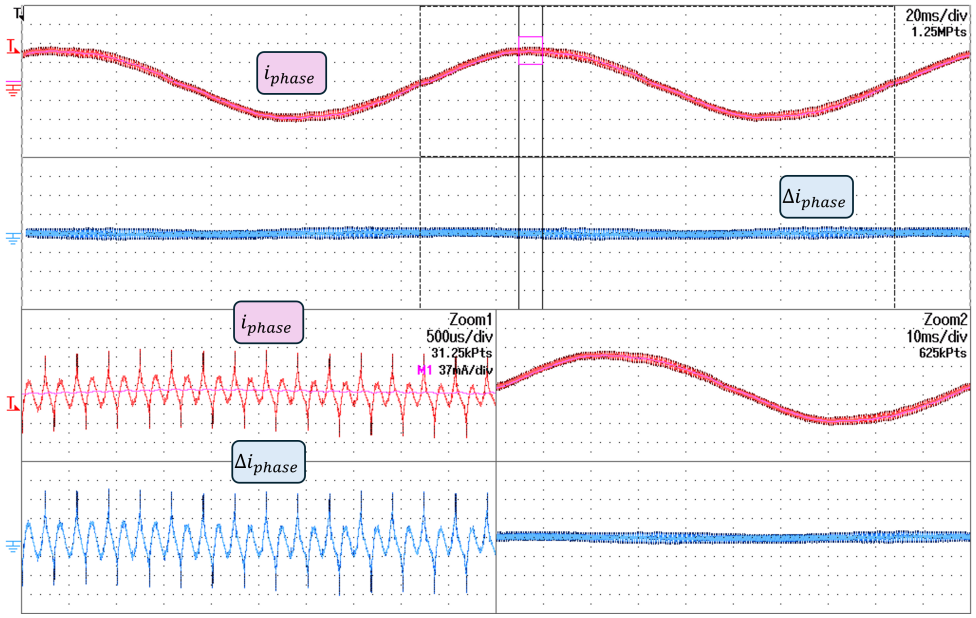

(a)

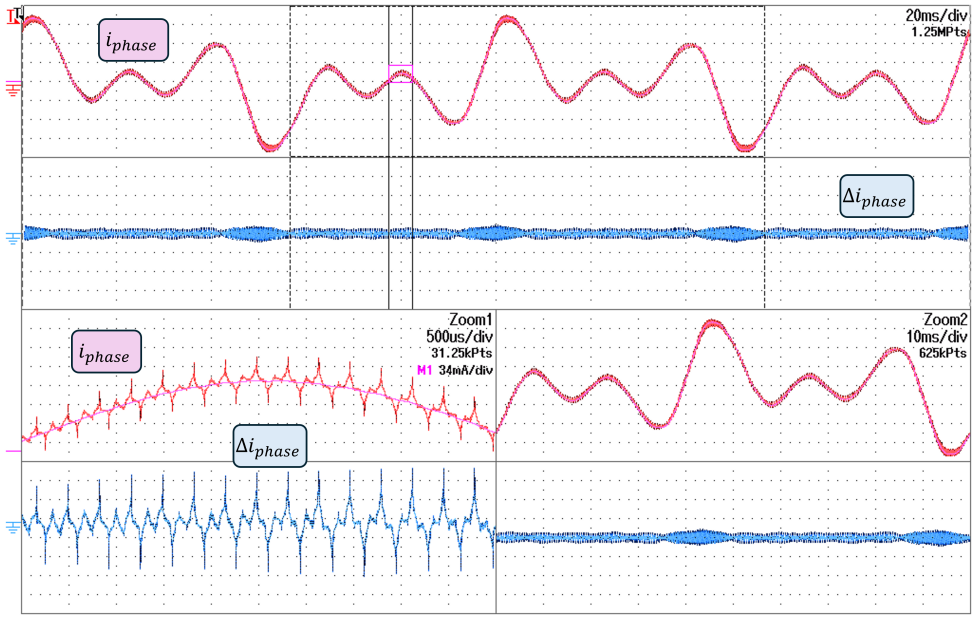

(b)

FIGURE 5.12: Waveform of the phase current of the seven-phase induction machine when the fundamental frequency is 10 Hz. a) Operating point P_1. b) Operating point P_{135}. From top to bottom: phase current (0.25 A/div), phase current ripple $\triangle i$ (0.035 A/div).

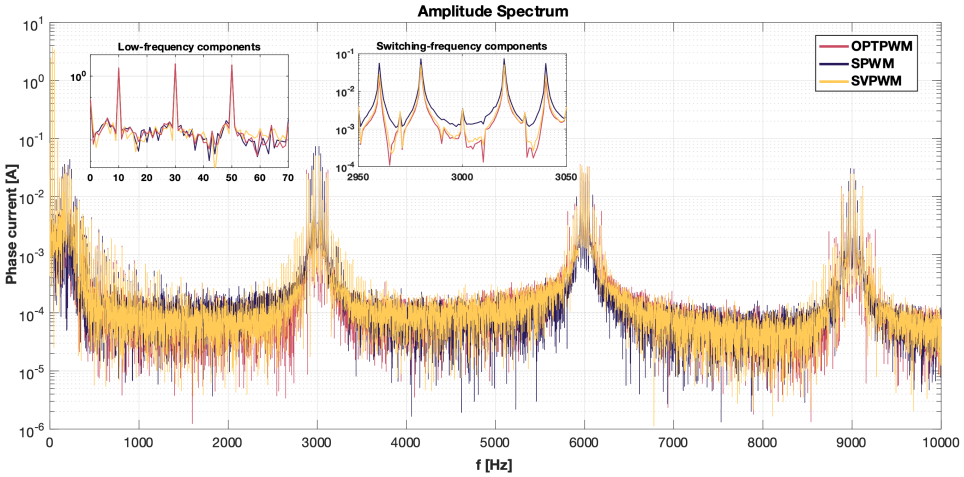

FIGURE 5.13: Spectrum of the phase current in the operating point P_{135} for the seven-phase inverter.

the RMS value of the load current ripple by up to 4% for five-phase inverters and 2% for seven-phase inverters compared to the SVPWM technique. When compared to SPWM, the reduction can be up to 25%, depending on the operating conditions. Moreover, the proposed technique reduces the number of switch commutations when high reference voltages are required, i.e., for values of the modulating indices close to the overmodulation region. The reduction may be up to 25% for five-phase inverters and 15% for seven-phase inverters. Consequently, power electronic switches experience a reduction in switching losses. The experimental results have confirmed the trends expected by the theoretical analysis. Although some of these findings have already been reported in the literature in special cases, this study provides a coherent theoretical motivation. The theoretical results have been validated by numerical and experimental tests with five- and seven-phase induction motors.

Bibliography

[1] B. Yu, W. Song, and Y. Guo, "A simplified and generalized svpwm scheme for two-level multiphase inverters with common-mode voltage reduction," *IEEE Transactions on Industrial Electronics*, vol. 69, no. 2, pp. 1378–1388, 2022.

[2] A. Lega, M. Mengoni, G. Serra, A. Tani, and L. Zarri, "Space vector modulation for multiphase inverters based on a space partitioning algorithm," *IEEE Transactions on Industrial Electronics*, vol. 56, no. 10, pp. 4119–4131, 2009.

[3] A. Chakrabarti, K. Sarkar, P. R. Kasari, B. Das, and S. K. Biswas, "A cb-pwm technique for eliminating cmv in multilevel multiphase vsi," *IEEE Transactions on Industrial Electronics*, vol. 70, no. 9, pp. 8666–8675, 2023.

[4] M. Gu, Z. Wang, P. Liu, and J. He, "Comparative study of advanced modulation and control schemes for dual three-phase pmsm drives with low switching frequencies," *IEEE Transactions on Transportation Electrification*, vol. 10, no. 1, pp. 962–975, 2024.

[5] H.-S. Jung, C.-E. Hwang, H.-S. Kim, S.-K. Sul, A. Hee-Won, and H. Yoo, "Minimum torque ripple pulse width modulation with reduced switching frequency for medium-voltage motor drive," *IEEE Transactions on Industry Applications*, vol. 54, no. 4, pp. 3315–3325, 2018.

[6] A. Lega, M. Mengoni, G. Serra, A. Tani, and L. Zarri, "Space vector modulation for multiphase inverters based on a space partitioning algorithm," *IEEE Trans. on Ind. Elect.*, vol. 56, no. 10, pp. 4119–4131, 2009.

[7] O. López, J. Álvarez, A. G. Yepes, F. Baneira, D. Pérez-Estévez, F. D. Freijedo, and J. Doval-Gandoy, "Carrier-based pwm equivalent to multilevel multiphase space vector pwm techniques," *IEEE Trans. on Ind. Elect.*, vol. 67, no. 7, pp. 5220–5231, 2020.

[8] B. Yu, W. Song, and Y. Guo, "A simplified and generalized svpwm scheme for two-level multiphase inverters with common-mode voltage reduction," *IEEE Trans. on Ind. Elect.*, vol. 69, no. 2, pp. 1378–1388, 2022.

[9] A. Chakrabarti, K. Sarkar, P. R. Kasari, B. Das, and S. K. Biswas, "A cb-pwm technique for eliminating cmv in multilevel multiphase vsi," *IEEE Trans. on Ind. Elect.*, vol. 70, no. 9, pp. 8666–8675, 2023.

[10] L. Zarri, M. Mengoni, A. Tani, G. Serra, and D. Casadei, "Minimization of the power losses in igbt multiphase inverters with carrier-based pulsewidth modulation," *IEEE Trans. on Ind. Elect.*, vol. 57, no. 11, pp. 3695–3706, 2010.

[11] L. Vancini, M. Mengoni, G. Rizzoli, G. Sala, L. Zarri, and A. Tani, "Carrier-based pwm overmodulation strategies for five-phase inverters," *IEEE Tran. on Pow. Elect.*, vol. 36, no. 6, pp. 6988–6999, 2021.

[12] A. G. Yepes and J. Doval-Gandoy, "Overmodulation method with adaptive x-y current limitation for five-phase induction motor drives," *IEEE Trans. on Ind. Elect.*, vol. 69, no. 3, pp. 2240–2251, 2022.

[13] D. Casadei, D. Dujic, E. Levi, G. Serra, A. Tani, and L. Zarri, "General modulation strategy for seven-phase inverters with independent control of multiple voltage space vectors," *IEEE Trans. on Ind. Elect.*, vol. 55, no. 5, pp. 1921–1932, 2008.

[14] E. Levi, D. Dujic, M. Jones, and G. Grandi, "Analytical determination of dc-bus utilization limits in multiphase vsi supplied ac drives," *IEEE Trans. on En. Conv.*, vol. 23, no. 2, pp. 433–443, 2008.

[15] A. M. S. R. Bowes, "Suboptimal switching strategies for micropocessor-controlled pwm inverter drives," *IEE Proceedings*, vol. 132, no. 3, pp. 133–148, 1985.

[16] D. Casadei, M. Mengoni, G. Serra, A. Tani, and L. Zarri, "A new carrier-based pwm strategy with minimum output current ripple for five-phase inverters," in *Proc. of EPE 2011*, 2011, pp. 1–10.

Chapter 6

Eccentricity Fault Diagnosis Using the Stray Flux

Recent years have witnessed significant advancements in the technological development of electric drives. The proliferation of electric vehicles necessitates high demands for reliability and flexibility in power transmission. The utilization of measuring sensors to measure the variables required for diagnosing potential faults in an electric motor can often be tedious and invasive. Consequently, research is progressively concentrating on alternate methods to assess the state of health of electrical machines. This chapter presents a methodology for diagnosing rotor eccentricity with sensors placed on the stator yoke, rendering the approach less invasive as the sensors are not included within the motor's stator and/or rotor housing.

6.1 Stray Flux

In recent years, Permanent Magnet Synchronous Motors (PMSMs) have surpassed induction motors in popularity across various industrial sectors, including electric transport vehicles [1], robotics, and aerospace [2]. The superior torque density demonstrated by PMSMs, is a significant factor contributing to their relative advantage over induction motors [3; 4]. Furthermore, the weight and dimensions of a PMSM are considerably reduced in comparison to an induction motor of equivalent power rating. Finally, induction motors typically exhibit more rotor joule losses compared to synchronous machines, resulting in diminished efficiency [5].

Nonetheless, irrespective of the motor type, unintentional malfunctions or failures may arise, leading to expensive repairs or replacements, as well as complete system failure. Consequently, in critical applications, constant health monitoring and early faults identification are essential to maintain optimal performance of electrical machines over a prolonged duration.

Most electrical machines include a standardized stator design; hence, any failure affecting the stator will show similar behavior irrespective of the motor's nature. The primary distinguishing characteristic among electrical machines lies in their rotor design. Therefore, a comprehensive examination of rotor failures must be performed for the particular machine under examination.

Since their measurement is simple, the currents are often used as signals for defect diagnosis. Moreover, the torque generated directly depends on the current and any distortion results in torque oscillations. However, given the widespread application of PMSMs in industries requiring high torque density, it is essential to possess an accurate and rapid torque regulation capability. The issue can be addressed by implementing closed-loop control systems that employ one or more PI regulators that keep the current waveform as sinusoidal as feasible, even in the event of a fault, hence minimizing torque oscillations. Consequently, the use of a closed-loop control system makes the measured currents a questionable diagnostic indicator. Conversely, the use of stray flux as a fault detector in PMSMs demonstrates significant promise, as it can convey information regarding the magnetic flux, including potential imbalances resulting from failures.

Multiple research have been performed to identify diverse faults in induction motors using stray flux [6]. Some utilize statistical approaches to identify pertinent features related to faults [7]. Alternative studies employ the frequency response of the stray flux signal [8–10] or the orbital analysis of vibrations [11; 12].

There is a lack of research in the literature that utilizes stray flux as a fault indicator in PMSMs. Few studies have been undertaken to assess stator faults such as short circuits [13; 14] or rotor faults such as magnet asymmetry [15] or eccentricity [16; 17]. Nevertheless, most of them rely on the utilization of an equivalent circuit for modeling the stray flux [18] surrounding the stator yoke. This approach always involves an approximation, as the path of the stray magnetic flux must be approximated using exact values for the rotor, air-gap, stator, and stray reluctances.

The current study examines the various forms of eccentricity, including static, dynamic, and mixed, that a PMSM may encounter. A static eccentricity failure occurs when the rotor's axial center misaligns with the stator's axial center. If the rotor's central axis deviates from the stator's central axis, it results in a dynamic eccentricity fault. Moreover, the simultaneous occurrence of static and dynamic eccentricities produces a third type of eccentricity known as mixed eccentricity. All the three types of eccentricity are depicted in Fig. 6.1.

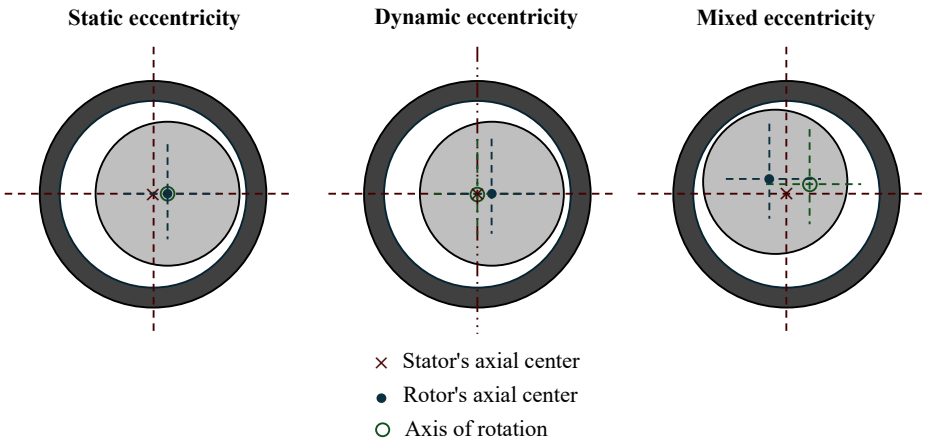

FIGURE 6.1: Types of eccentricity.

The research investigates the stray magnetic field outside the stator yoke as a failure signal, proving its superiority over the use of stator currents. The stray flux is described using the VSD, which allows to fully represent the stray flux through a space vector and a zero-sequence component. The utilization of space vector and zero sequence components facilitates the identification of the particular type of eccentricity present.

6.2 Machine and Stray Flux Equations

6.2.1 Stator Phase Voltage Equations

The phase voltage equation for a healthy motor is as follows:

$$v_k = R_k i_k + \sum_{z=1}^{3} M_{k,z} \frac{di_z}{dt} + e_k \quad k = 1, 2, 3 \tag{6.1}$$

where R_k is the resistance of the k-th stator phase, $M_{k,z}$ denotes the self and mutual inductances of the three-phase winding, e_k refers to the rotor BEMF induced in phase k, and i_k is the current flowing through the k-th stator winding.

In steady-state operating conditions, each phase variable x_k in (6.1) can be defined through its corresponding phasor as follows:

$$x_k = \tfrac{1}{2} \sum_{h=1}^{\infty} \Re_e\{\bar{X}_k^{(h)}\ e^{jh\omega_e t}\} \qquad k = 1, 2, 3 \tag{6.2}$$

where the symbol $\Re_e$ indicates the real part operator and ω_e is the rotor electrical speed. For each harmonic h, a representative vector is provided in the following manner:

$$\bar{\mathbf{X}}_{\mathbf{3ph}}^{(\mathbf{h})} = [\bar{X}_1^{(h)}\ \bar{X}_2^{(h)}\ \bar{X}_3^{(h)}\ ]'. \tag{6.3}$$

where $'$ defines the transposition operation.

Based on (6.1) and considering (6.3), since the current derivatives in the phasors domain can be rewritten as $\frac{d\bar{I}_k^{(h)}}{dt} = jh\omega_e \bar{I}_k^{(h)}$ $(k = 1, 2, 3)$, the vector of the three-phase currents is written as follows:

$$\bar{\mathbf{I}}_{\mathbf{3ph}}^{(\mathbf{h})} = \frac{\bar{\mathbf{V}}_{\mathbf{3ph}}^{(\mathbf{h})} - \bar{\mathbf{E}}_{\mathbf{3ph}}^{(\mathbf{h})}}{\hat{\mathbf{Z}}_{\mathbf{3ph}}^{(\mathbf{h})}} \tag{6.4}$$

where $\hat{\mathbf{Z}}_{\mathbf{3ph}}^{(\mathbf{h})}$ is the impedance matrix defined in this manner:

$$\hat{\mathbf{Z}}_{\mathbf{3ph}}^{(\mathbf{h})} = \begin{bmatrix} R_1 - jh\omega_e M_{11} & -jh\omega_e M_{12} & -jh\omega_e M_{13} \\ -jh\omega_e M_{21} & R_2 - jh\omega_e M_{22} & -jh\omega_e M_{23} \\ -jh\omega_e M_{31} & -jh\omega_e M_{32} & R_3 - jh\omega_e M_{33}. \end{bmatrix} \tag{6.5}$$

In healthy operating conditions, disregarding high-order harmonic components, the stator currents are sinusoidal as a result of the sinusoidal voltages supplied to the motor's stator phases. Furthermore, the induced rotor Back Electromotive Force (BEMF) are symmetrical and balanced. Conversely, if a rotor eccentricity is present, the matrix $\hat{\mathbf{Z}}_{\mathbf{3ph}}^{(\mathbf{h})}$ exhibits an alteration due to the inconsistent air-gap, which affects the reluctance of the magnetic circuit. Additionally, an irregular air-gap produces an asymmetrical flux generated by the magnets that links the stator phases. Consequently, the eccentricity results in current harmonic components, identified for $h > 1$ in (6.4). However, the control architecture employs one or several PI regulators to keep the currents as sinusoidal as possible, hence achieving lower torque oscillations. Therefore, even in the event of a failure, such as a rotor eccentricity, under an acceptable degree of fault severity, the h-th current harmonic component due to the fault in (6.4) is compensated by an adequately designed control system [15]. On the contrary, the influence of the fault is visible on the stray flux due to the magnets, on which the control system has no effect.

It is clear that stator currents are not a reliable diagnostic signal, and stray flux becomes an important fault indicator.

6.2.2 Stray Flux Equations

The magnetic flux in PMSM is produced by the rotor-mounted magnets and the electric currents flowing through the stator winding. Owing to the materials' permeability, not all flux lines are confined within the air gap, and in ferromagnetic materials, a small fraction of the flux surrounds the stator yoke. The latter defines the stray flux. Therefore, the radial component of the stray flux can be measured by placing sensors external to the stator yoke. Considering the k-th phase of a three-phase motor with p pole pairs, by positioning three sensors (A, B, C) at $(p-1)\frac{2}{3}\pi(k-1)$ mechanical degree intervals around the stator, the associated stray flux is as

follows:

$$\varphi_{sf,w} = \varphi_{e,w} + \sum_{z=1}^{3} M_{w,z} di_z \quad w = A, B, C \tag{6.6}$$

where $M_{w,z}$ indicates the mutual inductances between the w-th stray flux sensor and the z-th stator phase, and $\varphi_{e,w}$ denotes the flux generated by the magnets linked to the w-th stray flux sensor.

According to (6.2) and (6.3),(6.6) can be written in terms of phasors, as follows:

$$\bar{\mathbf{\Phi}}^{(\mathbf{h})}_{\mathbf{3sf}} = \bar{\mathbf{\Phi}}^{(\mathbf{h})}_{\mathbf{e,3sf}} + \hat{\mathbf{Z}}_{\mathbf{3sf}} \bar{\mathbf{I}}^{(\mathbf{h})}_{\mathbf{3ph}} \tag{6.7}$$

where

$$\hat{\mathbf{Z}}_{\mathbf{3sf}} = \begin{bmatrix} M_{A1} & M_{A2} & M_{A3} \\ M_{B1} & M_{B2} & M_{B3} \\ M_{C1} & M_{C2} & M_{C3} \end{bmatrix}. \tag{6.8}$$

When positioning the stray flux sensors, it is necessary to take into account the motor fins. The length of the fins vary according to the motor design but, typically, unless for specific purposes, they are not shorter than 1 cm. Accordingly, it is not possible to put the stray flux sensors directly on the surface of the stator since the presence of the fins introduces a significant air-gap between the stator and the stray flux sensors. As a result, the matrix is close to zero due to the vacuum permeability. Therefore, (6.6) becomes:

$$\varphi_{sf,w} \simeq \varphi_{e,w} \quad w = A, B, C. \tag{6.9}$$

In the phasors domain:

$$\bar{\mathbf{\Phi}}^{(\mathbf{h})}_{\mathbf{3sf}} \simeq \bar{\mathbf{\Phi}}^{(\mathbf{h})}_{\mathbf{e,3sf}}. \tag{6.10}$$

Thus, the presence of fins surrounding the stator results in the primary cause of stray flux generation being the magnetic flux produced by the magnets.

According to (6.9), applying the VSD (2.1), the space vector and the zero-sequence component of the stray flux are:

$$\bar{\varphi}_{sf_1} \simeq \frac{2}{3}(\varphi_{e,A} + \varphi_{e,B}\bar{\alpha} + \varphi_{e,C}\bar{\alpha}^2) \tag{6.11}$$

$$\varphi_{sf_0} \simeq \frac{2}{3}(\varphi_{e,A} + \varphi_{e,B} + \varphi_{e,C}). \tag{6.12}$$

The complex fast Fourier transform allows to rewrite (6.11) as sum of rotating and counter-rotating harmonic components, as follows:

$$\bar{\varphi}_{sf_1} = \sum_{h=1}^{\infty} \bar{\varphi}_{sf_1}^{(h+)} e^{jh\omega_e t} + \sum_{h=1}^{\infty} \bar{\varphi}_{sf_1}^{(h-)} e^{-jh\omega_e t}. \tag{6.13}$$

where the notation $h+$ and $h-$ is used to identify the h-th harmonic component of the positive and negative sequence, respectively.

6.2.3 Rotor Eccentricity Equations

Rotor eccentricity leads to a non-uniform air gap thickness δ, which deviates from its average value δ_0, as expressed hereafter:

$$\delta = \delta_0 + \Re_e\{\bar{\delta}_\epsilon \; e^{-j\,\theta_s}\} \tag{6.14}$$

where $\bar{\delta}_\epsilon$ is a complex quantity, which can be represented in polar form as $\delta_\epsilon e^{j\,\theta_e}$. The magnitude δ_ϵ indicates the severity of the eccentricity, while the phase angle θ_e defines its electrical position. Additionally, θ_s is an angular coordinate used to specify a position in the air gap.

The reciprocal of (6.14) can be expressed in accordance with the first-order truncated Fourier transform in the following manner:

$$g = \frac{1}{\delta} \simeq g_0 + \Re_e\{\bar{g}_1 e^{-j\,\theta_s}\}. \tag{6.15}$$

where g_0 is a constant, and $\bar{g}_1$ depends on the eccentricity position θ_e.

Permanent magnets and currents induce Magnetomotive Forces (MMFs) in the air-gap, which can be expressed as follows:

$$f_m(\theta_s) = \sum_{\rho=1}^{\infty} \Re_e\{\bar{F}_\rho e^{-j\,\rho\theta_s}\} \tag{6.16}$$

where the component for $\rho = 0$ can be demonstrated to be zero because the divergence of the flux density is zero.

Consequently, in case of an isotropic rotor and neglecting the stator slotting, the resulting air-gap magnetic field can be evaluated as:

$$h \simeq g f_m. \tag{6.17}$$

Substituting (6.15) and (6.16) in (6.17) leads to:

$$\begin{aligned} h &\simeq \sum_{\rho=1}^{\infty}[\Re_e\{\bar{F}_\rho e^{-j\,\rho\theta_s}\}][g_0 + \Re_e\{\bar{g_1} e^{-j\,\theta_s}\}] = \\ &= \sum_{\rho=1}^{\infty}\Re_e\{\frac{g_0\bar{F}_\rho e^{-j\,\rho\theta_s} + \bar{F}_\rho \bar{g_1}^* e^{-j\,(\rho-1)\theta_s} + \bar{F}_\rho \bar{g_1} e^{-j\,(\rho+1)\theta_s}}{2}\} = \\ &= \sum_{\rho=1}^{\infty}\Re_e\{\bar{H}_\rho e^{-j\,\rho\theta_s} + \bar{H}_{\rho-1} e^{-j\,(\rho-1)\theta_s} + \bar{H}_{\rho+1} e^{-j\,(\rho+1)\theta_s}\}. \end{aligned} \tag{6.18}$$

Expression (6.18) outlines how each spatial MMF harmonic ρ generates a spatial distribution of the magnetic field characterized by the sum of three harmonic components with space periodicity of order ρ, $\rho - 1$ and $\rho + 1$.

Based on (6.18), assuming that the k-th sensor is placed in a position θ_{sk}, in steady state operating conditions, given a certain number of pole pairs p, the field distribution due to the most significant harmonic of the MMF ($\rho = p$) is

$$h_k(t) = \Re_e\{\bar{H}_p(t) e^{-j\,p\theta_{sk}} + \bar{H}_{p-1}(t) e^{-j\,(p-1)\theta_{sk}} + \bar{H}_{p+1}(t) e^{-j\,(p+1)\theta_{sk}}\}. \tag{6.19}$$

Considering an eccentricity that does not substantially modify in time the air-gap thickness, i.e., $g_0(t) = g_0$, and a function $\bar{g_1}(t) = \bar{g}_{1s} + \bar{g}_{1d} e^{j\,\omega_m t}$ that encompasses both static and dynamic eccentricity effects, the terms in (6.19) are as follows:

$$\begin{aligned} \bar{H}_p(t) &\simeq \frac{g_0 \bar{F}_p e^{j\,p\omega_m t}}{2} \\ \bar{H}_{p-1}(t) &\simeq \frac{\bar{F}_p e^{j\,p\omega_m t}\bar{g}_{1s}^*}{2} + \frac{\bar{F}_p e^{j\,(p-1)\omega_m t}\bar{g}_{1d}^*}{2} \\ \bar{H}_{p+1}(t) &\simeq \frac{\bar{F}_p e^{j\,p\omega_m t}\bar{g}_{1s}}{2} + \frac{\bar{F}_p e^{j\,(p+1)\omega_m t}\bar{g}_{1d}}{2} \end{aligned} \tag{6.20}$$

where ω_m is the mechanical speed of the motor.

To accurately measure the air-gap magnetic field, it is critical to determine the optimal placement of the probes. In this research study, a generic machine with a number of pole pairs greater than two is considered. As a result, three probes are positioned in mechanical positions $\theta_{sk} = (p-1)\frac{2\pi}{3}(k-1)$ each other. According to VSD, using the three probes allows to fully describe the air-gap magnetic field with a space vector and a zero-sequence component defined as follows:

$$\bar{h}_1 = \frac{2}{3}\sum_{k=1}^{3} h_k(t) e^{j\frac{2\pi}{3}(k-1)} \tag{6.21}$$

$$h_0 = \frac{2}{3}\sum_{k=1}^{3} h_k(t). \tag{6.22}$$

Substituting (6.19) in (6.21) and (6.22) leads to:

$$\begin{aligned}\bar{h}_1 = \frac{1}{6}\sum_{k=1}^{3} & \bar{H}_p(t)e^{-j\,[p(p-1)-1]\frac{2\pi}{3}(k-1)} + \bar{H}_p^*(t)e^{j\,[p(p-1)+1]\frac{2\pi}{3}(k-1)} + \\ & + \bar{H}_{p-1}(t)e^{-j\,[(p-1)^2-1]\frac{2\pi}{3}(k-1)} + \bar{H}_{p-1}^*(t)e^{j\,[(p-1)^2+1]\frac{2\pi}{3}(k-1)} + \\ & + \bar{H}_{p+1}(t)e^{-j\,[(p^2-2)]\frac{2\pi}{3}(k-1)} + \bar{H}_{p+1}^*(t)e^{j\,[p^2]\frac{2\pi}{3}(k-1)}\end{aligned} \tag{6.23}$$

$$\begin{aligned}h_0 = \frac{2}{3}\sum_{k=1}^{3} & \Re_e\{\bar{H}_p(t)e^{-j\,p(p-1)\frac{2\pi}{3}(k-1)} + \bar{H}_{p-1}(t)e^{-j\,(p-1)^2\frac{2\pi}{3}(k-1)} + \\ & + \bar{H}_{p+1}(t)e^{-j\,(p^2-1)\frac{2\pi}{3}(k-1)}\}.\end{aligned} \tag{6.24}$$

For a two pole pairs machine ($p = 2$) the following are obtained:

$$\bar{h}_1 = \bar{H}_1(t) + \bar{H}_2^*(t) \tag{6.25}$$

$$h_0 = 2\Re\{\bar{H}_3(t)\} \tag{6.26}$$

Substituting (6.20) in (6.25) and (6.26) yields:

$$\bar{h}_1 = \frac{\bar{F}_2\bar{g}_{1s}^*}{2}e^{j\,2\omega_m t} + \frac{\bar{F}_2\bar{g}_{1d}^*}{2}e^{j\,\omega_m t} + g_0\bar{F}_2{}^* e^{-j\,2\omega_m t} \tag{6.27}$$

$$h_0 = \Re_e\{\frac{\bar{F}_2\bar{g}_{1s}}{2}e^{j\,2\omega_m t} + \frac{\bar{F}_2\bar{g}_{1d}}{2}e^{j\,3\omega_m t}\}. \tag{6.28}$$

Equations (6.27) and (6.28) incorporate the effects of both static and dynamic eccentricity, hence characterizing mixed eccentricity.

In case of healthy machine, with no eccentricity, (6.27) becomes:

$$\begin{aligned}\bar{h}_1 &= g_0\bar{F}_2{}^* e^{-j\,2\omega_m t} \\ h_0 &= 0.\end{aligned} \tag{6.29}$$

A machine affected by a static eccentricity yields:

$$\begin{aligned}\bar{h}_1 &= \frac{\bar{F}_2\bar{g}_{1s}^*}{2}e^{j\,2\omega_m t} + g_0\bar{F}_2{}^* e^{-j\,2\omega_m t} \\ h_0 &= \Re_e\{\frac{\bar{F}_2\bar{g}_{1s}}{2}e^{j\,2\omega_m t}\}.\end{aligned} \tag{6.30}$$

Finally, in case of dynamic eccentricity, it results:

$$\begin{aligned}\bar{h}_1 &= \frac{\bar{F}_2\bar{g}_{1d}^*}{2}e^{j\,\omega_m t} + g_0\bar{F}_2{}^* e^{-j\,2\omega_m t} \\ h_0 &= \Re_e\{\frac{\bar{F}_2\bar{g}_{1d}}{2}e^{j\,3\omega_m t}\}.\end{aligned} \tag{6.31}$$

TABLE 6.1: Low-order harmonic content of the air-gap magnetic field based on the machine state of health.

Healthy	Static eccentricity	Dynamic eccentricity	Mixed eccentricity
Space vector			
$-2\omega_m$	$-2\omega_m$, $+2\omega_m$	$-2\omega_m$, $+\omega_m$	$-2\omega_m$, $+\omega_m$, $+2\omega_m$
Zero-sequence component			
0	$2\omega_m$	$3\omega_m$	$2\omega_m$, $3\omega_m$

In summary, depending on its state of health, a machine with two pole pairs exhibits the following harmonic components in the space vector and zero-sequence component of the air-gap magnetic field:

- **Healthy**: the space vector only contains an harmonic component at the fundamental frequency $-2\omega_m$, and the zero-sequence component is zero.
- **Static eccentricity**: alongside the counter-rotating fundamental harmonic component present in healthy condition, a fundamental rotating $+2\omega_m$ harmonic component arises in both the spectrum of the space vector and the zero-sequence component.
- **Dynamic eccentricity**: in addition to the healthy state, the space vector has a component at the mechanical frequency ω_m, whereas the common mode component has a contribution three times the mechanical frequency.
- **Mixed eccentricity**: all the effects of static and dynamic eccentricity are present.

Tab. 6.1 summarizes the previously discussed low-order harmonic content of the air-gap magnetic field based on the machine state of healthy.

According to the equivalent magnetic circuit of a PMSM [18], it has been shown that the stray flux surrounding the stator yoke differs from the air-gap flux solely by a factor given by the stator and stray flux reluctances [13]. Consequently, the magnetic field measured outside the stator yoke possesses the same informational content as that observed at the air-gap, albeit with a lower magnitude. Such a result enables the placement of probes external to the stator yoke for the measurement of stray flux, leading to a non-invasive solution. Furthermore, the probes do not require pre-installation during the motor design phase, as they may be readily attached to the stator at any moment.

6.3 Simulation Results

Several machine parameters are required to evaluate the matrices (6.5) and (6.8) as well as the flux generated by the magnets under healthy and faulty operating conditions. For this purpose, in this study, a numerical approach based on finite-element analysis is used.

The considered three-phase PMSM has a power of 3.5 kW with a rated speed of 1500 RPM, a rated current of 10 A, and two pole pairs. The stator winding is arranged in a single layer and there is not any magnet skew on the rotor. The motor numerical model has been designed utilizing the Altair Flux Motor software. The latter refers to a powerful tool capable of accurate and specific simulations, thereby gathering all the parameters associated with the healthy machine. In order to replicate the faulty machine, the motor's geometry from Altair Flux Motor has been imported into Altair Flux. This software environment enables changing the motor's geometry to simulate different kinds of eccentricity. Additionally, it allows inserting the stray flux coils around the stator yoke.

In order to consider the presence of the fins, the stray flux sensors are placed at 1 cm from the stator surface. The overall structure of the motor is illustrated in Fig. 6.2.

Several simulations were carried out for the finite element analysis. The motor model is conventional, with the rotor rotating and moving radially in a position x-y that varies in accordance with the trajectory of the eccentricity considered. The currents flowing into the stator winding are imposed and supposed sinusoidal. The control strategy adopted is the Field Oriented Control (FOC) with the flux produced by the magnets having just the d-axis component aligned with the magnetic axis of the phase A.

The ferromagnetic non-linear material utilized is the alloy steel $M800_50$, while the magnets used consist of $NdFeB_1110_2500$ with a radial magnetization. No-skew of the rotor is adopted.

The analysis of the flux values is conducted during the post-processing phase. In particular, the fluxes associated with the three stray flux sensors are taken into account for the specific eccentricity in question.

A preliminary simulation was conducted to evaluate the degree to which the flux generated by the stator currents (armature flux) contributes to the stray flux. Fig. 6.3 illustrates the amplitude spectrum of the stray flux space vector in a healthy machine. As expected, the armature flux, despite the full motor load, leads to a negligible reduction of the harmonic component at frequency $-2\omega_m$ of the stray flux, suggesting that the influence of the armature flux on the stray flux can be disregarded. To extensively verify the aforementioned claim, the inductances between stray flux sensors and stator windings were computed. Even considering eccentricity, Fig. 6.4 shows that the inductances have a very low value, thereby reaffirming the correctness of (6.9) and (6.9).

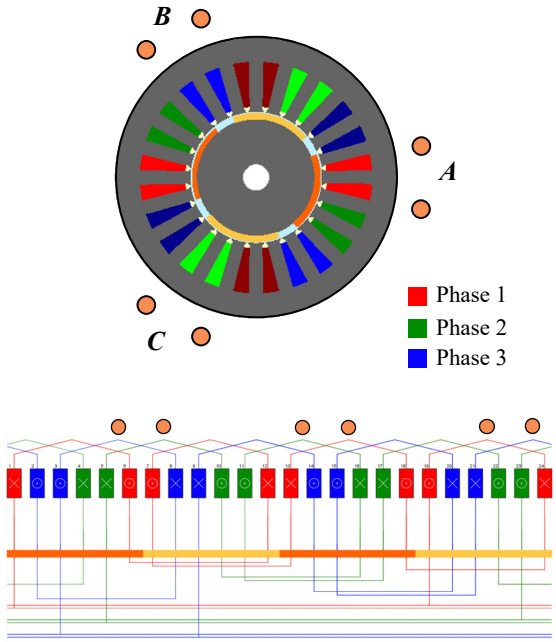

FIGURE 6.2: Layout of the motor considered for the finite element simulations.

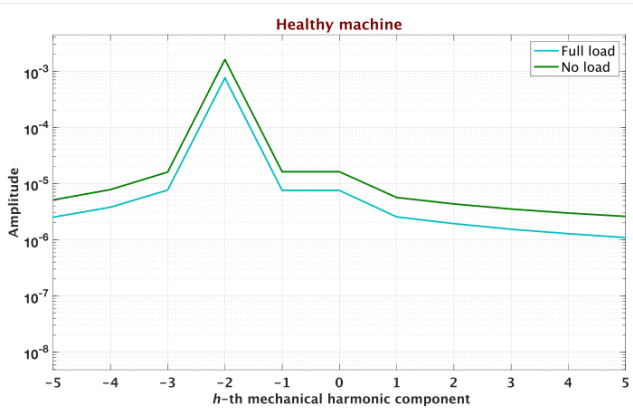

FIGURE 6.3: Spectrum of the stray flux space vector in case of healthy machine at 1500 RPM under no-load and full-load operating conditions.

The amplitude spectrum of the space vectors for two degrees of eccentricity severity are presented in Fig. 6.5, while the space vector and zero-sequence component spectrum for an eccentricity severity of 25% are illustrated in Fig. 6.6. It can be appreciated how the harmonics components coincide with those predicted by the analytical model and reported in Tab. 6.1.

It is relevant to note that even in the presence of eccentricity, the second order counter-rotating harmonic component observed in a healthy condition, remains unchanged in amplitude. Furthermore, all components resulting from eccentricity exhibit approximately constant amplitude regardless of the occurring eccentricity type . For example, the harmonic component at angular frequency $+\omega_m$ resulting from dynamic eccentricity exhibits an amplitude approximately equivalent to that of the harmonic at angular frequency $+2\omega_m$ arising from static eccentricity. Consequently, the harmonic order, rather than the amplitude, is crucial for distinguishing the

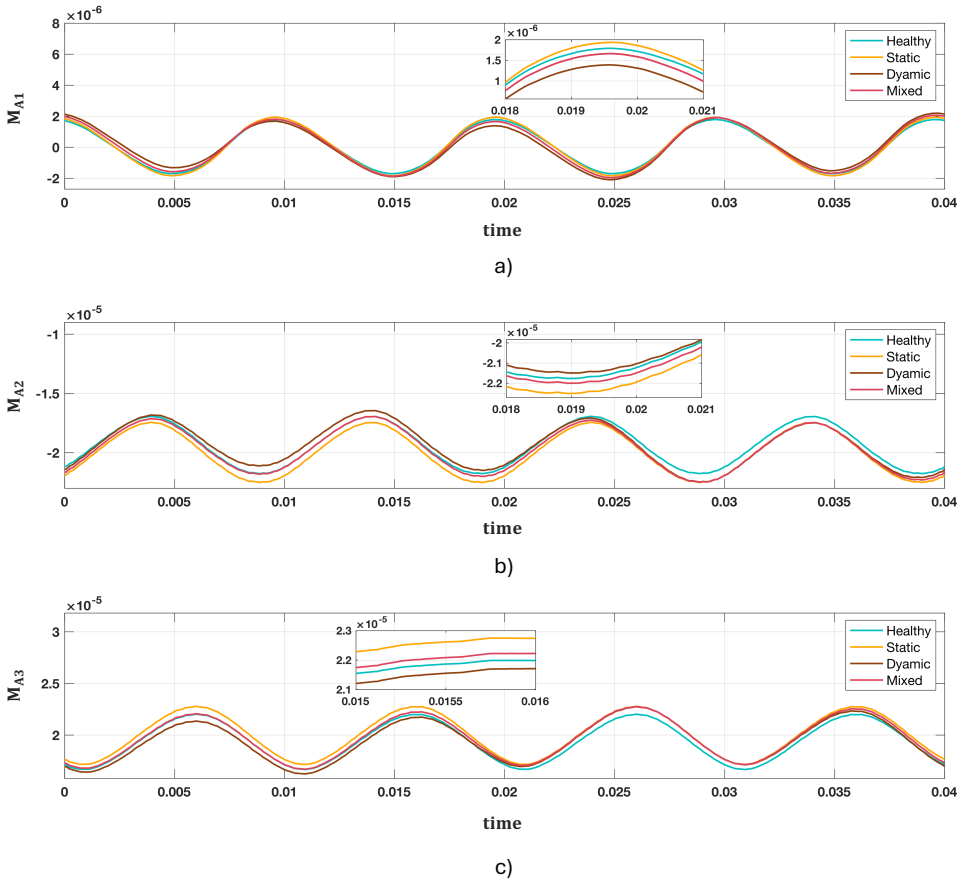

FIGURE 6.4: Inductances between the stray flux coil A and the stator windings measured in healthy condition and in case of various types of eccentricity. The severity is 25% of the air-gap thickness. a) The inductance between the stray flux coil A and phase 1. b) Inductance between the stray flux coil A and phase 2. c) Inductance between the stray flux coil A and phase 3.

eccentricity type.

6.4 Conclusions

This chapter introduced a diagnostic method to recognize rotor eccentricity in permanent magnet motors. The technique was implemented for a three-phase surface-mounted permanent magnet motor but can be adapted to any motor with N-phases and any magnet configuration.

The proposed technique uses flux sensors positioned externally on the stator back iron to measure the stray flux, which is characterized, utilizing VSD, through a space vector and a homopolar component.

Finite element simulations have been used to validate the developed technique by demonstrating that the information content of stray flux is appropriate to distinguish among several forms of eccentricity, namely static, dynamic, and mixed eccentricity.

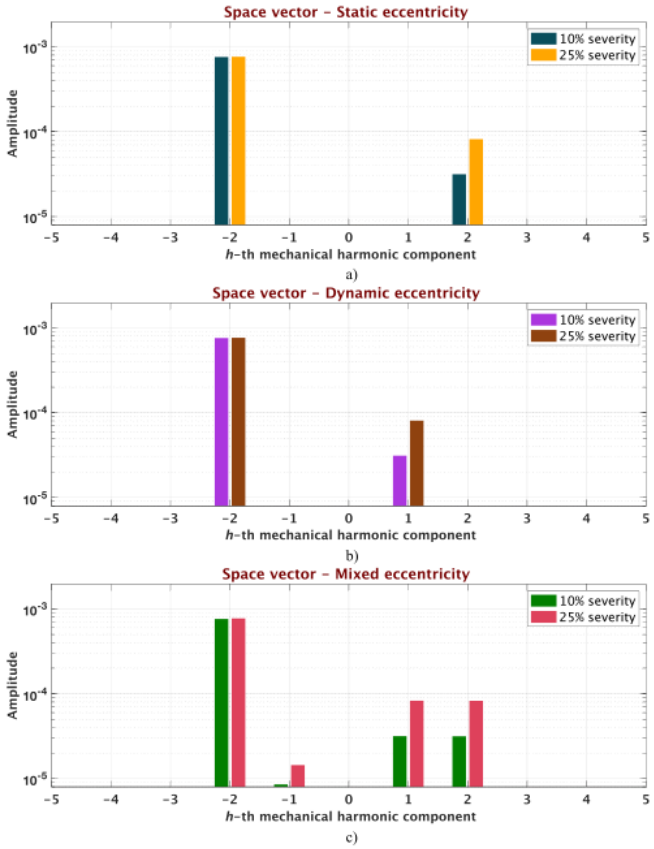

FIGURE 6.5: Amplitude spectrum of the stray flux space vector for two different levels of eccentricity, given as a percentage of the air-gap thickness, under full load operating conditions at a rotational speed of 1500 RPM. a) Static eccentricity. b) Dynamic eccentricity. c) Mixed eccentricity.

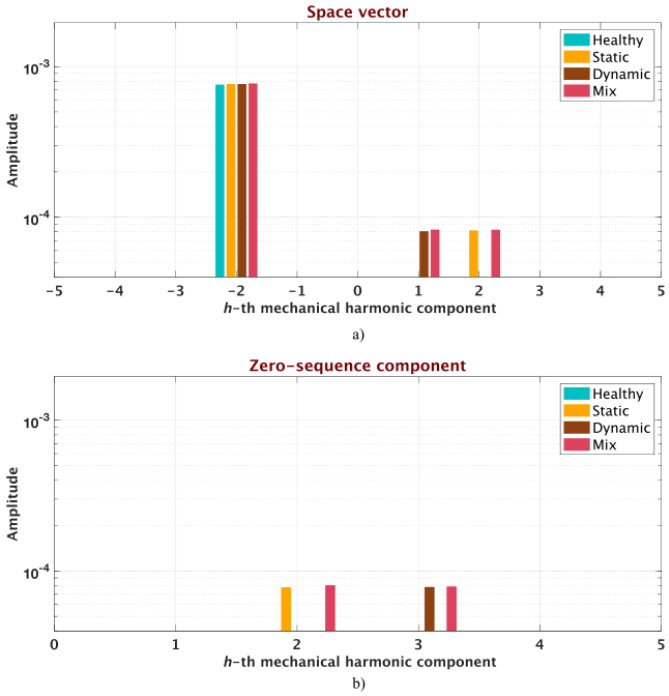

FIGURE 6.6: Amplitude spectrum in case of healthy and faulty machine under full load operating conditions at a rotational speed of 1500 RPM. a) Space vector $\bar{\varphi}_{sf_1}$. b) Zero-sequence component φ_{sf_0}.

Bibliography

[1] L. Cao, Y. Zuo, S. Xie, C. C. Hoang, B. S. Han, and C. H. T. Lee, "Comparative study of permanent-magnet vernier motor and interior permanent-magnet motor for hybrid electric vehicles," *IEEE Transactions on Industry Applications*, vol. 59, no. 6, pp. 6601–6614, 2023.

[2] C. Jenkins, S. Jones-Jackson, I. Zaher, G. Pietrini, R. Rodriguez, J. Cotton, and A. Emadi, "Innovations in axial flux permanent magnet motor thermal management for high power density applications," *IEEE Transactions on Transportation Electrification*, vol. 9, no. 3, pp. 4380–4405, 2023.

[3] C. Diao, W. Zhao, Y. Liu, and X. Wang, "Permanent magnet assisted synchronous reluctance motor with asymmetric rotor for high torque performance," *CES Transactions on Electrical Machines and Systems*, vol. 7, no. 2, pp. 179–186, 2023.

[4] Y. Pu, Z. Xiang, M. Jiang, and X. Zhu, "Investigation on electromagnetic torque of a flux-switching permanent magnet motor from perspective of flux density harmonic reduction ratio," *IEEE Transactions on Magnetics*, vol. 58, no. 2, pp. 1–6, 2022.

[5] V. Dmitrievskii, V. Prakht, E. Valeev, A. Paramonov, V. Kazakbaev, and A. Anuchin, "Comparative study of induction and wound rotor synchronous motors for the traction drive of a mining dump truck operating in wide constant power speed range," *IEEE Access*, vol. 11, pp. 68 395–68 409, 2023.

[6] Y. Park, C. Yang, J. Kim, H. Kim, S. B. Lee, K. N. Gyftakis, P. A. Panagiotou, S. H. Kia, and G.-A. Capolino, "Stray flux monitoring for reliable detection of rotor faults under the influence of rotor axial air ducts," *IEEE Transactions on Industrial Electronics*, vol. 66, no. 10, pp. 7561–7570, 2019.

[7] I. Zamudio-Ramirez, J. J. Saucedo-Dorantes, J. Antonino-Daviu, R. A. Osornio-Rios, and L. Dunai, "Detection of uniform gearbox wear in induction motors based on the analysis of stray flux signals through statistical time-domain features and dimensionality reduction techniques," *IEEE Transactions on Industry Applications*, vol. 58, no. 4, pp. 4648–4656, 2022.

[8] P. A. Panagiotou, I. Arvanitakis, N. Lophitis, J. A. Antonino-Daviu, and K. N. Gyftakis, "A new approach for broken rotor bar detection in induction motors using frequency extraction in stray flux signals," *IEEE Transactions on Industry Applications*, vol. 55, no. 4, pp. 3501–3511, 2019.

[9] K. N. Gyftakis, P. A. Panagiotou, and S. B. Lee, "Generation of mechanical frequency related harmonics in the stray flux spectra of induction motors suffering from rotor electrical faults," *IEEE Transactions on Industry Applications*, vol. 56, no. 5, pp. 4796–4803, 2020.

[10] A. Djerdir, J.-A. Farooq, A. Rezig, and A. Miraoui, "Faults in permanent magnet traction motors: state of the art and modelling approaches," in *IEEE PES General Meeting*, 2010, pp. 1–5.

[11] P. C. M. L. Filho, D. C. Santos, F. B. Batista, and L. M. R. Baccarini, "Axial stray flux sensor proposal for three-phase induction motor fault monitoring by means of orbital analysis," *IEEE Sensors Journal*, vol. 20, no. 20, pp. 12 317–12 325, 2020.

[12] P. C. M. Lamim Filho, L. M. Rabelo Baccarini, F. B. Batista, and A. C. Araújo, "Orbit analysis from a stray flux full spectrum for induction machine fault detection," *IEEE Sensors Journal*, vol. 21, no. 14, pp. 16 152–16 161, 2021.

[13] X. Liu, W. Miao, Q. Xu, L. Cao, C. Liu, and P. W. T. Pong, "Inter-turn short-circuit fault detection approach for permanent magnet synchronous machines through stray magnetic field sensing," *IEEE Sensors Journal*, vol. 19, no. 18, pp. 7884–7895, 2019.

[14] V. Gurusamy, E. Bostanci, C. Li, Y. Qi, and B. Akin, "A stray magnetic flux-based robust diagnosis method for detection and location of interturn short circuit fault in pmsm," *IEEE Transactions on Instrumentation and Measurement*, vol. 70, pp. 1–11, 2021.

[15] V. Gurusamy, K. H. Baruti, M. Zafarani, W. Lee, and B. Akin, "Effect of magnets asymmetry on stray magnetic flux based bearing damage detection in pmsm," *IEEE Access*, vol. 9, pp. 68 849–68 860, 2021.

[16] S. Reza Mortezaei, M. Hosseini Aliabadi, and S. Javadi, "Eccentricity fault detection in surface-mounted permanent magnet synchronous motors by analytical prediction, fem evaluation, and experimental magnetic sensing of the stray flux density," *Journal of Magnetism and Magnetic Materials*, vol. 589, p. 171441, 2024.

[17] C. Ma, J. Li, N. Zhang, F. Bu, and Z. Yang, "Open-circuit radial stray magnetic flux density based noninvasive diagnosis for mixed eccentricity parameters of interior permanent magnet synchronous motors in electric vehicles," *IEEE Transactions on Industrial Electronics*, vol. 70, no. 2, pp. 1983–1992, 2023.

[18] H.-K. Yeo, D.-K. Lim, D.-K. Woo, J. Ro, and H.-K. Jung, "Magnetic equivalent circuit model considering overhang structure of a surface-mounted permanent-magnet motor," *IEEE Transactions on Magnetics*, vol. 51, no. 3, pp. 1–4, 2015.

Summary

The objective of the doctoral research program was to investigate innovative fault diagnosis and control strategies for three-phase and multiphase machines. Specifically, fault diagnostic algorithms designed to satisfy safety-critical requirements have been developed using analytical modeling of the electrical machines along with artificial intelligence strategies.

The initial year of the PhD program focused on simulating failures in stator windings, encompassing high resistance connections, manufacturing defects, and inter-turn short circuits. An thorough analytical model has been proposed for a dual-three-phase brushless motor drive, providing real-time detection of the just mentioned faults without the need for measuring equipment. A finite element model of the machine has been designed to assess the validity of the analytical models. Consequently, the derived equations have been verified by finite element analysis and directly utilizing a prototype of a dual-three-phase motor in the LEMAD laboratory.

During the course of the second year, control algorithms for fault diagnosis using machine learning have been developed. In particular, two algorithms have been presented in order to identify failures while avoiding using complex equations that always require approximations due to uncertainty motor design parameters. In contrast, machine learning algorithms discover themselves hidden correlations between variables and can identify failures just using data obtained from the control system.

The third year focused on enhancing the models and control strategies developed in prior years and validating theoretical outcomes. Furthermore, in the third year, the collaboration with the research group at the Polytechnic University of Valencia, led by Professor Jose Alfonso Antonino-Daviu (IEEE Senior Member), was noteworthy. A technique for diagnosing rotor eccentricity by the measurement of stray flux around the stator yoke, utilizing a specific set of sensors, was developed during this partnership. The detected stray flux provides insights about

the machine's health and facilitates the identification of the sort of eccentricity present.

A Appendix

A.1 Magnetic Circuits

A magnetic circuit refers to the region of material which holds the magnetic field lines produced by electric currents flowing through a set of conductors or by PMs. The relationships among the variables that govern the physical behaviour of magnetic and electric fields are determined by the equations of electromagnetism (Tab. A1).

The material medium in which the fields described by electromagnetism's equations develop may be magnetic, dielectric, or conducting and the scalar quantities associated with each of these materials are determined based on the specific phenomenon they are involved in. Thus, any material has properties characterized by scalar variables including conductivity (σ), permittivity

TABLE A1: Equations of electromagnetism.

Differential form	Integral form	-
$\nabla \times \bar{E} = -\frac{\partial \bar{B}}{\partial t}$	$\oint_l \bar{E} \cdot d\bar{l} = -\oint_S \frac{\partial \bar{B}}{\partial t} \cdot \hat{n} d\bar{S} = -\frac{d\varphi}{dt}$	Faraday's law
$\nabla \times \bar{H} = \bar{J} + \frac{\partial \bar{D}}{\partial t}$	$\oint_l \bar{H} \cdot d\bar{l} = i + \oint_S \frac{\partial \bar{D}}{\partial t} \cdot \hat{n} d\bar{S}$	Ampere's law
$\nabla \cdot \bar{J} = -\frac{\partial \rho_c}{\partial t}$	$\oint_S \bar{J} \cdot \hat{n} d\bar{S} = \frac{dQ}{dT}$	Conservation of charge
$\nabla \cdot \bar{D} = \rho_c$	$\oint_S \bar{D} \cdot \hat{n} d\bar{S} = Q$	Gauss' law
$\nabla \cdot \bar{B} = 0$	$\oint_S \bar{B} \cdot \hat{n} d\bar{S} = 0$	Solenoidality of $\bar{B}$
$\nabla \cdot \bar{J} = 0$	$\oint_S \bar{J} \cdot \hat{n} d\bar{S} = 0$	Solenoidality of $\bar{J}$

TABLE A2: Constitutive equations.

Field	Equation
Current field	$\bar{E} = \rho_c \bar{J}$
Electric field	$\bar{D} = \varepsilon_p \bar{E}$
Magnetic field	$\bar{B} = \mu \bar{H}$

(ε_p) and magnetic permeability (μ). These variables introduce the material constitutive laws (Tab. A2).

When studying electromagnetic phenomena, it is common to assume that materials are continuous, homogeneous, isotropic, and linear. Under those circumstances, σ and ε_p are fixed values whereas μ varies in accordance with the magnetization of the material. The magnetic permeability can be written as:

$$\mu = \mu_0 \mu_r. \tag{A1}$$

where μ_0 is the vacuum permeability (constant value) and μ_r is the relative permeability, which is an intrinsic magnetic characteristic of the material.

The equations in Tab. A1 have general validity, but within the field of magnetic circuits, quasi-stationary magnetic fields are frequently investigated. These fields exhibit gradual fluctuations in electromagnetic quantities over time, which permits neglecting the displacement currents in comparison to conduction currents ($\frac{\partial \bar{D}}{\partial t} = 0$). This assumption persists in all the subsequent chapters.

In Tab. A1, two key elements are emphasized, namely the solenoidality of the vectors $\bar{B}$ and $\bar{I}$. This property indicate that the field lines of a solenoidal vector remain unaltered as they traverse a closed surface, irrespective of the surface they encounter. Hence, the subsequent assumptions hold valid for the vector $\bar{B}$ and any other vector that is solenoidal:

- All flux lines entering a surface must necessarily exit it.
- Each flux line either ends in a finite region or reaches infinity (there are no sources or black holes).
- The flux of $\bar{B}$ remains constant across all sections of a flux tube. In other words, the flux linked from various surfaces sharing the same contour is identical.

By considering the aforementioned three properties of the solenoidal vector $\bar{B}$, it is possible to represent the magnetic flux through the use of a flux tube in which the flux lines are consistently perpendicular to every surface of the tube (see Fig. A1a).

Let's consider a solenoid with an infinitely small cross section, denoted as dS, and an infinitely short length, denoted as dl. The solenoid is wound by N_t turns, and an infinitely small current, denoted as di, flows through them (see Fig. A1b). The solenoid generates a uniform flux, denoted as $d\varphi$, whose expression is:

$$d\varphi = \bar{B} \cdot d\bar{S}. \tag{A2}$$

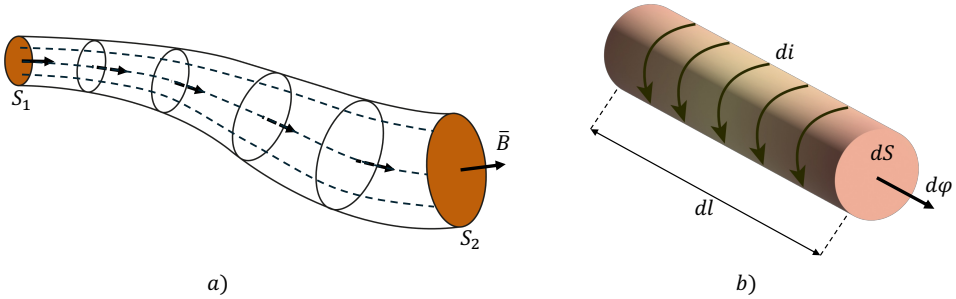

FIGURE A1: Magnetic flux generation. a) Magnetic flux originated by a solenoid. b) Flux tube through which magnetic flux lines flow.

The total magnetic flux linked with the N_t turns wounding the solenoid is determined by integrating the contributions of the infinitesimal components $d\varphi$ from all points on the closed surface as follows:

$$\varphi = N_t \oint_S d\varphi = N_t \oint_S \bar{B} \cdot \hat{n} d\bar{S}. \tag{A3}$$

The Amperes' law introduces the concept of magnetomotive force:

$$\mathscr{F} = \oint_l \bar{H} \cdot d\bar{l} = N_t i = \varphi \Re \tag{A4}$$

where $\Re$ is the total magnetic reluctance of the magnetic circuit defined as follows:

$$\Re = \frac{1}{\mu} \frac{l}{S}. \tag{A5}$$

Equation (A4) often referred to as Hopkinson's law and bears a striking resemblance to Ohm's first law $v = Ri$. Indeed, by equating $\mathscr{F}$ with the electric voltage v, flux φ with current i, and reluctance $\Re$ with resistance R, the electrical equivalent of Hopkinson's equation, also known as Ohm's first law, is obtained (see Fig. A2).

It is noteworthy that the quantity of turns comprising the circuit does not have any influence on the magnetic reluctance. Conversely, it comprises exclusively evidence pertaining to the geometric properties of the flux tube through which the turns are wound. Therefore, in order to account for the number of turns, inductance L is frequently favored over reluctance when establishing equations for magnetic circuits:

$$L = \frac{N_t^2}{\Re}. \tag{A6}$$

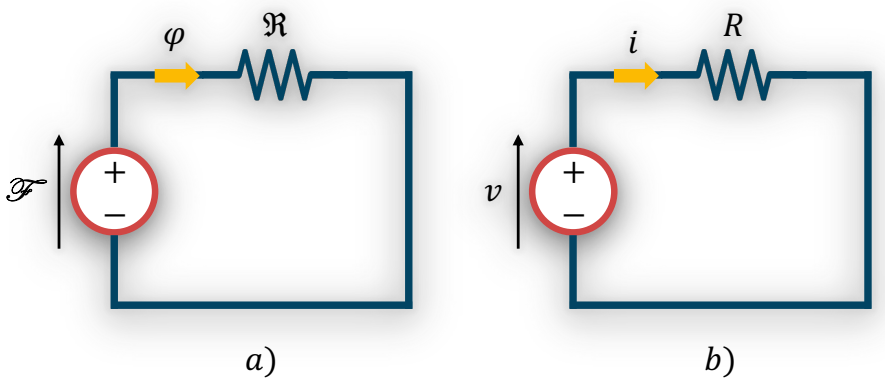

FIGURE A2: Equivalent circuits. a) Hopkinson's law. b)Ohm's first law.

A.2 Magnetic Materials Behavior

Magnetic materials, also referred to as ferromagnetic materials, find application in the design of magnetic circuits and the manufacture of PMs for electric motors. The primary characteristics of a material that is appropriate for the purpose of designing a magnetic circuit for an electric motor include:

- Elevated magnetic permeability.
- Minimal losses when operating in Alternating Current (AC).
- Excellent physical and mechanical characteristics include robust mechanical strength, ease of manufacturability by punching and laser cutting, and high thermal and chemical compatibility.
- Cost-effective.

Let us examine the closed circuit in Fig.A3a, where an electric current i is flowing. The latter generates a magnetic flux and a magnetic dipole $\bar{\kappa}$ orthogonal to the surface whose value is:

$$\bar{\kappa} = iS\hat{n}. \tag{A7}$$

Considering all the magnetic dipoles per unit of volume $d\tau$ (see Fig. A3b), the magnetization intensity vector $\bar{M}$ is obtained as follows:

$$\bar{M} = \frac{\sum_i^N \bar{\kappa}_i}{d\tau}. \tag{A8}$$

By applying an external magnetic field $\bar{H}$, the dipoles are oriented towards certain direction inducing a magnetization as illustrated in Fig. A4. As a result, $\bar{M}$ can be defined as the

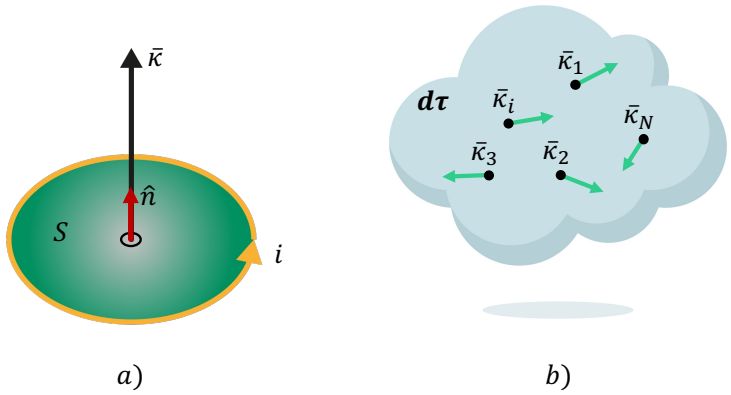

FIGURE A3: Magnetic dipole. a) Generation of a magnetic dipole resulting from the flow of an electric current. b) Magnetic dipoles distributed in a volume $d\tau$.

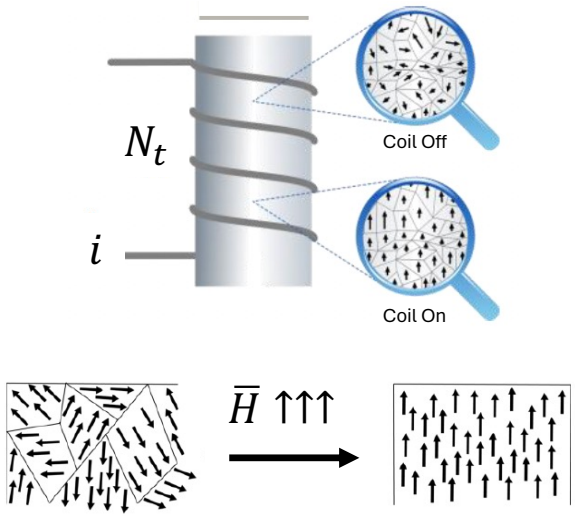

FIGURE A4: Orientation of the magnetic dipoles due to the application of an external magnetic field.

material's response to a certain magnetic field application and the relationship between $\bar{H}$ and $\bar{M}$ is expressed as follows:

$$\bar{H} = \mu_0 \chi_m \bar{M}. \tag{A9}$$

where χ_m is the magnetic susceptibility of the material.

The magnetic material may exhibit diamagnetic properties, denoted by a negative value of χ_m, or paramagnetic properties, denoted by a positive value of χ_m. Conversely, materials that exhibit a variable χ_m value in response to an applied magnetic field are known to as ferromagnetic. The latter refers to materials used in the manufacture of electric motors, which possess the characteristic of retaining their magnetization even after the removal of the applied magnetic field, as long as the temperature remains below the a certain temperature (Curie temperature). This characteristic of ferromagnetic materials is called magnetic hysteresis and it is described by the $B - H$ curve shown in Fig. A5a.

In order to analyze the magnetization response of a ferromagnetic material its behaviour when it is completely demagnetized, is considered. Initially, both the magnetic field H and the magnetic flux density B have null values. When a rising magnetic field H is applied, progressively the current i and consequently the applied magnetomotive force $\mathscr{F}$ increase. As H grows, there is an initial narrow range where the response of the material is linear, characterized by a high slope. Once the field magnitude beyond a specific threshold, the characteristic curve experiences an inflection point, resulting in a distinct material behavior. This change is characterized by a sharp bend, following which the curve returns to a linear pattern with a minimal slope. At this point, the material has been saturated, meaning that any additional rise in the applied field will not result in a significant increase in the value of induction. Once reached the saturation point, even if the magnetic field is removed, contrary to expectations, the induction value does not nullify and the material does not follow the same curve as the initial magnetization. Instead, it exhibits a delay known as hysteresis. At $H = 0$, the induction value is different from zero and equal to B_r, which is referred to as remanence induction or residual magnetization. To nullify the magnitude of B_r, a field with an opposite polarity must be applied. The value of B drops by reaching a value of $H = -H_c$, which is referred to as the coercive field. Continuing to lower the applied field until the value of $-H_s$ achieves a symmetrical negative saturation point consequently gradually decreasing H, the curve ultimately reaches the value of $-B_r$. By reversing the field once more and gradually increasing it until the magnetic field strength reaches positive H_c, the value of B becomes again zero.

Based on the value of H_c and B_r the ferromagnetic materials can be classified as:

- Soft margin materials: exhibit a narrow hysteresis loop with a low coercive force (see Fig. A5(b)) and show a high susceptibility to magnetization. Furthermore, they possess a high level of permeability. They are employed in electrical devices such as transformers, motors, and generators. The most frequently utilized materials include iron and its alloys containing nickel, cobalt, and silicon, as well as low carbon steels and soft ferrites.

- Hard margin materials: are characterized by a high coercive force and a high residual induction (see Fig. A5(c)). They are used to produce PMs since, once magnetized, are challenging to demagnetize. Some Alnico alloys belong to this class. These are iron-based alloys with additions of aluminum, nickel, cobalt, and copper.

A.3 Flux Production in Magnetic Circuits

Consider the magnetic anchor depicted in Fig. A6, which have a cross-sectional area denoted as S, an average length denoted as l_{fe}, and an air-gap with a length of δ_0.

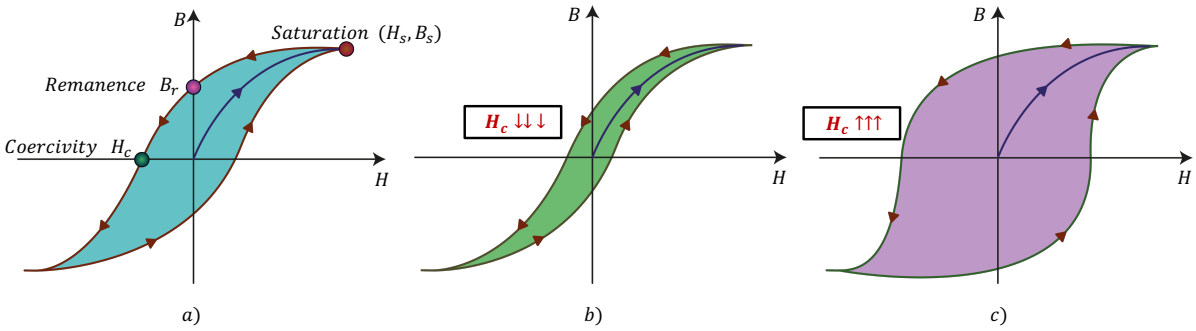

FIGURE A5: Hysteresis loops for ferromagnetic material. a) Hysteresis loop description. b) Soft margin material. c) Hard margin material

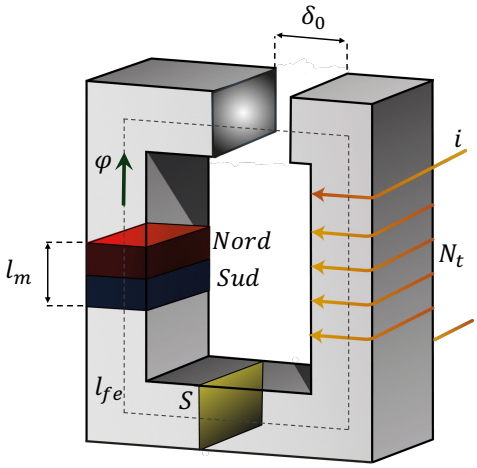

FIGURE A6: Magnetic circuit.

A magnet of thickness l_m is positioned on the right side of the anchor, while N_t turns conducting a current i are wound around the left side column. The circuit depicted in Fig. A6 demonstrates magnetic characteristics that have similarities to those of a PM motor, with magnets mounted on the rotor and windings located in the stator slots. Therefore, by examining the magnetic properties of thee aformetioned circuit, one may comprehend how air-gap flux is generated in PM electric motors.

Typically, the magnetization characteristic of a magnet is approximated as linear (see Fig. A7). Therefore, the magnet's remanance induction is as follows:

$$B_m = B_r + \mu H_m. \tag{A10}$$

Furthermore, where an electric current is provided to a coil, the load curve is given:

$$B_m = \frac{\mu_0 l_m}{\delta_0}\left[\frac{Ni}{l_m} - H_m\right]. \tag{A11}$$

Due to the solenoidal property, the magnetic field is constant in each section of the magnetic circuit and the flux φ flowing through the flux tube represented by the anchor may be estimated

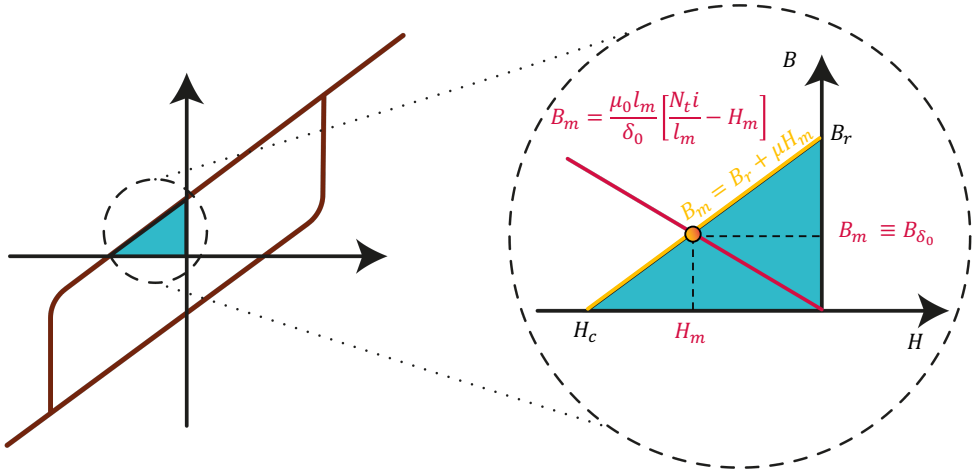

FIGURE A7: Linearized magnetization curve.

using the Ampere's law (A4), as follows:

$$B_m = B_{\delta_0} = B_{fe} = \frac{\varphi}{S}. \tag{A12}$$

In addition the Ampere's law allows to state:

$$H_m l_m + H_0 \delta_0 + H_{fe} l_{fe} = N_t i. \tag{A13}$$

Therefore, the constitutive equation $\bar{B} = \mu \bar{H}$ along with (A12) and (A13) gives:

$$\varphi = \frac{N_t i + \frac{B_r}{\mu} l_m}{\frac{l_m}{\mu S} + \frac{\delta_0}{\mu_0 S} + \frac{l_{fe}}{\mu_{fe} S}}. \tag{A14}$$

Expression (A14) can be rewritten in terms of reluctance and magnetomotive force as follows:

$$\varphi = \frac{\mathscr{F}_t + \mathscr{F}_m}{\Re_m + \Re_{\delta_0}}. \tag{A15}$$

where $\mathscr{F}_t$ is the magnetomotive force produced by the current flowing through the coil and $\mathscr{F}_m$ is the magnetomotive force produced by the magnets. It is worth noting that, in (A15), $\Re_{fe}$ has been neglected since $\mu_{fe} >> \mu_0$.

Equation (A15) defines Hopkinson's law for the circuit shown in Fig. A6. It states that the generated flux is influenced by the geometry of the magnet and airgap, as well as the magnetomotive force produced by the magnets and the coil supplied by the current.